DISS. ETH NO. 25579

An accessory-mineral perspective on magma storage in subvolcanic reservoirs: the Kneeling Nun Tuff, New Mexico

A thesis submitted to attain the degree of

DOCTOR OF SCIENCES OF ETH ZURICH

(Dr. sc. ETH Zurich)

presented by

DAWID SZYMANOWSKI

MSc in Earth Sciences, ETH Zurich

born on 15.02.1990

citizen of Poland

accepted on the recommendation of

Prof. Dr. Olivier Bachmann, examiner
Dr. Ben Ellis, co-examiner
Dr. Jörn-Frederik Wotzlaw, co-examiner
Prof. Dr. Adam Kent, co-examiner

2018

Abstract

Volcanoes are a source of threat to human life in many parts of the world, yet the understanding of the physical conditions and timescales of magma storage and remobilisation remains insufficient to confidently manage the existing risk. The ongoing debate about how magma is stored prior to eruptions has particular implications for the ability of geophysical surveys to identify accumulations of melt that are potentially eruptible.

The objective of this study was to develop new approaches constraining the timescales and conditions of magma storage prior to volcanic eruptions. The principal tools used to achieve this are petrological and geochemical characterisation of eruptive products and high-precision U–Pb geochronology of accessory mineral phases (zircon and titanite) by isotope dilution thermal ionisation mass spectrometry (ID-TIMS). The main focus was on a case study from the Kneeling Nun Tuff, a deposit of a large, caldera-forming eruption from the mid-Tertiary Mogollon–Datil volcanic field in New Mexico (USA). The eruption that produced the 35.3 Ma Kneeling Nun Tuff deposited more than 900 km^3 of crystal-rich material which has a rich mineral assemblage and an age which allowed us to fully exploit the modern analytical capabilities of U–Pb geochronology.

In the first part (Chapter 2) we developed a novel approach to constraining dominant magma storage conditions based on simultaneously determined crystallisation temperatures and ages of zircon and titanite. In the Kneeling Nun Tuff, ID-TIMS U–Pb geochronology of single crystals of the two minerals independently revealed a protracted crystallisation history in excess of 600,000 years. Since titanite stability in the Kneeling Nun Tuff magma is limited to temperatures lower than ca. 730 °C, the preservation of an extended range of titanite dates was interpreted to indicate long-term storage of most of the erupted magma volume at or below this temperature, but above the granitic solidus (ca. 680–700 °C). The low model temperatures and high observed crystallinity of the Kneeling Nun Tuff require that the magma was stored as high-crystallinity mush, which was subsequently rejuvenated by heat input to reach a mobile, eruptible state. Finally, the systematics of zircon and titanite trace elements were used to explore the thermal effect of such rejuvenation in other titanite-bearing eruptive units.

Chapter 3 builds on the findings from Chapter 2 by examining a suite of samples of the Kneeling Nun Tuff as well as juvenile and lithic clasts found within the ignimbrite. Whole-rock, feldspar and amphibole compositions were used to understand the first-order pre-eruptive magma storage conditions and magmatic architecture. A vastly expanded ID–TIMS U–Pb zircon geochronology dataset was combined with zircon trace-element geochemistry to arrive at a detailed, time-resolved record of chemical and physical changes within the magma reservoir. Chemical compositions and zircon ages revealed a prolonged (> 1.5 million years since early intrusions) growth and maturation of the magma reservoir that was heterogeneous in terms of temperature, melt composition and crystallinity. The protracted storage at dominant crystallinity in excess of 50 % cul-

minated in a period of ca. 100,000 years of increase in recharge heat supply and related homogenisation, decrease in crystallinity to 40–50 %, and potential increase in average melt temperature, leading up to eruption at 35.305 ± 0.021 Ma. Sampling of co-magmatic lithic clasts derived from early-cooled domains of the magma reservoir showed that the long, million year-scale maturation time was shared across all erupted domains of the magmatic system, irrespective of their final cooling history.

The last part of the thesis (Chapter 4) focusses on laboratory protocol developments required to accurately perform some of the analyses presented in the Kneeling Nun Tuff study as well as similar future approaches using the Ti-in-zircon thermometer. This geothermometer is based on the temperature-dependence of Ti incorporation into zircon and is widely applied to estimate zircon crystallisation temperatures across many geological environments. In this paper we identified a critical lack of suitable matrix-matched reference materials for *in situ* analyses of Ti contents of zircon crystals, which may bias the results by as much as 30 % for Ti concentration or up to tens of degrees for the model temperatures. To alleviate this issue, we selected two thoroughly characterised zircon reference materials, zircons 91500 and GZ7, and tested them for homogeneity with respect to Ti/Si by secondary ion mass spectrometry (SIMS) and laser ablation–inductively coupled plasma mass spectrometry (LA-ICP-MS). The results suggested homogeneity close to the precision of individual spot analyses, so the two samples were developed as primary reference materials for Ti. The Ti mass fraction was independently determined in multiple fragments of these two zircon crystals using isotope dilution (ID)-ICP-MS employing a precisely calibrated ^{47}Ti–^{49}Ti double spike. A set of complementary secondary reference materials was also characterised using LA-ICP-MS with Ti concentrations anchored to the new isotope dilution values, thereby creating a self-consistent framework permitting comparisons of Ti-in-zircon datasets whenever data for these secondary reference materials are reported.t

Riassunto

I vulcani rappresentano una minaccia per la vita umana in molte parti del mondo, eppure la comprensione delle condizioni fisiche e dei tempi di accumulo e rimobilizzazione dei magmi rimane insufficiente per la gestione del rischio esistente. L'attuale dibattito riguardante le modalità di accumulo e stoccaggio dei magmi nella crosta superiore prima di essere eruttati in superficie ha implicazioni dirette sull'abilità di identificare volumi discreti di magma potenzialmente eruttabile utilizzando indagini geofisiche.

L'obiettivo primario di questo studio è proprio quello di sviluppare nuovi metodi atti a determinare i tempi e le condizioni fisiche di stoccaggio dei magmi prima delle eruzioni vulcaniche. Gli strumenti principali di questa ricerca sono la caratterizzazione petrologica e geochimica di prodotti vulcanici e la geocronologia U–Pb di alta precisione su minerali accessori (zircone e titanite) tramite spettrometria di massa di ionizzazione termica con diluizione isotopica (ID-TIMS). Il tema centrale è l'analisi di una spessa ignimbrite, il Kneeling Nun Tuff, formatasi in seguito ad una voluminosa eruzione calderica avvenuta nel Terziario medio e riconducibile al campo vulcanico di Mogollon–Datil (Nuovo Messico, USA). L'eruzione del Kneeling Nun Tuff (35.3 Ma) ha emesso più di 900 km^3 di magma altamente cristallino, caratterizzato da una ricca varietà mineralogica ed un'età che ci ha permesso di sfruttare al massimo le moderne capacità analitiche della geocronologia U–Pb.

Nella prima parte di questo studio (Capitolo 2) abbiamo sviluppato un nuovo approccio atto a determinare le condizioni fisiche di stoccaggio dei magmi del Kneeling Nun Tuff, basato sulla determinazione simultanea di temperature ed età di cristallizzazione di zirconi e titaniti. Nel Kneeling Nun Tuff la geocronologia U–Pb tramite ID-TIMS di cristalli singoli di zircone e titanite indica un periodo di cristallizzazione che va oltre i 600'000 anni. Siccome la stabilità della titanite nel magma del Kneeling Nun Tuff è limitata a temperature inferiori a ca. 730 °C, la preservazione di titaniti con un ampio intervallo di età radiometriche dimostra che la maggior parte del volume del magma coinvolto è stata conservata per un lungo periodo di tempo a temperature comprese tra ca. 730 °C e la temperatura del *solidus* granitico (ca. 680–700 °C). Le basse temperature ottenute con il nostro modello e l'elevata cristallinità del Kneeling Nun Tuff indicano che il magma è stato stoccato nella crosta in condizioni di alta cristallinità (*crystal mush*) per poi venire rimobilizzato e reso eruttabile tramite un input termico riconducibile ad una o più ricariche magmatiche. Inoltre, la sistematica degli elementi in traccia negli zirconi e nelle titaniti è stata utilizzata per esplorare l'effetto termico della rimobilizzazione di *mush* cristallini in altre eruzioni che contengono zircone e titanite.

Il Capitolo 3 si sviluppa a partire dai risultati del Capitolo 2 ed esamina una serie di campioni (iuvenili e litici) del Kneeling Nun Tuff. Dati composizionali di roccia totale, feldspati ed anfiboli sono stati utilizzati per ottenere informazioni riguardanti le condizioni fisiche di stoccaggio dei magmi e ricostruire l'architettura del sistema magmatico profon-

do. Un ampio *database* di età radiometriche è stato ottenuto mediante l'analisi ID-TIMS dei rapporti isotopici di U e Pb negli zirconi del Kneeling Nun Tuff. Questi risultati, uniti alle concentrazioni degli elementi in traccia nei cristalli di zircone, hanno fornito una cronaca dettagliata delle fluttuazioni delle condizioni fisico-chimiche nel *reservoir* magmatico. Le composizioni chimiche e le età degli zirconi hanno dimostrato che lo sviluppo e la maturazione del corpo magmatico che ha alimentato l'eruzione del Kneeling Nun Tuff si sono protratti per più di 1.5 milioni di anni (a partire dalle intrusioni cha hanno determinato le prime fasi di costruzione del *reservoir* magmatico). Le condizioni di stoccaggio del magma si sono rivelate eterogenee in termini di temperatura, composizione e cristallinità. Il prolungato accumulo di magma nella crosta è avvenuto in condizioni di elevata cristallinità (oltre 50 % di cristalli) ed è culminato in un periodo di aumentata ricarica e apporto di calore durato ca. 100′000 anni. In seguito a questa fase il *reservoir* magmatico ha subito una significativa omogeneizzazione, la sua temperatura media è probabilmente aumentata e la cristallinità è stata ridotta a 40–50 %, il ché potrebbe aver preparato il sistema per l'eruzione avvenuta 35.305 ± 0.021 Ma fa. Le analisi dei clasti litici co-magmatici, provenienti da regioni periferiche del reservoir magmatico che si sono raffreddate a contatto con la crosta "fredda", mostrano che i tempi di maturazione sono comuni a tutto il corpo magmatico, indipendente dal percorso di raffreddamento finale seguito dei diversi volumi di magma.

L'ultima parte di questa tesi (Capitolo 4) si concentra sullo sviluppo di metodologie e protocolli di laboratorio atti ad ottimizzare l'accuratezza di alcune analisi simili a quelle eseguite nello studio del Kneeling Nun Tuff e di future indagini che utilizzeranno il geotermometro Ti-in-zircone. Questo geotermometro è basato sulla relazione fra la concentrazione di Ti nello zircone e la temperatura, ed è ampiamente applicato alla stima di temperature di cristallizzazione di questo minerale in molte problematiche geologiche. In questo studio abbiamo riscontrato una critica mancanza in letteratura di materiali di riferimento accoppiati alla matrice appropriati per l'analisi *in situ* della concentrazione di Ti nello zircone. Tale mancanza può tradursi in un errore sulle misure di concentrazioni di Ti fino al 30 % e di decine di gradi sulla stima delle temperature di cristallizzazione. Al fine di far fronte a questa problematica, abbiamo selezionato due materiali di riferimento ben caratterizzati, gli zirconi 91500 e GZ7, e valutato la loro omogeneità rispetto al rapporto Ti/Si tramite spettrometria di massa a ioni secondari (SIMS) e spettrometria di massa ad accoppiamento induttivo e ablazione laser (LA-ICP-MS). I risultati mostrano che gli zirconi 91500 e GZ7 sono sufficientemente omogenei (i.e., la variazione dei valori ottenuti mediante i test di omogeneità è simile alla variabilità associata alle singole analisi) perciò i due campioni possono essere utilizzati in futuro come materiali di riferimento primari per il Ti. Il contenuto di Ti è stato determinato indipendentemente in più frammenti di questi cristalli di zircone tramite diluizione isotopica (ID) e ICP-MS, utilizzando un doppio *spike* (^{47}Ti–^{49}Ti) calibrato con precisione. Inoltre le concentrazioni di Ti di una serie di materiali di riferimento secondari sono state caratterizzate tramite LA-ICP-MS utilizzando i nuovi valori ottenuti mediante diluizione

isotopica. Tale caratterizzazione offre la possibilità di comparare direttamente diversi *dataset* di Ti-in-zircone (che riportano anche i valori di questi materiali di riferimento secondari) tramite confronto diretto con i valori delle concentrazioni di Ti misurate e riportate nel nostro studio.

Table of contents

Chapter 1

Introduction

1.1. Background

Volcanic eruptions represent some of the most destructive geological events that can affect both society and the environment, with effects ranging from local devastation to long-term effects on the Earth's climate on global scale (Robock, 2000; Self, 2006). Despite such significance of volcanism, the understanding of local patterns of eruptive activity, the geometry and physical states of magma storage regions, or eruption triggers is currently far from sufficient with the exception of several well-studied locations. Geophysical detection of eruptible magma bodies and, in a longer perspective, forecasting of eruptions with a high degree of confidence, rely on a firm understanding of the underlying processes operating within subvolcanic magma bodies. Two issues emerge as critical to establishing a framework to interpret the eruptive potential of magmatic systems: the physical states of magma bodies and the timescales over which any such state develops and changes.

The physical properties of magmas are decisive for the way they move or stall in the crust, where the key parameter—viscosity—can vary over many orders of magnitude as a function of composition, crystallinity, pressure, temperature, or water content (Mader et al., 2013). These key parameters affect both the ability of the system to erupt and its eruptive style. Some information about the physical state, and geometry, of active volcanic systems can be gleaned from geophysical surveys utilising passive and active seismic data (e.g. Farrell et al., 2014; Huang et al., 2015 for Yellowstone, Kiser et al., 2016, 2018 for Mount St. Helens, Flinders et al., 2018 for Long Valley caldera, Ward et al., 2014; Delph et al., 2017 for the Altiplano–Puna Magma Body or Zollo et al., 2008 for Campi Flegrei), electrical resistivity/magnetotelluric methods (e.g. Hill et al., 2009; Cordell et al., 2018) or geodetic (GPS and differential radar interferometry, InSAR) and gravity data (e.g. Tizzani et al., 2009; Parks et al., 2012; Feigl et al., 2014; Miller et al., 2017). The modelling and interpretation of the results of these surveys require knowledge of the underlying mechanisms and the physical properties of the particular mate-

rials present in the subsurface, which often results in large propagated uncertainties. Nonetheless, these investigations tend to converge on a view of magmatic systems as complex, transcrustal structures with multiple storage levels of relatively low melt content ('crystal mush'; Fig. 1.1). In particular, upper-crustal magma bodies that directly feed young volcanoes are commonly found to contain only a few to a few tens % of melt (Farrell et al., 2014; Ward et al., 2014; Huang et al., 2015; Flinders et al., 2018).

Since there are almost no active magmatic systems available for direct observation in the subsurface, the study of fossil eruptions and plutonic bodies remains critical to understanding how modern volcanoes operate. Textural and compositional analyses of magmatic rocks reveal sources of magmas and the processes of their differentiation from the source to the emplacement level, but perhaps more importantly, magmatic petrology can provide constraints on the pre-eruptive physical states and properties of magmas. In particular, thermobarometry (e.g. Ghiorso and Sack, 1991; Holland and Blundy, 1994; Nimis and Ulmer, 1998; Blundy and Cashman, 2001; Putirka, 2008) and phase-equilibrium experiments (e.g. Johnson and Rutherford, 1989; Gardner et al., 1995; Scaillet and Evans, 1999; Scaillet et al., 2008; Cadoux et al., 2014) are the primary sources of information about how crystals and melts are stored prior to eruptions. These techniques have shaped the community's views of igneous processes over the last decades and continue to provide new insights about the setup of magmatic plumbing systems (Bachmann and Huber, 2016; Cashman et al., 2017).

The other critical component necessary to understand how magmas behave in the crust is the time dimension of igneous processes such as magma reservoir assembly, growth, cooling and reorganisation, all affecting the ultimate eruptive potential. The timescales of such processes vary over many orders of magnitude (hours to millions of years), and are investigated with two groups of methods: geochronology, relying on the radioactive decay of unstable isotopes of elements, and the modelling of intra-crystal diffusion of elements (Turner and Costa, 2007; Reid, 2008). The former provides absolute ages of events whereas the latter gives a measure of relative time, which can be used to get absolute age only in conjunction with another event of known age (e.g. eruption).

The original objective of geochronology as applied to magmatic systems was the determination of absolute ages of volcanic eruptions or pluton emplacement. This approach, utilising mostly the K–Ar and U–Pb systems, allowed a first-order understanding of regional eruption frequencies, which fed into quantitative models of magma generation rates and fluxes on regional scale. However, as analytical techniques improved over the years, the precision achieved for individual analyses of increasingly small sample sizes have revealed previously unrecognised complexities within individual magmatic systems (Schmitt, 2011). These efforts have focussed primarily on single-grain to sub-grain geochronology of minerals enriched in elements such as U and Th; most commonly zircon, but also other accessory minerals such as allanite, titanite, chevkinite, monazite. It is now commonly found that individual eruptive units, or individual hand samples,

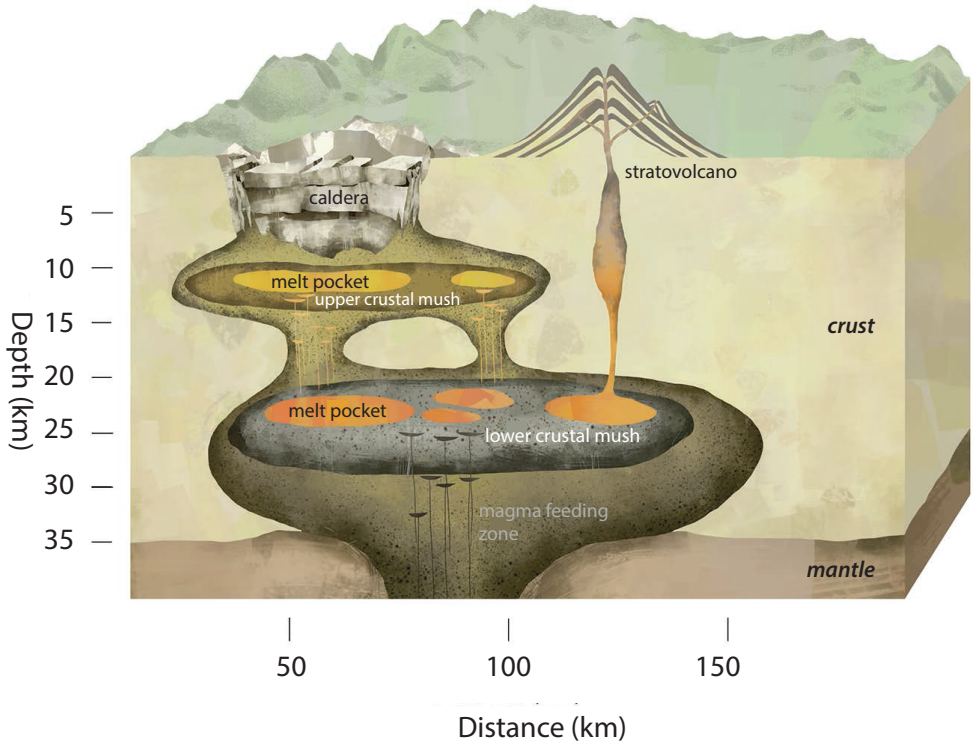

Figure 1.1. Schematic representation of the polybaric, transcrustal mush model (modified from Bachmann and Huber, 2016). Magmatic systems are composed of multiple, crystal-dominated magma bodies of variable melt content, connected through vertical melt transport.

may contain crystals of these minerals predating the eruption by up to a few 10^5 years (Reid et al., 1997; Brown and Fletcher, 1999; Vazquez and Reid, 2004; Charlier et al., 2005; Bachmann et al., 2007; Claiborne et al., 2010; Wotzlaw et al., 2013; Tierney et al., 2016; Kaiser et al., 2017). While the derivation of individual zircons from the same magma ('autocrysts', as opposed to scavenging from older magmatic wall-rocks – 'antecrysts') in specific cases may be debated, the by now critical body of data shows that individual magmatic systems are constructed over timescales of tens of thousands to millions of years. An approach complementary to accessory mineral dating focusses on major mineral phases (e.g. feldspars) in young rocks, containing small amounts of U, Th, or Ra, that can be analysed as bulk mineral separates (Condomines et al., 2003; Cooper, 2015). This method returns averaged mineral residence times that are typically shorter than those from accessory minerals, mostly within 10,000 years of eruption and rarely exceeding 100,000 years. These apparently conflicting timescales are challenging to interpret as they reflect complex recycling and averaging effects within magma reservoirs (Cooper, 2015).

An alternative approach to constraining magmatic timescales relies on the smoothing of compositional variations within individual crystals by diffusional migration of atoms during time spent at magmatic temperature. Upon eruption diffusion effectively stops, which locks the compositional profile and allows to calculate the elapsed diffusion time for given diffusivity, initial and boundary conditions and temperature of storage (Costa et al., 2008). This technique enables the relative dating of magmatic events that change melt composition or intensive parameters, which is recorded in crystals as an (initially) abrupt compositional boundary. Processes that can dated this way include e.g. recharge and magma mixing, assimilation, heating or cooling, decompression. Depending on the process and the mineral–element pair used, diffusion modelling can return timescales ranging from days–months (Morgan et al., 2004; Kilgour et al., 2014; Till et al., 2015; Hartley et al., 2016) to years (Zellmer et al., 2003; Wark et al., 2007; Druitt et al., 2012; Matthews et al., 2012; Flaherty et al., 2018) to 10^3–10^5 years (Morgan and Blake, 2006; Matthews et al., 2012; Chamberlain et al., 2014). However, the modelled compositional boundaries are in most studies limited to the prominent outer zones, which can be used to quantify the last major change experienced by the crystal, but cannot reveal the full length of the crystal's diffusion history (or the length of crystal residence).

One promising approach to magmatic timescales is the combination of radiometric (e.g. U–Pb, U–Th, Th–Ra) dating and diffusion modelling of the same crystals or populations of crystals to determine the relationship between absolute crystal ages and their subsequent magmatic storage history (Cooper and Kent, 2014). For major phases, this is again limited to bulk mineral separates (Cooper and Kent, 2014; Cooper, 2015), but for particular elements this approach might be applicable to accessory phases such as zircon (Rubin et al., 2017). The first results of these studies show that in upper-crustal magma reservoirs most of the total time since the crystallisation of a mineral (as given by radiometric age) may be spent at relatively low temperatures (as required by the limited intra-crystal diffusion), which effectively implies magma storage in high-crystallinity mush conditions. As a consequence, the capability of evolved magmatic systems to erupt might be limited to relatively brief periods following thermal rejuvenation from a near-solidus state (Cooper and Kent, 2014).

Recent improvements in the understanding of the storage of magma in the crust prior to eruptions appear to converge on a model featuring multi-level, crystal-dominated bodies of low melt fraction (Fig. 1.1). Of particular importance to the volcano science are shallow magma bodies that feed eruptions directly, but the details of their magma storage temperature, crystallinity and the corresponding physical properties, especially their development over time, remain a topic of a vigorous debate. This thesis aims to contribute to the understanding of such upper-crustal magma reservoirs by taking advantage of recent analytical developments and the increased ease of generating large geochemical datasets from individual eruptions, with a particular focus on accessory phase geochemistry.

1.2. Objectives of the thesis

The main goal of the research presented in this thesis is to contribute new data and new perspectives to the debate about the modes and timescales of magma storage prior to volcanic eruptions. This is accomplished by studying a particular deposit of a large explosive eruption from the Mogollon–Datil volcanic field in New Mexico (USA), the Kneeling Nun Tuff. The choice of the eruptive unit, particularly its large volume (> 900 km^3), age of 35.3 Ma and good exposure in the field, allows for a workflow combining:

1) classical tools of petrology (e.g. thermobarometry, textural and compositional analyses) to investigate the melt compositions, as well as crystallinity, depth, and temperature of mineral crystallisation and subsequent magmatic storage;

2) geochemistry and U–Pb geochronology of accessory mineral phases (zircon + titanite) to inform about the timescales of magma reservoir growth, maturation, and pre-eruptive rejuvenation.

In particular, the application of isotope dilution thermal ionisation mass spectrometry (ID-TIMS) U–Pb geochronology of both mineral phases to a unit of Cenozoic age was predicted to allow for enough precision in individual age determinations to generate a precise, radiometric timeline of the magma reservoir evolution. That way, deciphering the compositional information contained within the accessory minerals (whose crystallisation is placed in absolute time) is expected to provide an absolute chronology of chemical and physical changes in the subvolcanic magma reservoir. Such a record should be of great interest to the community given that most petrological constraints on fossil magma chambers lack an absolute time framework.

1.3. Geological setting

This study focusses on the Kneeling Nun Tuff (KNT), a deposit of one of the largest eruptions of the Tertiary Mogollon–Datil volcanic field (MDVF) in western New Mexico (USA), and one of the most voluminous explosive eruptions in the geological record according to the compilation of Mason et al. (2004). The MDVF belongs to a discontinuous belt of mid-Tertiary volcanism extending from the Southern Rocky Mountain volcanic field in Colorado in the north (Lipman et al., 1970; Lipman, 2007) to the Sierra Madre Occidental (Mexico) in the south (McDowell and Clabaugh, 1979; McDowell and McIntosh, 2012). The regional volcanism in the mid-Tertiary is characterised by an arc-like geochemical signature (high-K calc-alkaline series) and can in parts be related to the subduction of the Farallon plate beneath North America, however the large distance from the plate margin in present Colorado and New Mexico (several hundreds of kilometres) would require this subduction to be of low angle (Lipman et al., 1972; Coney and Reynolds, 1977). Alternatively, interpretations involving magma generation from lithospheric mantle previously modified by subduction have been proposed (Davis et al., 1993; Davis and Hawkesworth, 1993; Farmer et al., 2007). In the MDVF, active between

40 and 24 Ma, initial andesitic volcanism was followed by numerous caldera-forming eruptions of evolved-composition magmas, creating a region of multiple, often overlapping calderas (Elston, 1984). The initial mapping (Kuellmer, 1954; Elston, 1957; Giles, 1965, 1968; Elston et al., 1970, 1975) was aided by $^{40}Ar/^{39}Ar$ dating and paleomagnetic analyses to create a basic stratigraphic framework (McIntosh et al., 1990, 1991, 1992; McIntosh, 1991).

The Kneeling Nun Tuff (Elston, 1957) was erupted from the Emory caldera (Elston et al., 1975) in the southern part of the Black Range in the centre of MDVF at 35.36 ± 0.05 Ma (recalculated sanidine $^{40}Ar/^{39}Ar$ age; McIntosh et al., 1990) and is considered the largest eruption of the first pulse of MDVF silicic volcanism (McIntosh et al., 1992). The Emory caldera is well exposed and elongate parallel to the N–S trend of the Black Range, with a central resurgent uplift of 55 × 25 km size roughly matching the original caldera area. Peripheral fractures, many of which were subsequently reactivated during regional Basin and Range extension, extend outward for another 25 km from the caldera margins and are often associated with rhyolite domes and flows (Elston et al., 1975). The Kneeling Nun Tuff itself occurs both as thick caldera facies and outflow facies extending at least 30 km beyond the caldera margin, which led to a minimum eruptive volume estimate of 900 km^3 (Elston et al., 1975). The intracaldera facies consists of massive, welded and intensely jointed ignimbrite of thicknesses exceeding 500–1000 m (Kuellmer, 1954; Ericksen et al., 1970; Elston et al., 1975). The outflow facies of KNT is exposed in multiple fault blocks surrounding the Emory caldera, where its thickness reaches up to 150 m.

The Kneeling Nun Tuff is a crystal-rich (25–60 % crystals; Giles, 1965) rhyolite to dacite carrying a mineral assemblage of sanidine + plagioclase + quartz + biotite + hornblende + rare clinopyroxene + magnetite + ilmenite + titanite + apatite + zircon. The outflow ignimbrite is locally zoned, with an upward increase in crystallinity, phenocryst size and the proportion of plagioclase and ferromagnesian phases accompanied by a decrease in the amount of quartz and alkali feldspars (Giles, 1968). Both outflow and intracaldera KNT facies contain abundant crystal-rich pumice, rare crystal-poor pumice and lithic fragments of underlying andesites, Paleozoic basement rocks, and granites, porphyries and aplites of variable texture which are potentially contemporaneous and genetically related to KNT magma (Elston, 1989). In some areas within the caldera the xenoliths become larger (up to 10s of metres) and form zones of 'megabreccia' that were previously interpreted as vent or collapse breccias (Kuellmer, 1954; Elston, 1989).

The KNT typically overlies a thick sequence of broadly andesitic lavas and tuffs of the Rubio Peak formation (Elston, 1957; Davis and Hawkesworth, 1994), but locally a sequence of rhyolitic ignimbrites and air fall tuffs called the Sugarlump tuffs (Elston, 1957) occurs right beneath the KNT. Dated at 35.64 ± 0.12 Ma (recalculated from McIntosh et al., 1990), some of the Sugarlump tuffs may represent precursor eruptions of the same system that fed the KNT. Post-KNT, associated with the caldera resurgence following the eruption, an internally variable group of crystal-poor, pumiceous pyroclastic

deposits and rhyolitic lava domes and flows designated as the Mimbres Peak formation (34.2–34.3 Ma; O′Neill, 2002) occur at the caldera ring fractures (Elston, 1957; Elston et al., 1975). Additionally, at Rabb Park, a locality within the Emory caldera, a shallow subvolcanic complex dominated by rhyolite porphyry is described as intruding the KNT and plugging a KNT feeder vent (O′Brient, 1986).

1.4. Structure of the thesis

Following this introduction (**Chapter 1**), this doctoral thesis is subdivided into four chapters. The first two of them focus on the Kneeling Nun magmatic system; an additional chapter presents analytical developments applicable to studies utilising the widely-used Ti-in-zircon geothermometer:

Chapter 2, equivalent to a paper published in *Nature Geoscience*, presents a combination of zircon and titanite U–Pb geochronology and trace element compositions as a way of constraining dominant magmatic storage conditions within the Kneeling Nun magmatic system.

Chapter 3, a manuscript submitted to *Earth and Planetary Science Letters*, describes a detailed record of magmatic storage and rejuvenation leading to the Kneeling Nun Tuff eruption, including petrological data and zircon time–compositional systematics from a suite of texturally controlled samples.

Chapter 4, a paper published in *Chemical Geology*, documents the development of matrix-matched reference materials for accurate *in situ* analyses of Ti in zircon.

Chapter 5 contains final discussion and conclusions.

Appendices A–C include material supplementary to the main text of Chapters 2–4, excluding a number of large geochemical data tables provided in electronic form.

References

Bachmann, O., Huber, C., 2016. Silicic magma reservoirs in the Earth's crust. Am. Mineral. 101, 2377–2404.

Bachmann, O., Oberli, F., Dungan, M., Meier, M., Mundil, R., Fischer, H., 2007. $^{40}Ar/^{39}Ar$ and U–Pb dating of the Fish Canyon magmatic system, San Juan Volcanic field, Colorado: Evidence for an extended crystallization history. Chem. Geol. 236, 134–166.

Blundy, J., Cashman, K., 2001. Ascent-driven crystallisation of dacite magmas at Mount St Helens, 1980–1986. Contrib. Mineral. Petrol. 140, 631–650.

Brown, S.J.A., Fletcher, I.R., 1999. SHRIMP U–Pb dating of the preeruption growth history of zircons from the 340 ka Whakamaru Ignimbrite, New Zealand: Evidence for >250 k.y. magma residence times. Geology 27, 1035–1038.

Cadoux, A., Scaillet, B., Druitt, T.H., Deloule, E., 2014. Magma storage conditions of large Plinian eruptions of Santorini Volcano (Greece). J. Petrol. 55, 1129–1171.

Cashman, K.V., Sparks, R.S.J., Blundy, J.D., 2017. Vertically extensive and unstable magmatic systems: A unified view of igneous processes. Science 355, eaag3055.

Chamberlain, K.J., Morgan, D.J., Wilson, C.J., 2014. Timescales of mixing and mobilisation in the Bishop Tuff magma body: perspectives from diffusion chronometry. Contrib. Mineral. Petrol. 168, 1034.

Charlier, B., Wilson, C., Lowenstern, J., Blake, S., Van Calsteren, P., Davidson, J., 2005. Magma generation at a large, hyperactive silicic volcano (Taupo, New Zealand) revealed by U–Th and U–Pb systematics in zircons. J. Petrol. 46, 3–32.

Claiborne, L.L., Miller, C.F., Flanagan, D.M., Clynne, M.A., Wooden, J.L., 2010. Zircon reveals protracted magma storage and recycling beneath Mount St. Helens. Geology 38, 1011–1014.

Condomines, M., Gauthier, P.J., Sigmarsson, O., 2003. Timescales of magma chamber processes and dating of young volcanic rocks. Rev. Mineral. Geochem. 52, 125–174.

Coney, P.J., Reynolds, S.J., 1977. Cordilleran Benioff Zones. Nature 270, 403–406.

Cooper, K.M., 2015. Timescales of crustal magma reservoir processes: insights from U-series crystal ages. Geol. Soc. Spec. Publ. 422, 141–174.

Cooper, K.M., Kent, A.J.R., 2014. Rapid remobilization of magmatic crystals kept in cold storage. Nature 506, 480–483.

Cordell, D., Unsworth, M.J., Díaz, D., 2018. Imaging the Laguna del Maule Volcanic Field, central Chile using magnetotellurics: Evidence for crustal melt regions laterally-offset from surface vents and lava flows. Earth Planet. Sci. Lett. 488, 168–180.

Costa, F., Dohmen, R., Chakraborty, S., 2008. Time scales of magmatic processes from modeling the zoning patterns of crystals. Rev. Mineral. Geochem. 69, 545–594.

Davis, J., Hawkesworth, C.J., 1994. Early calc-alkaline magmatism in the Mogollon–Datil Volcanic Field, New Mexico, USA. J. Geol. Soc. London 151, 825–843.

Davis, J.M., Elston, W.E., Hawkesworth, C.J., 1993. Basic and intermediate volcanism of the Mogollon–Datil volcanic field: implications for mid-Tertiary tectonic transitions in southwestern New Mexico, USA. Geol. Soc. Spec. Publ. 76, 469–488.

Davis, J.M., Hawkesworth, C.J., 1993. The petrogenesis of 30–20 Ma basic and intermediate volcanics from the Mogollon–Datil Volcanic Field, New Mexico, USA. Contrib. Mineral. Petrol. 115, 165–183.

Delph, J.R., Ward, K.M., Zandt, G., Ducea, M.N., Beck, S.L., 2017. Imaging a magma plumbing system from MASH zone to magma reservoir. Earth Planet. Sci. Lett. 457, 313–324.

Druitt, T.H., Costa, F., Deloule, E., Dungan, M., Scaillet, B., 2012. Decadal to monthly timescales of magma transfer and reservoir growth at a caldera volcano. Nature 482, 77–80.

Elston, W.E., 1957. Geology and mineral resources of Dwyer quadrangle, Grant, Luna, and Sierra Counties, New Mexico. N.M. Bur. Mines Miner. Res. Bull. 38.

Elston, W.E., 1984. Mid-Tertiary ash flow tuff cauldrons, southwestern New Mexico. J. Geophys. Res. 89, 8733–8750.

Elston, W.E., 1989. Day 5: Field guide to the Emory caldera along NM-152 and in Tierra Blanca Canyon, in: Chapin, C.E., Zidek, J. (Eds.), Field excursions to volcanic terranes in the western United States, Volume I: Southern Rocky Mountain region, pp. 91–106.

Elston, W.E., Coney, P.J., Rhodes, R.C., 1970. Progress report on the Mogollon Plateau volcanic province, southwestern New Mexico, no. 2, in: Woodward, L.A. (Ed.), N.M. Geol. Soc. 21st Fall Field Conf. Guidebook, pp. 75–86.

Elston, W.E., Seager, W.R., Clemons, R.E., 1975. Emory Cauldron, Black Range, New Mexico, source of the Kneeling Nun Tuff, in: Seager, W.R., Clemons, R.E., Callender, J.F. (Eds.), N.M. Geol. Soc. 26th Fall Field Conf. Guidebook, pp. 283–292.

Ericksen, G.E., Wedow Jr., H., Eaton, G.P., Leland, G.R., 1970. Mineral resources of the Black Range Primitive Area, Grant, Sierra, and Catron Counties, New Mexico. U.S. Geol. Surv. Bull. 1319–E.

Farmer, G.L., Bailley, T., Elkins-Tanton, L.T., 2007. Mantle source volumes and the origin of the mid-Tertiary ignimbrite flare-up in the southern Rocky Mountains, western US. Lithos 102, 279–294.

Farrell, J., Smith, R.B., Husen, S., Diehl, T., 2014. Tomography from 26 years of seismicity revealing that the spatial extent of the Yellowstone crustal magma reservoir extends well beyond the Yellowstone caldera. Geophys. Res. Lett. 41, 3068–3073.

Feigl, K.L., Le Mével, H., Tabrez Ali, S., Córdova, L., Andersen, N.L., DeMets, C., Singer, B.S., 2014. Rapid uplift in Laguna del Maule volcanic field of the Andean Southern Volcanic zone (Chile) 2007–2012. Geophys. J. Int. 196, 885–901.

Flaherty, T., Druitt, T.H., Tuffen, H., Higgins, M.D., Costa, F., Cadoux, A., 2018. Multiple timescale constraints for high-flux magma chamber assembly prior to the Late Bronze Age eruption of Santorini (Greece). Contrib. Mineral. Petrol. 173, 75.

Flinders, A.F., Shelly, D.R., Dawson, P.B., Hill, D.P., Tripoli, B., Shen, Y., 2018. Seismic evidence for significant melt beneath the Long Valley Caldera, California, USA. Geology 46, 799–802.

Gardner, J., Rutherford, M., Carey, S., Sigurdsson, H., 1995. Experimental constraints on pre-eruptive water contents and changing magma storage prior to explosive eruptions of Mount St Helens volcano. Bull. Volcanol. 57, 1–17.

Ghiorso, M.S., Sack, R.O., 1991. Fe–Ti oxide geothermometry: thermodynamic formulation and the estimation of intensive variables in silicic magmas. Contrib. Mineral. Petrol. 108, 485–510.

Giles, D., 1965. Some aspects of the Kneeling Nun rhyolite tuff, in: Fitzsimmons, J.P., Balk, C.L. (Eds.), N.M. Geol. Soc. 16th Fall Field Conf. Guidebook, pp. 164–166.

Giles, D.L., 1968. Ash-flow tuffs of the Cobre Mountains, in: Titley, S.R. (Ed.), Arizona Geological Society Southern Arizona Guidebook III, pp. 289–291.

Hartley, M.E., Morgan, D.J., Maclennan, J., Edmonds, M., Thordarson, T., 2016. Tracking timescales of short-term precursors to large basaltic fissure eruptions through Fe–Mg diffusion in olivine. Earth Planet. Sci. Lett. 439, 58–70.

Hill, G.J., Caldwell, T.G., Heise, W., Chertkoff, D.G., Bibby, H.M., Burgess, M.K., Cull, J.P., Cas, R.A.F., 2009. Distribution of melt beneath Mount St Helens and Mount Adams inferred from magnetotelluric data. Nat. Geosci. 2, 785.

Holland, T., Blundy, J., 1994. Non-ideal interactions in calcic amphiboles and their bearing on amphibole–plagioclase thermometry. Contrib. Mineral. Petrol. 116, 433–447.

Huang, H.H., Lin, F.C., Schmandt, B., Farrell, J., Smith, R.B., Tsai, V.C., 2015. The Yellowstone magmatic system from the mantle plume to the upper crust. Science 348, 773–776.

Johnson, M.C., Rutherford, M.J., 1989. Experimentally determined conditions in the Fish Canyon Tuff, Colorado, magma chamber. J. Petrol. 30, 711–737.

Kaiser, J.F., de Silva, S., Schmitt, A.K., Economos, R., Sunagua, M., 2017. Million-year melt–presence in monotonous intermediate magma for a volcanic–plutonic assemblage in the Central Andes: Contrasting histories of crystal-rich and crystal-poor super-sized silicic magmas. Earth Planet. Sci. Lett. 457, 73–86.

Kilgour, G., Saunders, K., Blundy, J., Cashman, K., Scott, B., Miller, C., 2014. Timescales of magmatic processes at Ruapehu volcano from diffusion chronometry and their comparison to monitoring data. J. Volcanol. Geoth. Res. 288, 62–75.

Kiser, E., Levander, A., Zelt, C., Schmandt, B., Hansen, S., 2018. Focusing of melt near the top of the Mount St. Helens (USA) magma reservoir and its relationship to major volcanic eruptions. Geology 46, 775–778.

Kiser, E., Palomeras, I., Levander, A., Zelt, C., Harder, S., Schmandt, B., Hansen, S., Creager, K., Ulberg, C., 2016. Magma reservoirs from the upper crust to the Moho inferred from high-resolution Vp and Vs models beneath Mount St. Helens, Washington State, USA. Geology 44, 411–414.

Kuellmer, F.J., 1954. Geologic section of the Black Range at Kingston, New Mexico. N.M. Bur. Mines Miner. Res. Bull. 33.

Lipman, P.W., 2007. Incremental assembly and prolonged consolidation of Cordilleran magma chambers: Evidence from the Southern Rocky Mountain volcanic field. Geosphere 3, 42.

Lipman, P.W., Prostka, H.J., Christiansen, R.L., 1972. Cenozoic volcanism and plate-tectonic evolution of the western United States. I. Early and middle Cenozoic. Philos. T. Roy. Soc. A 271, 217–248.

Lipman, P.W., Steven, T.A., Mehnert, H.H., 1970. Volcanic history of the San Juan Mountains, Colorado, as indicated by potassium–argon dating. Geol. Soc. Am. Bull. 81, 2329–2352.

Mader, H.M., Llewellin, E.W., Mueller, S.P., 2013. The rheology of two-phase magmas: A review and analysis. J. Volcanol. Geoth. Res. 257, 135–158.

Mason, B.G., Pyle, D.M., Oppenheimer, C., 2004. The size and frequency of the largest explosive eruptions on Earth. Bull. Volcanol. 66, 735–748.

Matthews, N., Huber, C., Pyle, D., Smith, V., 2012. Timescales of magma recharge and reactivation of large silicic systems from Ti diffusion in quartz. J. Petrol. 53, 1385–1416.

McDowell, F.W., Clabaugh, S.E., 1979. Ignimbrites of the Sierra Madre Occidental and their relation to the tectonic history of western Mexico. Geol. Soc. Am. Spec. Papers 180, 113–124.

McDowell, F.W., McIntosh, W.C., 2012. Timing of intense magmatic episodes in the northern and central Sierra Madre Occidental, western Mexico. Geosphere 8, 1505.

McIntosh, W.C., 1991. Evaluation of paleomagnetism as a correlation criterion for Mogollon–Datil ignimbrites, southwestern New Mexico. J. Geophys. Res. 96, 13459–13483.

McIntosh, W.C., Chapin, C.E., Ratté, J.C., Sutter, J.F., 1992. Time-stratigraphic framework for the Eocene–Oligocene Mogollon–Datil volcanic field, southwest New Mexico. Geol. Soc. Am. Bull. 104, 851–871.

McIntosh, W.C., Kedzie, L.L., Sutter, J.F., 1991. Paleomagnetism and $^{40}Ar/^{39}Ar$ ages of ignimbrites, Mogollon–Datil volcanic field, southwestern New Mexico. N.M. Bur. Mines Miner. Res. Bull. 135.

McIntosh, W.C., Sutter, J.F., Chapin, C.E., Kedzie, L.L., 1990. High-precision $^{40}Ar/^{39}Ar$ sanidine geochronology of ignimbrites in the Mogollon–Datil volcanic field, southwestern New Mexico. Bull. Volcanol. 52, 584–601.

Miller, C.A., Williams-Jones, G., Fournier, D., Witter, J., 2017. 3D gravity inversion and thermodynamic modelling reveal properties of shallow silicic magma reservoir beneath Laguna del Maule, Chile. Earth Planet. Sci. Lett. 459, 14–27.

Morgan, D., Blake, S., Rogers, N., DeVivo, B., Rolandi, G., Macdonald, R., Hawkesworth, C., 2004. Time scales of crystal residence and magma chamber volume from modelling of diffusion profiles in phenocrysts: Vesuvius 1944. Earth Planet. Sci. Lett. 222, 933–946.

Morgan, D.J., Blake, S., 2006. Magmatic residence times of zoned phenocrysts: introduction and application of the binary element diffusion modelling (BEDM) technique. Contrib. Mineral. Petrol. 151, 58–70.

Nimis, P., Ulmer, P., 1998. Clinopyroxene geobarometry of magmatic rocks Part 1: An expanded structural geobarometer for anhydrous and hydrous, basic and ultrabasic systems. Contrib. Mineral. Petrol. 133, 122–135.

O'Brient, J.D., 1986. Preservation of primary magmatic features in subvolcanic pegmatites, aplites, and granite from Rabb Park, New Mexico. Am. Mineral. 71, 608–624.

O'Neill, J.M., 2002. Geologic investigations in the Lake Valley area, Sierra County, New Mexico. U.S. Geol. Surv. Prof. Paper 1644.

Parks, M.M., Biggs, J., England, P., Mather, T.A., Nomikou, P., Palamartchouk, K., Papanikolaou, X., Paradissis, D., Parsons, B., Pyle, D.M., 2012. Evolution of Santorini Volcano dominated by episodic and rapid fluxes of melt from depth. Nat. Geosci. 5, 749.

Putirka, K.D., 2008. Thermometers and barometers for volcanic systems. Rev. Mineral. Geochem. 69, 61–120.

Reid, M.R., 2008. How long does it take to supersize an eruption? Elements 4, 23–28.

Reid, M.R., Coath, C.D., Harrison, T.M., McKeegan, K.D., 1997. Prolonged residence times

for the youngest rhyolites associated with Long Valley Caldera: ^{230}Th–^{238}U ion microprobe dating of young zircons. Earth Planet. Sci. Lett. 150, 27–39.

Robock, A., 2000. Volcanic eruptions and climate. Rev. Geophys. 38, 191–219.

Rubin, A.E., Cooper, K.M., Till, C.B., Kent, A.J.R., Costa, F., Bose, M., Gravley, D., Deering, C., Cole, J., 2017. Rapid cooling and cold storage in a silicic magma reservoir recorded in individual crystals. Science 356, 1154–1156.

Scaillet, B., Evans, B.W., 1999. The 15 June 1991 eruption of Mount Pinatubo. I. Phase equilibria and pre-eruption P–T–fO_2–fH_2O conditions of the dacite magma. J. Petrol. 40, 381–411.

Scaillet, B., Pichavant, M., Cioni, R., 2008. Upward migration of Vesuvius magma chamber over the past 20,000 years. Nature 455, 216.

Schmitt, A.K., 2011. Uranium series accessory crystal dating of magmatic processes. Annu. Rev. Earth Planet. Sci. 39, 321–349.

Self, S., 2006. The effects and consequences of very large explosive volcanic eruptions. Philos. T. Roy. Soc. A 364, 2073–2097.

Tierney, C.R., Schmitt, A.K., Lovera, O.M., de Silva, S.L., 2016. Voluminous plutonism during volcanic quiescence revealed by thermochemical modeling of zircon. Geology 44, 683–686.

Till, C.B., Vazquez, J.A., Boyce, J.W., 2015. Months between rejuvenation and volcanic eruption at Yellowstone caldera, Wyoming. Geology 43, 695–698.

Tizzani, P., Battaglia, M., Zeni, G., Atzori, S., Berardino, P., Lanari, R., 2009. Uplift and magma intrusion at Long Valley caldera from InSAR and gravity measurements. Geology 37, 63–66.

Turner, S., Costa, F., 2007. Measuring timescales of magmatic evolution. Elements 3, 267–272.

Vazquez, J.A., Reid, M.R., 2004. Probing the accumulation history of the voluminous Toba magma. Science 305, 991–994.

Ward, K.M., Zandt, G., Beck, S.L., Christensen, D.H., McFarlin, H., 2014. Seismic imaging of the magmatic underpinnings beneath the Altiplano–Puna volcanic complex from the joint inversion of surface wave dispersion and receiver functions. Earth Planet. Sci. Lett. 404, 43–53.

Wark, D.A., Hildreth, W., Spear, F.S., Cherniak, D.J., Watson, E.B., 2007. Pre-eruption recharge of the Bishop magma system. Geology 35, 235–238.

Wotzlaw, J.F., Schaltegger, U., Frick, D.A., Dungan, M.A., Gerdes, A., Günther, D., 2013. Tracking the evolution of large-volume silicic magma reservoirs from assembly to supereruption. Geology 41, 867–870.

Zellmer, G., Sparks, R., Hawkesworth, C., Wiedenbeck, M., 2003. Magma emplacement and remobilization timescales beneath Montserrat: insights from Sr and Ba zonation in plagioclase phenocrysts. J. Petrol. 44, 1413–1431.

Zollo, A., Maercklin, N., Vassallo, M., Dello Iacono, D., Virieux, J., Gasparini, P., 2008. Seismic reflections reveal a massive melt layer feeding Campi Flegrei caldera. Geophys. Res. Lett. 35, L12306.

Chapter 2

Protracted near-solidus storage and pre-eruptive rejuvenation of large magma reservoirs*

D. Szymanowski, J. F. Wotzlaw, B. S. Ellis, O. Bachmann, M. Guillong, A. von Quadt

ABSTRACT

Building super-eruptive magma reservoirs in the cold, upper parts of Earth's crust requires a significant influx of magma over an extended period, sufficient to allow the magma to accumulate, differentiate and periodically erupt. Some models favour magma storage in a cold non-eruptible state, requiring extensive reactivation of the reservoirs before eruption, whereas others suggest storage at higher temperature and lower crystallinity, implying that magma in such reservoirs is readily eruptible. Consequently, constraining volcanic hazards requires observations directly linking magma residence timescales to the thermal state and crystallinity of storage. Here we simultaneously determine crystallisation temperatures and ages of magmatic crystals of zircon and titanite in the ~900 km^3 Kneeling Nun Tuff (New Mexico, USA), which allows us to place tight constraints on the long-term thermal evolution of the magma reservoir. We show that zircon and titanite crystals record more than 600,000 years of magma assembly and constrain the dominant storage conditions to low temperatures, set between the granitic solidus (680 to 700 °C) and the temperature of the onset of titanite crystallisation (about 720 to 730 °C). We apply the zircon–titanite systematics to a suite of other super-eruptions and suggest that protracted low-temperature storage culminating in late-stage reheating is a widespread feature of large crystal-rich eruptions.

* *This chapter is equivalent to a paper published in* Nature Geoscience *(10, 777–782, 2017)*

2.1. Introduction

The physical conditions and timescales over which magma is accumulated and stored in reservoirs in the Earth's crust control the ability of such magma bodies to become reactivated and erupted (Bachmann and Bergantz, 2004; Burgisser and Bergantz, 2011; Huber et al., 2012; Caricchi et al., 2014; Parmigiani et al., 2014; Annen et al., 2015; Karakas et al., 2017). Hence, predicting the behaviour of magma reservoirs crucially depends on the knowledge of temperature, pressure and crystallinity of storage over time, as such factors affect the mechanical properties of the magma, as well as the rates at which the chemical and physical processes occur. Over the past two decades, many studies have found evidence for extended periods of crystallisation of accessory minerals prior to individual eruptions of up to several hundred thousand years (Reid et al., 1997; Brown and Fletcher, 1999; Vazquez and Reid, 2004; Charlier et al., 2005; Simon et al., 2008; Claiborne et al., 2010; Schmitt, 2011; Wotzlaw et al., 2013; Barboni et al., 2016; Kaiser et al., 2017). However, the temperature–crystallinity conditions of magma storage in the upper crust remain controversial, with recent interpretations ranging from those postulating storage dominantly in a 'warm' eruptible state (< 60 % crystalline; Barboni et al., 2016) to those preferring cold, immobile (even sub-solidus) storage where the eruptible state can only be achieved for brief periods immediately following recharge ('cold storage'; Cooper and Kent, 2014). These studies, dominantly focussed on small arc volcanoes, have limitations in only recording crystallisation (rather than storage) conditions of a relatively refractory phase (zircon) or in placing only relative constraints on storage temperature; for this reason, precise and absolute determinations of dominant magmatic storage temperature tied to time information remain elusive.

Here we present an approach combining high-precision U–Pb geochronology of zircon and titanite with mineral thermometry (Ferry and Watson, 2007; Hayden et al., 2008) of the dated crystals to precisely constrain both the time and temperature (and indirectly, crystallinity) of storage within supereruptive magma reservoirs. While recovering temperature information relating to the crystallisation conditions of both phases, we can take advantage of the limited thermal stability of titanite to place an upper boundary on the magnitude of thermal fluctuations and pre-eruptive reheating of such magma reservoirs. We first present a detailed study of zircon–titanite age and temperature systematics of the ~ 900 km^3 Kneeling Nun Tuff (KNT; New Mexico, USA) and then demonstrate that this mineral pair displays similar time–temperature systematics in other large-volume eruptions, suggesting that these supereruptive magma reservoirs follow a common route from storage to eruption.

2.2. Zircon–titanite age and temperature systematics

The Kneeling Nun Tuff represents one of the ten largest explosive eruptions in the geological record (Mason et al., 2004), produced in a caldera-forming supereruption within the Eocene–Oligocene Mogollon–Datil volcanic field (MDVF) in western New Mexico, United States (Elston, 1957; Giles, 1968; Elston et al., 1975; McIntosh et al., 1992) (Fig.

2.1a). The low- to high-silica rhyolitic KNT ignimbrite sheet has an average crystal content of 30–40 % (Giles, 1968), dominated by plagioclase, sanidine, quartz, biotite, hornblende, clinopyroxene, magnetite and ilmenite, with accessory titanite, zircon and apatite. Importantly, sanidine and titanite clearly record at least one cycle of dissolution and recrystallisation resulting in well-defined rims surrounding resorbed cores. The rims are enriched in specific trace elements (e.g. Ba, Sr, Ti, P and REE in sanidine; Fig. A2 and REE, Sr, Ba, Zr in titanite; Fig. 2.1b). These compositional and textural relationships suggest an extensive reheating event resulting in cumulate melting and a reduction in crystallinity (Wolff et al., 2015; Forni et al., 2016), similar to pre-eruptive reheating suggested for many other crystal-rich volcanic systems (Bachmann et al., 2002; Molloy et al., 2008; Huber et al., 2012; Pamukcu et al., 2013; Wotzlaw et al., 2013; Cooper and Kent, 2014; Barboni et al., 2016). Here, we studied the proximal outflow sheet of the KNT (Fig. 2.1a) representing the most typical crystallinity of 35 % characteristic for the bulk of the ignimbrite volume.

Employing ID–TIMS U–Pb geochronology (see Methods), we dated zircon and titanite crystals that were analysed for trace elements using *in situ* techniques prior to dissolution. While high-precision age determinations on zircon are relatively routine, dating titanite has been associated with large uncertainties related to (1) the assumed isotopic composition of initial Pb present in the titanite crystal lattice at the time of crystallisation, and (2) the extent of the initial ^{230}Th–^{238}U disequilibrium (Schmitz and Bowring, 2001; Schoene and Bowring, 2006). We corrected for these effects using (1) a well-constrained initial Pb isotopic composition measured in 15 leached sanidine crystals and crystal fragments (Fig. A4), and (2) a constant Th/U partition coefficient ratio ($D_{Th/U}$, Fig. A5) determined based on assumed equilibrium with zircon compositions. Despite these corrections, the precision of individual titanite dates approaches that achieved for zircon allowing us to resolve the timescales of pre-eruptive magma storage using two independent mineral chronometers (Fig. 2.1d, Table A1) that also record temperature and chemical variations with time (Figs 2.2 and 2.3).

Both Kneeling Nun Tuff zircons and titanites display a large range of individual grain $^{206}Pb/^{238}U$ crystallisation ages (Fig. 2.1d). While the youngest dates overlap the $^{40}Ar/^{39}Ar$ eruption age of 35.36 ± 0.08 Ma (McIntosh et al., 1990), titanite records a pre-eruptive period of 671 ± 211 ky of continuous or episodic crystallisation and zircons from the same sample span an equivalent range of 618 ± 56 ky (Fig. 2.1d). Trace elements in the studied crystals of both phases follow common chemical trends whereas Hf isotopes in zircon (Table A2) suggest only limited open-system behaviour, which together suggests that they derive from the same crustal magmatic system. Similar datasets of accessory phases that are chemically related but diverse in crystallisation ages have been interpreted to represent the long-term build-up of upper-crustal magma bodies (Reid et al., 1997; Brown and Fletcher, 1999; Bachmann and Bergantz, 2004; Vazquez and Reid, 2004; Claiborne et al., 2010; Schmitt, 2011; Wotzlaw et al., 2013; Barboni et al., 2016; Kaiser

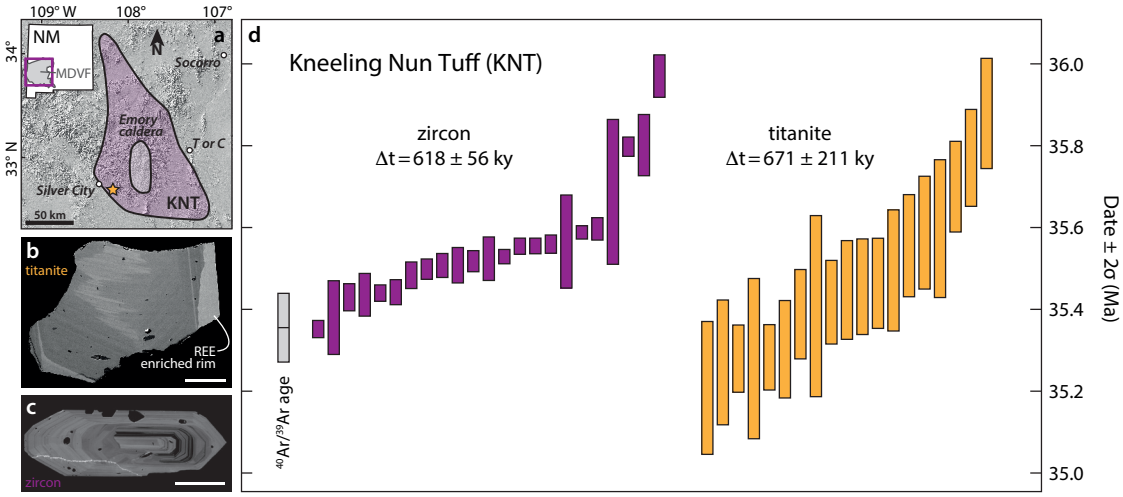

Figure 2.1. Zircon and titanite geochronology of the Kneeling Nun Tuff (KNT) magmatic system. (**a**) Map of the Mogollon–Datil volcanic field (MDVF, New Mexico [NM]) showing the extent of the KNT ignimbrite sheet around the source Emory caldera (McIntosh et al., 1992). The yellow star denotes sample location. (**b**) Backscattered electron image of a typical KNT titanite crystal. (**c**) Cathodoluminescence image of a typical KNT zircon crystal showing two growth domains. White scale bars are 100 µm long. (**d**) Individual single-grain $^{206}Pb/^{238}U$ dates of KNT zircon and titanite obtained in this study displayed with internal 2σ uncertainties including initial Pb correction uncertainties (see Methods). KNT $^{40}Ar/^{39}Ar$ age (McIntosh et al., 1990) (± 2σ) is recalculated using the calibration of Kuiper et al. (2008).

et al., 2017). We follow this interpretation while noting that the growth of a shallow magma reservoir need not be a linear process and that the preservation of crystals in the erupted products is likely enhanced for the younger part of the age population.

We assessed the thermal conditions of magma storage by combining two mineral thermometers based on Ti concentrations in zircon (Ferry and Watson, 2007) and Zr concentrations in titanite (Hayden et al., 2008). KNT zircons crystallised over a large range of temperature from 850 °C (equivalent to zircon saturation) to ~ 650 °C (equivalent to solidus; Holtz and Johannes, 1994) while titanites span a narrow range with cores and rims yielding indistinguishable temperatures centred at 726 ± 32 °C (Fig. 2.2). Trace element compositions of KNT zircons (e.g. Yb/Dy) support a fundamental role of titanite–zircon co-crystallisation at the lower end of the temperature spectrum; while high-T (> 726 °C) zircons may not have crystallised together with titanite, low-T (< 726 °C) zircons record a progressive increase in Yb/Dy (Fig. 2.2a). Simple trace element models confirm a key role of titanite (and hornblende) crystallisation in creating this signature (Fig. 2.2b). While compositional variations of the high-T zircons are explained by at least 35 % crystallisation of a titanite-free but hornblende-rich mineral assemblage, the compositions of low-T zircons are more easily produced by crystallising a titanite-bearing assemblage. Models based on measured modal abundances of minerals (1.6 wt % hornblende, 0.3 % titanite; Fig. A1) show that < 10 % crystallisation can explain the entire

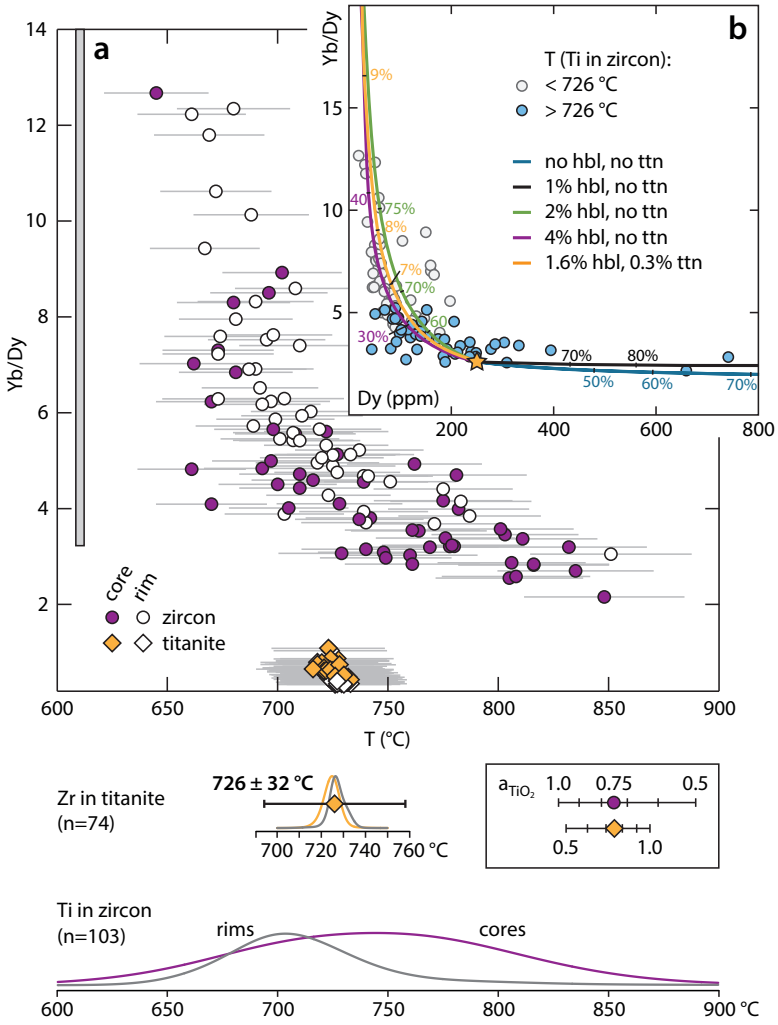

Figure 2.2. Accessory mineral trace element record and thermometry of the Kneeling Nun Tuff. (**a**) Zircon and titanite crystallisation temperatures based on Ti in zircon (Ferry and Watson, 2007) and Zr in titanite (Hayden et al., 2008) showing a large temperature range of zircon crystallisation and a narrow range for titanite at 726 ± 32 °C (2σ with propagated a_{TiO_2}, pressure and analytical uncertainties) with 2 °C of apparent difference between core and rim averages. Uncertainties on individual zircon and titanite temperatures (2σ) include analytical and thermometer calibration uncertainty (as well as pressure for titanite); the a_{TiO_2} used has a systematic yet opposite effect on the results of both models (see Methods and Fig. A8). Grey bar denotes the range of Yb/Dy_{zircon} in equilibrium with the Yb/Dy of KNT titanite using partitioning relations calculated from Rubatto and Hermann (2007) and Colombini et al. (2011). (**b**) Zircon trace element evolution scenarios as a function of the amount of hornblende and titanite in the crystallising mineral assemblage, calculated with modal proportions of the sample using partition coefficients of Bachmann et al. (2005) for major phases and of Colombini et al. (2011) for titanite and zircon. Percentages correspond to the fraction of an unevolved melt (star) removed into the crystallising mineral assemblage.

range of observed low-T zircon compositions. Such modelling suggests that the erupted part of the KNT magma reservoir reached a crystallinity of at least 45%, followed by a melting-induced reduction of the crystal content to ~35% at eruption. The data show that roughly half of the KNT zircons crystallised from a titanite-saturated melt below ca. 726 °C and above the lowest plausible crystallisation temperatures around the water-saturated solidus (T_{sol} = 680–700 °C) (Figs 2.2, 2.3).

We consider the Zr-in-titanite temperature constraint particularly robust due to the preservation of old U–Pb titanite ages (Fig. 2.1). Pb diffusion in titanite is faster than Zr diffusion (Cherniak, 2006), therefore the remarkable consistency of titanite temperatures is unlikely to result from diffusive resetting. The lack of titanites returning temperature lower than ca. 726 °C despite evidence for their crystallisation from zircon trace element signatures (Fig. 2.2a), together with common resorption textures of the studied crystals (Fig. 2.1b), suggest that such low-T titanite rims have been dissolved during the reheating event. In this scenario, the extent of pre-eruptive reheating was enough to obliterate all but few titanite cores recording the upper end of original titanite crystallisation temperature. At the same time, zircon crystals remained largely unaffected by the reheating, likely due to the zircon saturation temperature being considerably higher than titanite saturation temperature, the overall greater resistance and slow dissolution rates of zircon (Watson, 1996) or effects of shielding by other mineral phases. The apparent temperature difference between the lowest-temperature zircons (or the water-saturated solidus temperature; Holtz and Johannes, 1994) and the average titanite temperature (T_{ttn}) can be used to quantify the thermal effect of reheating prior to the KNT eruption (Fig. 2.4a). For our preferred a_{TiO2} of 0.75 (see Methods for details) the calculated temperature increase from the solidus at ~690 °C is ca. 35 °C, while the increase from the lowest-T zircon is 95 °C. For the extreme cases of a_{TiO2} of 0.5 and 1.0 the amount of reheating becomes 15 and 50 °C relative to the solidus, and 40–130 °C relative to the lowest-T zircon.

2.3. Thermal state of supereruptive magma bodies

The mean titanite crystallisation temperature (T_{ttn}, 726 ± 32 °C in the KNT) effectively places an upper boundary for the long-term thermal state of the bulk of a magma reservoir. Preservation of titanite crystals in the lowest crystallinity KNT (~35% crystals) up to 600,000 years older than the eruption requires that, even if spatially and temporally variable (Cooper and Kent, 2014; Barboni et al., 2016), the temperature of the bulk of the reservoir could not have exceeded T_{ttn} for a time long enough to reset the U–Pb system or dissolve all titanite crystals. In the KNT, temperature and trace element records show that most of the dated zircons crystallised below this temperature, with a dominant period of low-temperature zircon crystallisation at 35.6–35.5 Ma (Fig. 2.3a), similar to the occurrence of intermediate-age zircons in the Fish Canyon Tuff documenting a period of cooling to near-solidus conditions (Wotzlaw et al., 2013). Zircons younger than 35.5 Ma record generally higher temperature and a corresponding increase in Th/U

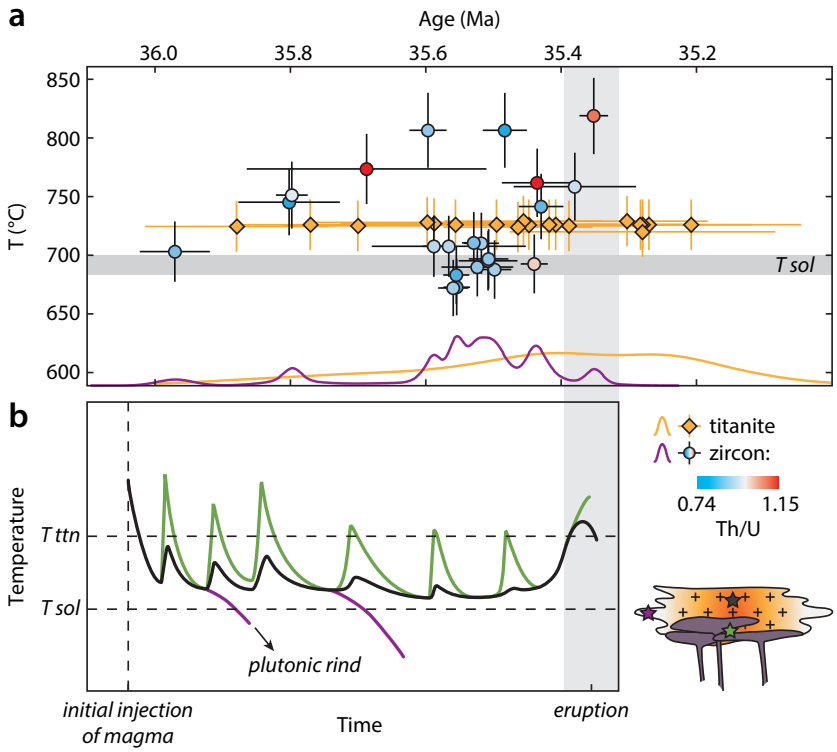

Figure 2.3. Temporal evolution of temperature within large silicic magmatic reservoirs. (**a**) Thermometry of the dated KNT zircon and titanite crystals based on single-spot trace element determinations or averages of multiple analyses of individual grains. Symbols representing zircons are colour-coded for their bulk-grain Th/U sensitive to titanite crystallisation/melting. Age distributions are presented as probability density functions along the bottom of the panel. (**b**) Schematic representation of the evolution of temperature in three regions of a mature, Kneeling Nun-like upper-crustal silicic magma reservoir: hot zone proximal to recharge (green), core or bulk of the reservoir volume (black) and cold non-eruptible rinds (purple).

indicating titanite dissolution, which may imply a prolonged period (~150,000 years) of pre-eruptive rejuvenation (cf. Wotzlaw et al., 2013). High-T zircons occur also before the proposed rejuvenation event, suggesting that such large magma reservoirs are heterogeneous in terms of their sensitivity to heat supplied by recharge magma.

Based on the observations of Kneeling Nun Tuff zircon and titanite crystals (as well as other phases in many eruptive units; Reid et al., 1997; Brown and Fletcher, 1999; Vazquez and Reid, 2004; Charlier et al., 2005; Schmitt, 2011; Wotzlaw et al., 2013; Cooper et al., 2016), we conclude that large (100s to 1000s km^3) magma reservoirs feeding supereruptions must be heterogeneously affected by recharge events, in turn producing complex time–temperature paths recorded by minerals in any specific sample, representing material mixed upon eruption (Fig. 2.3b). In particular, volumes of the reservoir adjacent to hot magma inputs from below are likely to experience pronounced spikes of temperature

(possibly up to the liquidus temperature, dissolving all pre-existing minerals). Peripheral parts of the reservoir, on the other hand, are less likely to see large temperature variations and more likely to fully solidify to form a plutonic rind. We argue that the core of such a supereruptive reservoir must be maintained in a high-crystallinity mush state at low temperature close to its solidus, relatively insensitive to recharge and buffered by a competition between conduction-dominated cooling, recharge heat supply, and latent heat released at these near-eutectic conditions (Huber et al., 2009; Morse, 2011; Annen et al., 2015; Karakas et al., 2017). Depending on the recharge rate, the storage conditions may end up being dominated by secular cooling, leading to pluton formation, or the reservoir may be reawakened to ultimately erupt a significant part of the mush zone (Bachmann et al., 2002; Bachmann and Bergantz, 2004; Burgisser and Bergantz, 2011; Huber et al., 2012; Pamukcu et al., 2013; Wotzlaw et al., 2013; Parmigiani et al., 2014; Barboni et al., 2016; Fig. 2.3b). However, the heat and volatile budgets necessary for the ultimate remobilisation by thermal reactivation of a large highly crystalline reservoir require that its core retains some melt throughout its lifetime (Huber et al., 2011; Parmigiani et al., 2014; Kaiser et al., 2017; Karakas et al., 2017). Our study shows that the temperature window in which most of the lifetime of such a reservoir is spent can be precisely constrained by employing accessory phase mineral thermometry.

2.4. Thermal effect of rejuvenation

The technique of combining thermometry based on zircon and titanite (or a similar combination of other accessory or major mineral phases) can be applied widely to both (1) constrain the dominant thermal conditions of magma storage and (2) evaluate the extent of pre-eruptive reheating in such magma reservoirs. A compilation of zircon and titanite trace element data for several well-studied supervolcanic eruptions reveals that low-temperature storage similar to that of KNT may be a widespread feature of such systems (Fig. 2.4a–d). In these cases, the partial survival of titanite through a pre-eruptive mush rejuvenation event independently documented by textural and compositional changes in major mineral phases allows the estimation of the temperature change as a result of reheating. In the Kneeling Nun Tuff and Fish Canyon Tuff (FCT), it is apparent that large volumes of the magma reservoir cooled down to near-solidus temperature and were reheated prior to eruption. The amount of reheating calculated as the temperature difference between the lowest-T zircon and the average titanite temperature (T_{ttn}) is 40–130 °C for KNT (Fig. 2.4a) and 35–130 °C for FCT (consistent with amphibole–plagioclase thermometry of Bachmann and Dungan, 2002; Fig. 2.4b). Taking the solidus temperature as the minimum temperature instead of the lowest-T zircon, these estimates become 15–50 °C and 35–80 °C, respectively. The Peach Spring Tuff is characterised by hotter storage with ca. 50 °C of reheating (Fig. 2.4c). Consistently with this scheme, the Masonic Park Tuff (Fig. 2.4d) displays the titanite crystallisation signature in zircon Yb/Dy despite the lack of observed titanite, which we interpret to reflect reheating to temperatures in excess of the titanite saturation temperature (T_{ttn}), resulting in complete dissolution of this mineral. Finally, magma bodies that did not ex-

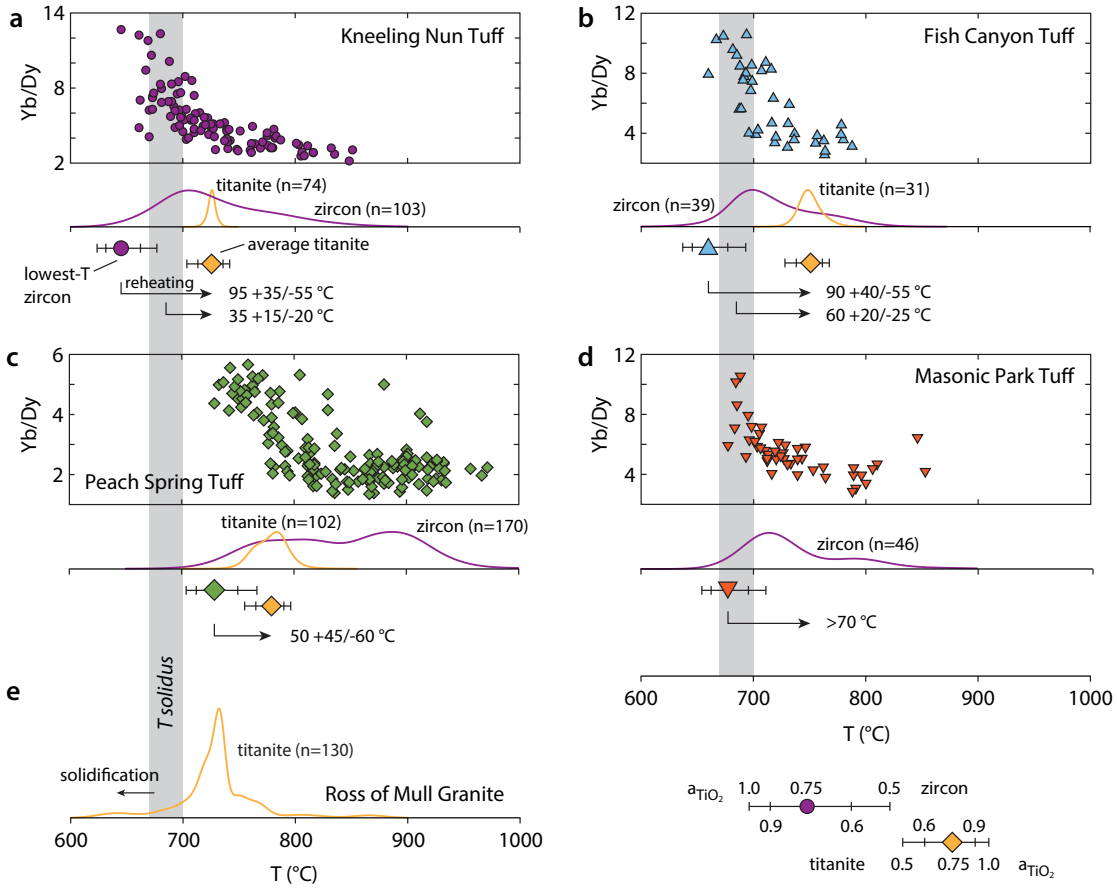

Figure 2.4. Ti-in-zircon and Zr-in-titanite thermometry of large volcanic magma reservoirs compared to a plutonic body. Large volcanic units of the western United States [Kneeling Nun Tuff (**a**), Fish Canyon Tuff (McLeod, 2007) (**b**), Peach Spring Tuff (Pamukcu et al., 2013) (**c**), and Masonic Park Tuff (Sliwinski et al., 2017) (**d**)] display a limited range of titanite crystallisation temperature despite evidence for zircon–titanite co-crystallisation (increase in Yb/Dy_{zircon} below T_{ttn}), allowing for an estimate of the thermal effect of pre-eruptive reheating (arrows). The Ross of Mull Granite, Scotland (McLeod et al., 2011) (**e**) has a wide range of Zr-in-titanite temperatures including sub-solidus (< 670 °C) values. For comparison, all temperatures are calculated (Ferry and Watson, 2007; Hayden et al., 2008) with $a_{TiO_2} = 0.75$, $a_{SiO_2} = 1.0$ and P = 0.25 GPa (0.15 GPa for KNT). Varying a_{TiO_2} has opposite effects on temperature returned by both thermometers, resulting in an increase (with an increase in a_{TiO_2}) or a decrease (with a decrease in a_{TiO_2}) of the estimated amount of heating.

perience such reheating and did not erupt (i.e. plutons) should show a greater range of titanite crystallisation temperatures including some that indicate sub-solidus crystallisation (< 670 °C) (Fig. 2.4e). A pronounced pre-eruptive rejuvenation is likely a common feature of many, if not all, crystal-rich magma reservoirs and its thermal effect can be demonstrated in wet, oxidised magmas by combining titanite and zircon trace element geochemistry. Extending this interpretation to hot and dry magmatic settings characterised by early ilmenite saturation, resulting in limited titanite stability (Xirouchakis et al., 2001), requires an alternative approach (e.g. Matthews et al., 2015; Stelten et al.,

2015; Till et al., 2015). Our study shows that the combination of precise dating and trace element geochemistry/thermometry on accessory minerals can provide unprecedented resolution in studies of the petrological evolution of upper crustal magma bodies, recording the storage conditions and thermal rejuvenation of such reservoirs prior to some of the largest eruptions in the geological record.

2.5. Methods

2.5.1. Sample preparation and characterisation

Zircon, titanite and feldspar crystals were separated from a Kneeling Nun Tuff sample by crushing with a SELFRAG high-voltage fragmentation device followed by standard heavy liquid and magnetic separation procedures, with the final concentrates hand-picked under a binocular microscope. Selected zircon crystals were placed in quartz crucibles and annealed for 48 h at 900 °C in a muffle furnace. All grains were mounted in epoxy, polished and imaged with backscattered electrons (BSE, titanite and feldspar) or cathodoluminescence (CL, zircon) using a JEOL JSM-6390 LA scanning electron microscope at ETH Zürich. Trace element concentrations in all phases were determined using LA-ICPMS on a Thermo Element XR ICPMS coupled to an ASI Resolution 155 LR ArF excimer laser, with a spot diameter of 30 µm. NIST 610/612 glass was used as reference material and Si (zircon, feldspar) and Ca (titanite) as internal standard. Most trace elements have uncertainties better than ± 5 % (2 RSD) based on glass standard reproducibility. Repeat analyses of secondary zircon reference material GJ-1 yielded external reproducibility of ± 17.8 % for Ti, 4.5 % for Dy, 4.0 % for Yb/Dy and 2.6 % for Th/U (all 2 RSD). GJ-1 zircon has significantly lower trace element concentrations than the KNT zircon (except for Ti), suggesting that the uncertainties quoted can be considered maximum uncertainties. The uncertainties of measured Zr contents in titanite can be approximated by the reproducibility of a homogeneous glass standard ATHO-G (512 ppm Zr) yielding an external reproducibility of 1.0 % (2 RSD).

2.5.2. Dissolution and U–Pb chemistry

Selected individual zircon crystals were extracted from the epoxy mounts, rinsed with 4 N HNO_3 and loaded into 300 µl Savillex microcapsules for partial dissolution ('chemical abrasion') in ~ 70 µl 29 N HF + trace HNO_3 at 180 °C for 12 h in a pressure vessel (Mattinson, 2005). Residual crystals were transferred into 3 ml Savillex beakers, fluxed in 6 N HCl on a hotplate and cleaned twice in 4 N HNO_3 in ultrasonic bath before loading back into their pre-cleaned microcapsules with a microdrop of 7 N HNO_3 and ~ 70 µl 29 N HF. The zircon samples were spiked with 6–10 mg of the EARTHTIME ^{202}Pb–^{205}Pb–^{233}U–^{235}U tracer solution (Condon et al., 2015; McLean et al., 2015) and dissolved in pressure vessels for ~60 h at 210 °C. After dissolution, samples were dried down and redissolved in 50 µl 6 N HCl at 180 °C for ~ 12 h to convert to chlorides, then dried down in preparation for ion exchange chemistry. Titanite preparation did not include the chemical abrasion step; selected grains or grain domains (where REE-enriched rims

were cut off to isolate cores) extracted from epoxy mounts and free of adhering resin were washed three times with 4 N HNO_3 in ultrasonic bath prior to dissolution. Titanite samples were spiked with 6–12 mg of the EARTHTIME ^{205}Pb–^{233}U–^{235}U tracer and dissolved in a procedure identical to that of zircon. Pb and U were separated using an HCl-based (zircon) or a two stage HBr–HCl-based (titanite) single-column anion exchange chemistry procedure modified from Krogh (1973). The resulting fractions (either U–Pb for zircon or separate U and Pb for titanite) were dried down with a drop of 0.02 M H_3PO_4.

Selected mm-sized sanidine crystals embedded in epoxy were fractured with a razor blade and resulting fragments belonging to different compositional domains were extracted as separate samples for Pb isotopic analyses. In order to dissolve potential inclusions hosted in the feldspar and remove any present ingrown radiogenic Pb component (Chiaradia and Fontboté, 2003), the samples were leached at 120 °C in 0.5 ml 6 N HCl + 0.5 ml 7.5 N HNO_3 during ~ 20 h in 3 ml screw-sealed Teflon beakers, with ultrasonication for 20 min after ~ 12 h. The residues were washed twice with deionised water for 15 min in ultrasound and loaded into 7 ml beakers for dissolution with 0.5 ml 7.5 N HNO_3 + 1.5 ml 29 N HF at 160 °C for ≥ 72 h. The solutions were dried down and redissolved in 0.5 ml 7.5 N HNO_3 at 160 °C for another 72 h, then dried again and redissolved in 0.5 ml 6 N HCl for several hours. The samples in chloride form were dried down and taken up in 1 N HBr for Pb separation by HBr-based anion exchange chemistry on microcolumns similar to the procedure used for titanite. Total procedural blanks were measured at < 5 pg Pb which is considered negligible compared to the ~ng Pb feldspar sample size.

2.5.3. Mass spectrometry and data reduction

U–Pb fractions were loaded on single outgassed Re filaments with a silica gel emitter modified from Gerstenberger and Haase (1997). Both elements were measured on a Thermo TRITON Plus thermal ionisation mass spectrometer (TIMS) at ETH Zürich. Pb isotopes were measured either: (1) in dynamic mode on a MasCom secondary electron multiplier (SEM; zircon); (2) in full static mode measuring ^{204}Pb, ^{206}Pb, ^{207}Pb, and ^{208}Pb in Faraday cups equipped with 10^{13} Ω resistors (feldspar); or (3) in a combined routine measuring ^{205}–^{208}Pb in H1–H4 Faraday cups with 10^{13} Ω resistors and ^{204}Pb in the axial SEM in the first line followed by a short measurement of ^{205}Pb in the SEM allowing for online detector yield correction (titanite) (see Wotzlaw et al., 2017 for details). Pb isotopic fractionation during zircon measurements was corrected using factors derived from the measured $^{202}Pb/^{205}Pb$ normalised to the true value of 0.99924 (Condon et al., 2015); for titanite and feldspar analyses the Pb mass fractionation factor was 0.094 ± 0.06 %/a.m.u. (2σ), based on repeat Faraday cup measurements of the NBS 982 standard over the course of the study. U was measured as oxides with $^{265}(UO_2)$, $^{267}(UO_2)$ and $^{270}(UO_2)$ collected in Faraday cups connected to amplifiers with 10^{13} Ω resistors(von Quadt et al., 2016). U isotopic ratios were corrected for isobaric interferences of $^{233}U^{18}O^{16}O$ on $^{235}U^{16}O_2$ using an $^{18}O/^{16}O$ of 0.00205 ± 0.00005 (2σ) and for mass fractionation using the measured $^{233}U/^{235}U$ ra-

tio relative to the true value of 0.99506 (Condon et al., 2015) and a sample $^{238}U/^{235}U$ of 137.818 ± 0.045 (Hiess et al., 2012). Data reduction was performed using the Tripoli and U-Pb Redux software packages (Bowring et al., 2011) employing data reduction and uncertainty propagation algorithms of McLean et al. (2011). U–Pb ratios and dates were calculated relative to a tracer $^{235}U/^{205}Pb$ ratio of 100.23 ± 0.046 % (2σ) and using the decay constants of Jaffey et al. (1971). All common Pb in zircon analyses was attributed to laboratory blank and corrected with the average composition of total procedural blank measurements ($^{206}Pb/^{204}Pb$ = 18.41 ± 0.39, $^{207}Pb/^{204}Pb$ = 15.19 ± 0.39, $^{208}Pb/^{204}Pb$ = 36.93 ± 0.91, 2σ, n = 14). For titanite chemistry, total procedural blanks averaged (1) 1.14 ± 0.75 pg (2σ) and (2) 0.45 ± 0.24 pg for two separate sets of samples prepared over the course of several months; consequently, two compositions were used for laboratory blank corrections: (1) $^{206}Pb/^{204}Pb$ = 19.70 ± 0.60, $^{207}Pb/^{204}Pb$ = 15.72 ± 0.43, $^{208}Pb/^{204}Pb$ = 38.82 ± 1.11 (2σ; n = 5) and (2) $^{206}Pb/^{204}Pb$ = 18.84 ± 1.35, $^{207}Pb/^{204}Pb$ = 15.63 ± 0.71, $^{208}Pb/^{204}Pb$ = 38.34 ± 1.61 (2σ; n = 4). The accuracy of TIMS U and Pb isotope ratio measurements was monitored by routine analyses of NBS 982 Pb standard as well as U–Pb synthetic solutions and standard zircons throughout the period of the study (analyses compiled in Wotzlaw et al., 2017 and von Quadt et al., 2016).

2.5.4. Common Pb correction in titanite

During crystallisation titanite incorporates variable amounts of non-radiogenic Pb (present Pb*/Pbc = 0.6–0.8, Table A1). The accuracy of U/Pb titanite dates is thus limited by the necessity of correcting for the isotopic composition of this initial non-radiogenic Pb present in excess of the Pb formed by the decay of U and Th. In this study, the amount of non-radiogenic (common) Pb measured in each titanite sample was partitioned between the laboratory blank (see above) and the initial Pb component. The isotopic composition of initial Pb was determined on fragments of sanidine from the same sample, assuming that this mineral crystallised in isotopic equilibrium with the dated titanite. The low U and Th contents of sanidine minimise the amount of subsequent radiogenic ingrowth, nonetheless in order to recover the least radiogenic Pb isotopic compositions an additional leaching procedure modified from Chiaradia and Fontboté (2003) was applied prior to dissolution (see above). A total of 15 samples were analysed of both sanidine cores and high-Ba rims, yielding a range of Pb isotopic compositions (Fig. A4, Table A3). No systematic differences were observed between the cores and the rims except a single rim analysis that was markedly less radiogenic in Pb isotopic composition (Fig. A4). The range of results indicates substantial isotopic homogeneity of KNT sanidine; our preferred value used for initial Pb correction of all titanite analyses is the average of five measurements (4 cores + 1 rim) clustering at the least radiogenic end of the range, where the propagated uncertainties are standard deviations of that population: $^{206}Pb/^{204}Pb$ = 17.944 ± 0.017, $^{207}Pb/^{204}Pb$ = 15.498 ± 0.019, $^{208}Pb/^{204}Pb$ = 38.111 ± 0.069 (2σ). The outlying unradiogenic rim analysis was excluded based on trace element contents that suggest an involvement of late recharge magma potentially violating the requirement of sanidine–titanite isotopic equilibrium. The uncertainties on initial Pb isotop-

ic composition including error correlations calculated following Schmitz and Schoene (2007) are fully propagated into all titanite dates.

2.5.5. Initial ^{230}Th–^{238}U disequilibrium correction

The fractionation of Th and U during crystallisation of zircon and titanite results in an enrichment (titanite, $D^{Th/U}_{mineral-melt} > 1$) or a depletion (zircon, $D^{Th/U}_{mineral-melt} < 1$) in ^{230}Th, a long-lived intermediate daughter product in the ^{238}U–^{206}Pb decay chain, leading to a ^{206}Pb deficit (zircon) or ^{206}Pb excess (titanite) translating into too young or too old ^{206}Pb/^{238}U dates, respectively (see e.g. Schoene, 2014). The initial disequilibrium can be corrected following Schärer (1984) by estimating the Th/U partitioning between the melt and the crystals, with the Th/U in the mineral calculated based on the measured radiogenic ^{208}Pb (assuming concordance between the U–Pb and Th–Pb systems). Based on the long-lived nature of the studied system and variable Th/U recorded by zircons, we assumed constant mineral/melt Th/U distribution coefficients ($D_{Th/U}$) for both zircon and titanite, where the variability in mineral Th/U is assumed to only be a result of changing melt composition. For zircon, the $D_{Th/U}$ used was based on a compilation of experimental data (Rubatto and Hermann, 2007) and natural examples (Fukuoka and Kigoshi, 1974; Blundy and Wood, 2003; Bindeman et al., 2006; Guillong et al., 2014; Stelten et al., 2015), including titanite-bearing systems (Bachmann et al., 2005; Colombini et al., 2011), yielding an average value of 0.218 ± 0.097 (2σ; Fig. A5). The partitioning of U and Th between titanite and melt is relatively poorly established, with experimental studies (Tiepolo et al., 2002; Prowatke and Klemme, 2005) reporting lower values than those found in natural phenocryst–glass pairs (Bachmann et al., 2005; Colombini et al., 2011; Olin and Wolff, 2012; Padilla and Gualda, 2016; Fig. A5). In order to derive an accurate titanite $D_{Th/U}$ we took advantage of the relatively well-constrained zircon $D_{Th/U}$. Most zircons crystallised from a titanite-saturated melt (Fig. 2.3), therefore we made a choice of titanite–melt $D_{Th/U}$ such that on average the Th/U_{melt} given by titanite–melt partitioning corresponds to the average Th/U_{melt} calculated from zircon compositions. The average Th/U_{melt} calculated from zircons is equal to 4.1, which gave titanite–melt $D_{Th/U} = 1.96$, a value lying in the middle of the range of the compiled data (Fig. A5). The Th/U disequilibrium correction translates into +84.9 ka for zircon and –104.5 ka for titanite. Uncertainties on the partition coefficients were not propagated into final age uncertainties as with fixed $D_{Th/U}$ they are considered systematic for all the grains (Barboni and Schoene, 2014; Ickert et al., 2015). In particular, the absolute age differences between grains are insensitive to the disequilibrium correction and could be assessed without applying it, however with a potential loss of accuracy (Schoene, 2014).

2.5.6. Hf isotope analysis

Hf isotopic compositions of single zircons (Table A2) were analysed in eluted fractions remaining from U–Pb anion exchange chemistry. Hf was separated from the matrix using an HCl–HF-based ion exchange chemistry using Ln-spec resin and analysed on a Nu Plasma II MC-ICPMS at ETH Zürich. All ^{176}Hf/^{177}Hf isotope ratios were normalised to

the JMC475 standard (recommended value of $^{176}Hf/^{177}Hf = 0.282160$; Vervoort and Blichert-Toft, 1999), which returned reproducible values over the course of three sessions at 0.282186 ± 10 (2σ, $n = 29$), 0.282168 ± 14 (2σ, $n = 25$) and 0.282189 ± 14 (2σ, $n = 27$). The ratios were corrected for *in situ* radiogenic ingrowth of ^{176}Hf using the ^{176}Lu decay constant of Scherer et al. (2001), with $^{176}Lu/^{177}Hf$ derived from Lu/Hf measured via LA-ICPMS. All reported uncertainties include the within-run precision of each measurement and the reproducibility of the JMC475 standard.

2.5.7. Mineral thermometry

The calculation of zircon and titanite crystallisation temperatures was performed using the formulations of Ferry and Watson (2007) for zircon and Hayden et al. (2008) for titanite. The thermometers are based on the measured concentrations of Ti in zircon and Zr in titanite and require assumptions about the activity of TiO_2 and SiO_2 in the melt, as well as pressure included only in the Zr-in-titanite calibration. The SiO_2 activity was set to 1.0 based on the presence of quartz. The TiO_2 activity (a_{TiO2}) was taken to be 0.75 to resemble values estimated for the Fish Canyon Tuff (Ghiorso and Gualda, 2013) belonging to the same period of volcanism as KNT, with a similar tectonic setting, mineral assemblage, and likely oxygen fugacity (Bachmann et al., 2002). We did not take into account the variability of a_{TiO2} with temperature or the crystallising phase assemblage, but rather chose a preferred constant value and explored the effects of varying a_{TiO2} between plausible endmember values for wet and oxidised, titanite-bearing systems, $a_{TiO2} = 0.5$ and 1.0 (Ghiorso and Gualda, 2013) (Figs 2.2, 2.4, A8). Pressure of storage was estimated to be between < 50 MPa and ~175 MPa using the method of Blundy and Cashman (2001) and compositions of glass from rare quenched parts of the caldera fill, with a preferred value of 0.15 ± 0.15 GPa used in all calculations. We consider the Zr-in-titanite temperatures robust as they are relatively insensitive to changes in pressure and a_{TiO2} (Fig. A7, A8). The Ti-in-zircon temperatures are used here primarily for their ability to record trends in the entire dataset, however their absolute accuracy may be limited e.g. by the uncertain pressure dependence of the thermometer (Ferry and Watson, 2007; Ferriss et al., 2008). Changing the assumed TiO_2 activity (Fig. A8) has opposite effects on temperature returned by both thermometers, where an increase in a_{TiO2} results in expanding the postulated window of storage temperature, while a decrease in a_{TiO2} collapses that window and shifts it to lower absolute temperature. In particular, eliminating the zircon–titanite temperature difference in the KNT completely requires $a_{TiO2} \sim 0.3–0.4$, which appears unreasonably low for an oxidised, titanite-bearing system (Ghiorso and Gualda, 2013).

Acknowledgements

This work was supported by Swiss National Science Foundation (SNF) grant 200021–155923. J.F.W. acknowledges support through the ETH Zurich Postdoctoral Fellowship Program. The authors are grateful to J. Sliwinski for FCT and MPT zircon trace element data and Y. Buret for help with Hf isotopic analyses. Special thanks to C. Klemp and

K. Cook from Freeport–McMoRan Inc. for facilitating access to outcrops near Chino Mine, New Mexico.

Appendix

Supplementary information to this chapter can be found in Appendix A.

References

Annen, C., Blundy, J.D., Leuthold, J., Sparks, R.S.J., 2015. Construction and evolution of igneous bodies: Towards an integrated perspective of crustal magmatism. Lithos 230, 206-221.

Bachmann, O., Bergantz, G.W., 2004. On the origin of crystal-poor rhyolites: Extracted from batholithic crystal mushes. J. Petrol. 45, 1565-1582.

Bachmann, O., Dungan, M.A., 2002. Temperature-induced Al-zoning in hornblendes of the Fish Canyon magma, Colorado. Am. Mineral. 87, 1062-1076.

Bachmann, O., Dungan, M.A., Bussy, F., 2005. Insights into shallow magmatic processes in large silicic magma bodies: the trace element record in the Fish Canyon magma body, Colorado. Contrib. Mineral. Petrol. 149, 338-349.

Bachmann, O., Dungan, M.A., Lipman, P.W., 2002. The Fish Canyon magma body, San Juan volcanic field, Colorado: Rejuvenation and eruption of an upper-crustal batholith. J. Petrol. 43, 1469-1503.

Barboni, M., Boehnke, P., Schmitt, A.K., Harrison, T.M., Shane, P., Bouvier, A.-S., Baumgartner, L., 2016. Warm storage for arc magmas. Proc. Natl. Acad. Sci. USA 113, 13959-13964.

Barboni, M., Schoene, B., 2014. Short eruption window revealed by absolute crystal growth rates in a granitic magma. Nat. Geosci. 7, 524-528.

Bindeman, I.N., Schmitt, A.K., Valley, J.W., 2006. U–Pb zircon geochronology of silicic tuffs from the Timber Mountain/Oasis Valley caldera complex, Nevada: rapid generation of large volume magmas by shallow-level remelting. Contrib. Mineral. Petrol. 152, 649-665.

Blundy, J., Cashman, K., 2001. Ascent-driven crystallisation of dacite magmas at Mount St Helens, 1980-1986. Contrib. Mineral. Petrol. 140, 631-650.

Blundy, J., Wood, B., 2003. Mineral-melt partitioning of uranium, thorium and their daughters. Rev. Mineral. Geochem. 52, 59-123.

Bowring, J.F., McLean, N.M., Bowring, S.A., 2011. Engineering cyber infrastructure for U-Pb geochronology: Tripoli and U-Pb_Redux. Geochem. Geophys. Geosyst. 12, Q0AA19.

Brown, S.J.A., Fletcher, I.R., 1999. SHRIMP U-Pb dating of the preeruption growth history of zircons from the 340 ka Whakamaru Ignimbrite, New Zealand: Evidence for >250 k.y. magma residence times. Geology 27, 1035-1038.

Burgisser, A., Bergantz, G.W., 2011. A rapid mechanism to remobilize and homogenize highly crystalline magma bodies. Nature 471, 212-215.

Caricchi, L., Simpson, G., Schaltegger, U., 2014. Zircons reveal magma fluxes in the Earth's crust. Nature 511, 457-461.

Charlier, B., Wilson, C., Lowenstern, J., Blake, S., Van Calsteren, P., Davidson, J., 2005. Magma generation at a large, hyperactive silicic volcano (Taupo, New Zealand) revealed by U–Th and U–Pb systematics in zircons. J. Petrol. 46, 3-32.

Cherniak, D.J., 2006. Zr diffusion in titanite. Contrib. Mineral. Petrol. 152, 639-647.

Chiaradia, M., Fontboté, L., 2003. Separate lead isotope analyses of leachate and residue rock fractions: implications for metal source tracing in ore deposit studies. Miner. Deposita 38, 185-195.

Claiborne, L.L., Miller, C.F., Flanagan, D.M., Clynne, M.A., Wooden, J.L., 2010. Zircon reveals protracted magma storage and recycling beneath Mount St. Helens. Geology 38, 1011-1014.

Colombini, L.L., Miller, C.F., Gualda, G.A.R., Wooden, J.L., Miller, J.S., 2011. Sphene and zircon in the Highland Range volcanic sequence (Miocene, southern Nevada, USA): elemental partitioning, phase relations, and influence on evolution of silicic magma. Mineral. Petrol. 102, 29-50.

Condon, D.J., Schoene, B., McLean, N.M., Bowring, S.A., Parrish, R.R., 2015. Metrology and traceability of U–Pb isotope dilution geochronology (EARTHTIME Tracer Calibration

Part I). Geochim. Cosmochim. Acta 164, 464-480.

Cooper, G.F., Wilson, C.J.N., Millet, M.A., Baker, J.A., 2016. Generation and rejuvenation of a supervolcanic magmatic system: a case study from Mangakino volcanic centre, New Zealand. J. Petrol. 57, 1135-1170.

Cooper, K.M., Kent, A.J.R., 2014. Rapid remobilization of magmatic crystals kept in cold storage. Nature 506, 480-483.

Elston, W.E., 1957. Geology and mineral resources of Dwyer quadrangle, Grant, Luna, and Sierra Counties, New Mexico. N.M. Bur. Mines Miner. Res. Bull. 38.

Elston, W.E., Seager, W.R., Clemons, R.E., 1975. Emory Cauldron, Black Range, New Mexico, source of the Kneeling Nun Tuff, in: Seager, W.R., Clemons, R.E., Callender, J.F. (Eds.), N.M. Geol. Soc. 26th Fall Field Conf. Guidebook, pp. 283–292.

Ferriss, E.D., Essene, E.J., Becker, U., 2008. Computational study of the effect of pressure on the Ti-in-zircon geothermometer. Eur. J. Mineral. 20, 745-755.

Ferry, J.M., Watson, E.B., 2007. New thermodynamic models and revised calibrations for the Ti-in-zircon and Zr-in-rutile thermometers. Contrib. Mineral. Petrol. 154, 429-437.

Forni, F., Bachmann, O., Mollo, S., De Astis, G., Gelman, S.E., Ellis, B.S., 2016. The origin of a zoned ignimbrite: Insights into the Campanian Ignimbrite magma chamber (Campi Flegrei, Italy). Earth Planet. Sci. Lett. 449, 259-271.

Fukuoka, T., Kigoshi, K., 1974. Discordant Io-ages and the uranium and thorium distribution between zircon and host rocks. Geochem. J. 8, 117-122.

Gerstenberger, H., Haase, G., 1997. A highly effective emitter substance for mass spectrometric Pb isotope ratio determinations. Chem. Geol. 136, 309-312.

Ghiorso, M.S., Gualda, G.A.R., 2013. A method for estimating the activity of titania in magmatic liquids from the compositions of coexisting rhombohedral and cubic iron-titanium oxides. Contrib. Mineral. Petrol. 165, 73-81.

Giles, D.L., 1968. Ash-flow tuffs of the Cobre Mountains, in: Titley, S.R. (Ed.), Arizona Geological Society Southern Arizona Guidebook III, pp. 289–291.

Guillong, M., von Quadt, A., Sakata, S., Peytcheva, I., Bachmann, O., 2014. LA-ICP-MS Pb-U dating of young zircons from the Kos–Nisyros volcanic centre, SE Aegean arc. J. Anal. At. Spectrom. 29, 963-970.

Hayden, L.A., Watson, E.B., Wark, D.A., 2008. A thermobarometer for sphene (titanite). Contrib. Mineral. Petrol. 155, 529-540.

Hiess, J., Condon, D.J., McLean, N., Noble, S.R., 2012. $^{238}U/^{235}U$ systematics in terrestrial uranium-bearing minerals. Science 335, 1610-1614.

Holtz, F., Johannes, W., 1994. Maximum and minimum water contents of granitic melts: implications for chemical and physical properties of ascending magmas. Lithos 32, 149-159.

Huber, C., Bachmann, O., Dufek, J., 2011. Thermo-mechanical reactivation of locked crystal mushes: Melting-induced internal fracturing and assimilation processes in magmas. Earth Planet. Sci. Lett. 304, 443-454.

Huber, C., Bachmann, O., Dufek, J., 2012. Crystal-poor versus crystal-rich ignimbrites: A competition between stirring and reactivation. Geology 40, 115-118.

Huber, C., Bachmann, O., Manga, M., 2009. Homogenization processes in silicic magma chambers by stirring and mushification (latent heat buffering). Earth Planet. Sci. Lett. 283, 38-47.

Ickert, R.B., Mundil, R., Magee Jr, C.W., Mulcahy, S.R., 2015. The U–Th–Pb systematics of zircon from the Bishop Tuff: A case study in challenges to high-precision Pb/U geochronology at the millennial scale. Geochim. Cosmochim. Acta 168, 88-110.

Jaffey, A.H., Flynn, K.F., Glendenin, L.E., Bentley, W.C., Essling, A.M., 1971. Precision measurement of half-lives and specific activities of 235U and 238U. Phys. Rev. C 4, 1889-1906.

Kaiser, J.F., de Silva, S., Schmitt, A.K., Economos, R., Sunagua, M., 2017. Million-year melt–presence in monotonous intermediate magma for a volcanic–plutonic assemblage in the Central Andes: Contrasting histories of crystal-rich and crystal-poor super-sized silicic magmas. Earth Planet. Sci. Lett. 457, 73-86.

Karakas, O., Degruyter, W., Bachmann, O., Dufek, J., 2017. Lifetime and size of shallow magma bodies controlled by crustal-scale magmatism. Nat. Geosci. 10, 446-450.

Krogh, T.E., 1973. A low-contamination method for hydrothermal decomposition of zircon and extraction of U and Pb for isotopic age determinations. Geochim. Cosmochim. Acta 37, 485-494.

Kuiper, K.F., Deino, A., Hilgen, F.J., Krijgsman, W., Renne, P.R., Wijbrans, J.R., 2008. Synchronizing rock clocks of Earth history. Science 320, 500-504.

Mason, B.G., Pyle, D.M., Oppenheimer, C., 2004. The size and frequency of the largest explosive eruptions on Earth. Bull. Volcanol. 66, 735-748.

Matthews, N.E., Vazquez, J.A., Calvert, A.T., 2015. Age of the Lava Creek supereruption and magma chamber assembly at Yellowstone based on $^{40}Ar/^{39}Ar$ and U–Pb dating of sanidine and zircon crystals. Geochem. Geophys. Geosyst. 16, 2508-2528.

Mattinson, J.M., 2005. Zircon U–Pb chemical abrasion ("CA-TIMS") method: Combined annealing and multi-step partial dissolution analysis for improved precision and accuracy of zircon ages. Chem. Geol. 220, 47-66.

McIntosh, W.C., Chapin, C.E., Ratté, J.C., Sutter, J.F., 1992. Time-stratigraphic framework for the Eocene-Oligocene Mogollon-Datil volcanic field, southwest New Mexico. Geol. Soc. Am. Bull. 104, 851-871.

McIntosh, W.C., Sutter, J.F., Chapin, C.E., Kedzie, L.L., 1990. High-precision $^{40}Ar/^{39}Ar$ sanidine geochronology of ignimbrites in the Mogollon-Datil volcanic field, southwestern New Mexico. Bull. Volcanol. 52, 584-601.

McLean, N.M., Bowring, J.F., Bowring, S.A., 2011. An algorithm for U-Pb isotope dilution data reduction and uncertainty propagation. Geochem. Geophys. Geosyst. 12, Q0AA18.

McLean, N.M., Condon, D.J., Schoene, B., Bowring, S.A., 2015. Evaluating uncertainties in the calibration of isotopic reference materials and multi-element isotopic tracers (EARTHTIME Tracer Calibration Part II). Geochim. Cosmochim. Acta 164, 481-501.

McLeod, G.W., 2007. Titanite zoning and magma mixing. PhD Thesis, University of Glasgow.

McLeod, G.W., Dempster, T.J., Faithfull, J.W., 2011. Deciphering magma-mixing processes using zoned titanite from the Ross of Mull Granite, Scotland. J. Petrol. 52, 55-82.

Molloy, C., Shane, P., Nairn, I., 2008. Pre-eruption thermal rejuvenation and stirring of a partly crystalline rhyolite pluton revealed by the Earthquake Flat Pyroclastics deposits, New Zealand. J. Geol. Soc. London 165, 435-447.

Morse, S.A., 2011. The fractional latent heat of crystallizing magmas. Am. Mineral. 96, 682-689.

Olin, P.H., Wolff, J.A., 2012. Partitioning of rare earth and high field strength elements between titanite and phonolitic liquid. Lithos 128-131, 46-54.

Padilla, A.J., Gualda, G.A.R., 2016. Crystal-melt elemental partitioning in silicic magmatic systems: An example from the Peach Spring Tuff high-silica rhyolite, Southwest USA. Chem. Geol. 440, 326-344.

Pamukcu, A.S., Carley, T.L., Gualda, G.A., Miller, C.F., Ferguson, C.A., 2013. The evolution of the Peach Spring giant magma body: Evidence from accessory mineral textures and compositions, bulk pumice and glass geochemistry, and rhyolite-MELTS modeling. J. Petrol. 54, 1109-1148.

Parmigiani, A., Huber, C., Bachmann, O., 2014. Mush microphysics and the reactivation of crystal-rich magma reservoirs. J. Geophys. Res. 119, 6308-6322.

Prowatke, S., Klemme, S., 2005. Effect of melt composition on the partitioning of trace elements between titanite and silicate melt. Geochim. Cosmochim. Acta 69, 695-709.

Reid, M.R., Coath, C.D., Harrison, T.M., McKeegan, K.D., 1997. Prolonged residence times for the youngest rhyolites associated with Long Valley Caldera: $^{230}Th–^{238}U$ ion microprobe dating of young zircons. Earth Planet. Sci. Lett. 150, 27-39.

Rubatto, D., Hermann, J., 2007. Experimental zircon/melt and zircon/garnet trace element partitioning and implications for the geochronology of crustal rocks. Chem. Geol. 241, 38-61.

Schärer, U., 1984. The effect of initial ^{230}Th disequilibrium on young U-Pb ages: the Makalu case, Himalaya. Earth Planet. Sci. Lett. 67, 191-204.

Scherer, E., Münker, C., Mezger, K., 2001. Calibration of the lutetium-hafnium clock. Science 293, 683-687.

Schmitt, A.K., 2011. Uranium series accessory crystal dating of magmatic processes. Annu. Rev. Earth Planet. Sci. 39, 321-349.

Schmitz, M.D., Bowring, S.A., 2001. U-Pb zircon and titanite systematics of the Fish Canyon Tuff: an assessment of high-precision U-Pb geochronology and its application to young volcanic rocks. Geochim. Cosmochim. Acta 65, 2571-2587.

Schmitz, M.D., Schoene, B., 2007. Derivation of isotope ratios, errors, and error correlations for U-Pb geochronology using ^{205}Pb-^{235}U-(^{233}U)-

spiked isotope dilution thermal ionization mass spectrometric data. Geochem. Geophys. Geosyst. 8, Q08006.

Schoene, B., 2014. U–Th–Pb Geochronology, in: Holland, H.D., Turekian, K.K. (Eds.), Treatise on Geochemistry (Second Edition). Elsevier, Oxford, pp. 341-378.

Schoene, B., Bowring, S.A., 2006. U–Pb systematics of the McClure Mountain syenite: thermochronological constraints on the age of the $^{40}Ar/^{39}Ar$ standard MMhb. Contrib. Mineral. Petrol. 151, 615-630.

Simon, J.I., Renne, P.R., Mundil, R., 2008. Implications of pre-eruptive magmatic histories of zircons for U–Pb geochronology of silicic extrusions. Earth Planet. Sci. Lett. 266, 182-194.

Sliwinski, J.T., Bachmann, O., Dungan, M.A., Huber, C., Deering, C.D., Lipman, P.W., Martin, L.H.J., Liebske, C., 2017. Rapid pre-eruptive thermal rejuvenation in a large silicic magma body: the case of the Masonic Park Tuff, Southern Rocky Mountain volcanic field, CO, USA. Contrib. Mineral. Petrol. 172, 30.

Stelten, M.E., Cooper, K.M., Vazquez, J.A., Calvert, A.T., Glessner, J.J.G., 2015. Mechanisms and timescales of generating eruptible rhyolitic magmas at Yellowstone caldera from zircon and sanidine geochronology and geochemistry. J. Petrol. 56, 1607-1641.

Tiepolo, M., Oberti, R., Vannucci, R., 2002. Trace-element incorporation in titanite: constraints from experimentally determined solid/liquid partition coefficients. Chem. Geol. 191, 105-119.

Till, C.B., Vazquez, J.A., Boyce, J.W., 2015. Months between rejuvenation and volcanic eruption at Yellowstone caldera, Wyoming. Geology 43, 695-698.

Vazquez, J.A., Reid, M.R., 2004. Probing the accumulation history of the voluminous Toba magma. Science 305, 991-994.

Vervoort, J.D., Blichert-Toft, J., 1999. Evolution of the depleted mantle: Hf isotope evidence from juvenile rocks through time. Geochim. Cosmochim. Acta 63, 533-556.

von Quadt, A., Wotzlaw, J.F., Buret, Y., Large, S.J.E., Peytcheva, I., Trinquier, A., 2016. High-precision zircon U/Pb geochronology by ID-TIMS using new 10^{13} ohm resistors. J. Anal. At. Spectrom. 31, 658-665.

Watson, E.B., 1996. Dissolution, growth and survival of zircons during crustal fusion: Kinetic principles, geological models and implications for isotopic inheritance. Trans. R. Soc. Edinburgh Earth Sci. 87, 43-56.

Wolff, J.A., Ellis, B.S., Ramos, F.C., Starkel, W.A., Boroughs, S., Olin, P.H., Bachmann, O., 2015. Remelting of cumulates as a process for producing chemical zoning in silicic tuffs: A comparison of cool, wet and hot, dry rhyolitic magma systems. Lithos 236–237, 275-286.

Wotzlaw, J.F., Buret, Y., Large, S.J.E., Szymanowski, D., von Quadt, A., 2017. ID-TIMS U-Pb geochronology at the 0.1‰ level using 10^{13} Ω resistors and simultaneous U and $^{18}O/^{16}O$ isotope ratio determination for accurate UO_2 interference correction. J. Anal. At. Spectrom. 32, 579-586.

Wotzlaw, J.F., Schaltegger, U., Frick, D.A., Dungan, M.A., Gerdes, A., Günther, D., 2013. Tracking the evolution of large-volume silicic magma reservoirs from assembly to supereruption. Geology 41, 867-870.

Xirouchakis, D., Lindsley, D.H., Frost, B.R., 2001. Assemblages with titanite ($CaTiOSiO_4$), Ca-Mg-Fe olivine and pyroxenes, Fe-Mg-Ti oxides, and quartz: Part II. Application. Am. Mineral. 86, 254-264.

Chapter 3

Maturation and rejuvenation of a silicic magma reservoir: high-resolution chronology of the Kneeling Nun Tuff†

D. Szymanowski, B. S. Ellis, J. F. Wotzlaw, O. Bachmann

ABSTRACT

Knowledge of the conditions of magma storage prior to volcanic eruptions is key to their forecasting, yet little is known about how melt compositions, crystallinity and intensive parameters within individual magma reservoirs evolve over time. To address this, we studied the Kneeling Nun Tuff, a voluminous (> 900 km^3) deposit of an Eocene caldera-forming eruption from the Mogollon–Datil volcanic field in New Mexico, USA. Whole-rock, feldspar and amphibole compositions were combined with zircon trace-element geochemistry and precise isotope dilution–thermal ionisation mass spectrometry (ID–TIMS) U–Pb zircon crystallisation ages to arrive at a detailed, time-resolved record of chemical and physical changes within the voluminous, upper-crustal (~ 2.2 kbar) magma reservoir. Chemical compositions and zircon ages of the Kneeling Nun Tuff and co-magmatic clasts hosted within it reveal prolonged (> 1.5 million years) growth and maturation of the magma reservoir that was heterogeneous in terms of temperature, melt composition and crystallinity. This protracted storage at dominant crystallinity in excess of 50 % culminated in a period of ca. 100 ky of increase in recharge heat supply and related homogenisation, decrease in crystallinity to 40–50 %, and potential increase in average melt temperature, leading up to eruption at 35.305 ± 0.021 Ma. Sampling of co-magmatic lithic clasts derived from early-cooled domains of the magma reservoir show that the long, million year-scale maturation time is shared across all erupted domains of the magmatic system, irrespective of their final cooling history. This study provides key observations from a natural system against which thermal and mechanical models of upper-crustal magma reservoir construction can be validated.

†*This chapter is equivalent to a manuscript submitted to* Earth and Planetary Science Letters

3.1. Introduction

Explosive volcanic eruptions can have tremendous effects on both the Earth system and society, ranging from local-scale devastation to global perturbations of the climate system caused by release of volcanic gases (Self, 2006). Understanding how magma bodies feeding such eruptions work, as well as achieving the long-term goal of forecasting eruptions, crucially depends on the knowledge of the mode of magma storage (e.g. crystallinity, temperature, pressure, volatile content, all affecting its physical properties) and the timescale of the system's maturation prior to eruption. The physical state of a magma reservoir is key in the context of detecting such bodies by geophysical methods in the present day as well as reading their readiness to erupt (e.g. Flinders et al., 2018). In turn, the temporal aspect of magma residence feeds into a better understanding of magmatic fluxes, eruption frequencies and magnitudes (Costa, 2008). It is particularly important to know how magma parameters vary over time, e.g. whether the baseline (dormancy) magma storage conditions need to be drastically altered in a lead-up to an eruption, as proposed for silicic, high-crystallinity systems (Bachmann and Bergantz, 2003). Therefore, our understanding of upper-crustal magmatic processes would benefit from a detailed, absolute chronology of physical and chemical fluctuations in a fossil magma reservoir. Such a record has the potential to bring new insights about the magnitude, character and duration of key events in a magma chamber's life.

Ideally, such a chronology could be extracted from the most abundant, major mineral phases such as feldspar, pyroxene or quartz. However, the often-detailed stratigraphy of events preserved as compositional zoning in these phases carries little information that can be placed in absolute time. Given the relatively fast diffusion of most major and trace elements in these phases at magmatic temperatures (often utilised to constrain diffusion timescales; Costa et al., 2008), the compositions of the measured crystals will represent partial equilibration i.e. the conditions of crystallisation modified by any subsequent diffusion. Using an independently constrained temperature of storage of a crystal, diffusion modelling can then be used to constrain the maximum amount of time spent in a magma since the time of crystallisation (Cooper and Kent, 2014). This approach is capable of delivering important insights about the thermal history of individual crystals since a given (e.g. rim) crystallisation event, but currently cannot constrain the age of crystallisation itself except if combined with U-series ages of large mineral separates from young rocks (Cooper, 2015). As a consequence, so far we cannot build a reliable chronology of pre-eruptive events using the most abundant and sensitive, major mineral phases.

An alternative is to focus on zircon, a common accessory phase in silicic igneous rocks. Due to extremely slow diffusion of most trace elements (Cherniak and Watson, 2003), zircon crystals faithfully record melt composition and changes in intensive parameters while allowing them to be precisely placed in a temporal framework using the U–Pb chronometer. Similar approaches have been applied to young magmatic rocks mostly in the ^{230}Th–^{238}U disequilibrium range (Vazquez and Reid, 2004; Stelten et al., 2013; Bar-

boni et al., 2016; Tierney et al., 2016; Kaiser et al., 2017) but it has been shown that such solutions may be non-unique primarily due to poor precision of the individual zircon ages when compared to the expected duration of the events (Kent and Cooper, 2017). Additionally, this method is limited to magmatic systems younger than ca. 400,000 years while the majority of the most voluminous eruptions in the geological record and all known plutons are significantly older, requiring alternative analytical approaches. Zircon geochronology by isotope dilution–thermal ionisation mass spectrometry (ID-TIMS) has been shown to provide sufficient precision to resolve the timescales of magmatic processes on the scale of a single magma body (e.g. Coleman et al., 2004; Schaltegger et al., 2009). In particular, the combination of this technique with either bulk-grain or *in situ* zircon chemical and isotopic information can yield time–composition systematics constraining large-scale changes of magmatic conditions (Schoene et al., 2012; Wotzlaw et al., 2013; Rivera et al., 2014; Samperton et al., 2015).

Here we present a case study of appropriate age and a method of sufficient analytical precision (ID-TIMS, with typical single-crystal date uncertainties of <1‰) to obtain a detailed pre-eruptive chronology of a large magmatic system. We studied the Kneeling Nun Tuff, a voluminous (> 900 km^3) deposit of an Eocene super-eruption fed by a long-lived magmatic reservoir (Szymanowski et al., 2017 [*Chapter 2*]) with both traditional tools of petrology and detailed zircon petrochronology, allowing new insights into the maturation and rejuvenation of magmas feeding such large-volume caldera-forming eruptions.

3.2. Kneeling Nun Tuff

The Kneeling Nun Tuff (KNT) is a voluminous ignimbrite emplaced within the Mogollon–Datil volcanic field (MDVF) in western New Mexico, USA (Fig. 3.1; McIntosh et al., 1990, 1992; Chapin et al., 2004). The MDVF is part of a discontinuous belt of mid-Tertiary silicic volcanic fields extending from the southern Rocky Mountains in Colorado in the north (Lipman, 2007) to Sierra Madre Occidental in central Mexico in the south (McDowell and McIntosh, 2012; Fig. 3.1a). The Mid-Tertiary volcanic activity in this area is mostly characterised by an arc-like geochemical signature (high-K calc-alkaline series) related to the subduction of the Farallon plate beneath North America, however the large distance from the plate margin in present Colorado and New Mexico would require this subduction to be of low angle (Lipman et al., 1972; Coney and Reynolds, 1977). Alternatively, interpretations involving magma generation from the sub-continental lithospheric mantle previously modified by subduction have been proposed (Davis and Hawkesworth, 1993; Farmer et al., 2007).

MDVF activity followed a pattern similar to other Tertiary volcanic fields of SW North America, where early intermediate volcanism was followed by voluminous caldera-forming eruptions of silicic magma (cf. Lipman, 2007). In the MDVF, initial andesitic volcanism dominated between 40–36 Ma before episodic bimodal basaltic andesite–silicic

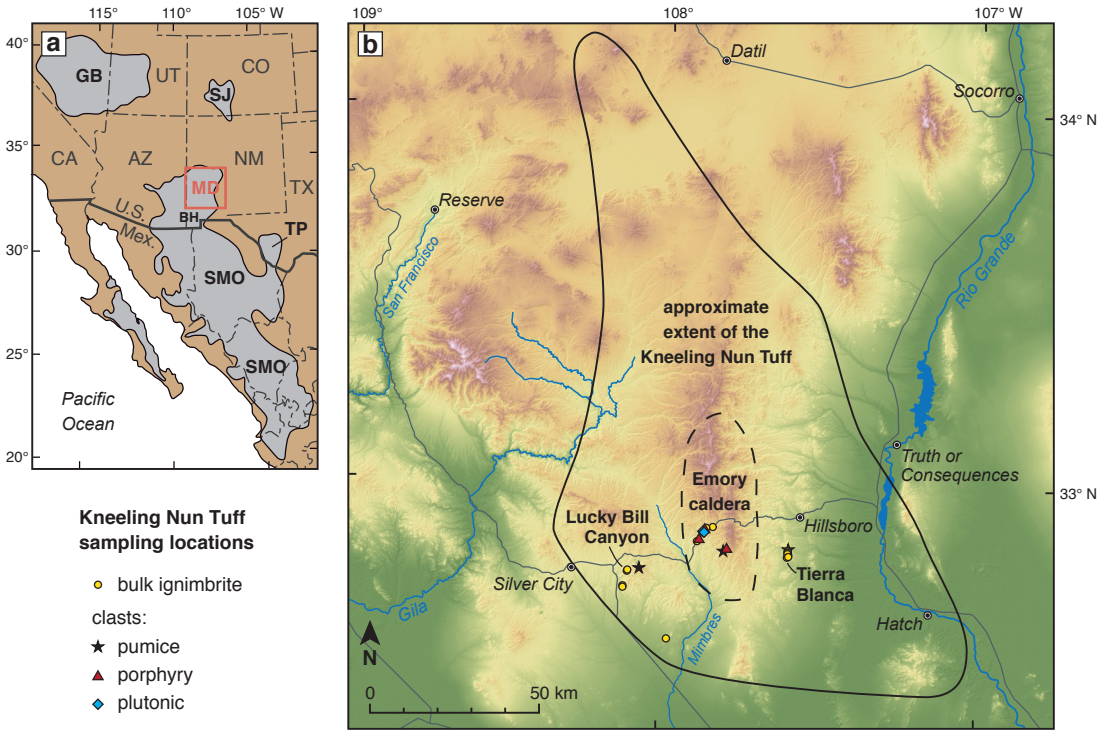

Figure 3.1. Location of the study area and Kneeling Nun Tuff sampling sites. (**a**) Map of the distribution of Tertiary volcanic rocks in SW North America (modified from McDowell and McIntosh, 2012); SJ–San Juan/Southern Rocky Mountain volcanic field; MD–Mogollon–Datil; BH–Boot Heel; TP–Trans-Pecos; SMO–Sierra Madre Occidental; GB–Great Basin. (**b**) Location of the Emory caldera, source of the Kneeling Nun Tuff, within the Mogollon–Datil volcanic field in western New Mexico, with the approximate extent of the KNT ignimbrite sheet proposed by McIntosh et al. (1992) based on paleomagnetic and $^{40}Ar/^{39}Ar$ data of distal samples. Three key areas were targeted for sampling: western outflow sheet at Lucky Bill Canyon, Hurley and inside Chino Mine; intracaldera KNT along NM-152 west of Emory Pass; eastern outflow sheet immediately south of Tierra Blanca valley.

activity became predominant between 36–24 Ma (Elston, 1984; McIntosh et al., 1990, 1992). The Kneeling Nun Tuff (Elston, 1957) was erupted from the Emory caldera (Elston et al., 1975) in the southern part of the Black Range in the centre of MDVF (Fig. 3.1b) at 35.36 ± 0.05 Ma (recalculated from McIntosh et al., 1990) and is considered the largest eruption of the first pulse of MDVF silicic volcanism (McIntosh et al., 1992).

The Kneeling Nun Tuff occurs both in thick intracaldera facies (500–1000 m; Kuellmer, 1954; Elston et al., 1975) and outflow facies (up to 150 m thick) extending at least 30 km beyond the caldera margins (Fig. 3.1b). This extent led to a minimum eruptive volume estimate of 900 km^3 (Elston et al., 1975) placing the KNT among the largest silicic eruptions in the geological record (Mason et al., 2004). The KNT outflow typically forms conspicuous, columnar-jointed red cliffs of welded ignimbrite with abundant pumice (Fig. 2a), which are often subdivided by local breaks into multiple 'cooling units' reflecting the complex nature of pyroclastic density currents and effects of variable topography

(e.g. Giles, 1965). The KNT typically overlies a thick sequence of broadly andesitic lavas and tuffs of the Rubio Peak formation, but locally a sequence of rhyolitic ignimbrites and air fall tuffs mapped as the Sugarlump Formation occurs beneath the KNT (Elston, 1957). Dated at 35.64 ± 0.12 Ma (recalculated from McIntosh et al., 1990), some of the Sugarlump tuffs may represent precursor eruptions from the same magmatic system that fed the KNT.

The Kneeling Nun Tuff is a crystal-rich (trachy)dacite to rhyolite carrying a mineral assemblage of quartz + sanidine + plagioclase + biotite + hornblende + rare clinopyroxene + magnetite + ilmenite + titanite + apatite + zircon. The reported crystal content is between 25 and 60 % (Giles, 1965). Accordingly, the KNT outflow sheets are locally zoned, with an upward increase in crystallinity, phenocryst size and the proportion of plagioclase and ferromagnesian phases accompanied by a decrease in the amount of quartz and alkali feldspar (Giles, 1968). Both outflow and intracaldera KNT facies contain abundant crystal-rich pumice, rare crystal-poor pumice and xenoliths of underlying Rubio Peak andesites, Palaeozoic basement rocks, and granites, porphyries and aplites of variable texture which may be partly contemporaneous and genetically related to KNT magma (Elston, 1989). Abundant cm-sized xenoliths are present throughout the ignimbrite but in some areas within the caldera they become larger (up to tens of metres) and form zones of 'megabreccia' that were previously interpreted as vent or collapse breccias (Kuellmer, 1954; Elston, 1989).

3.3. Samples

A total of 26 samples of different facies of the Kneeling Nun Tuff have been studied, comprising two main groups:

1) Samples of bulk KNT ignimbrite from the SW (Lucky Bill Canyon) and E (Tierra Blanca) outflow sheets as well as the caldera fill (Fig. 3.1), ranging from early- to late-erupted material. Detailed studies of the two outflow sections (Table 3.1; Fig. B2) are complemented by samples used only for bulk chemical analyses (Tables B1, B3).

2) A suite of magmatic clasts of presumed cogenetic character found within both intracaldera and outflow facies of the KNT ignimbrite (Table 3.1, Fig. 3.1). The samples were assigned to one of three groups: i) pumices, which have clear indications of ductile behaviour upon deposition (ubiquitous flattening, Fig. 3.2b), ii) porphyries, containing large phenocrysts in a formerly glassy matrix, but without clear evidence of syn-depositional deformation (Fig. 3.2d, e), and iii) plutonic lithics—angular fragments of holocrystalline, porphyritic to equigranular granites (Fig. 3.2c, f).

3.4. Analytical Methods

The samples were characterised by a combination of bulk chemical analyses, major element chemistry of main rock-forming mineral phases (feldspars, amphibole) and *in*

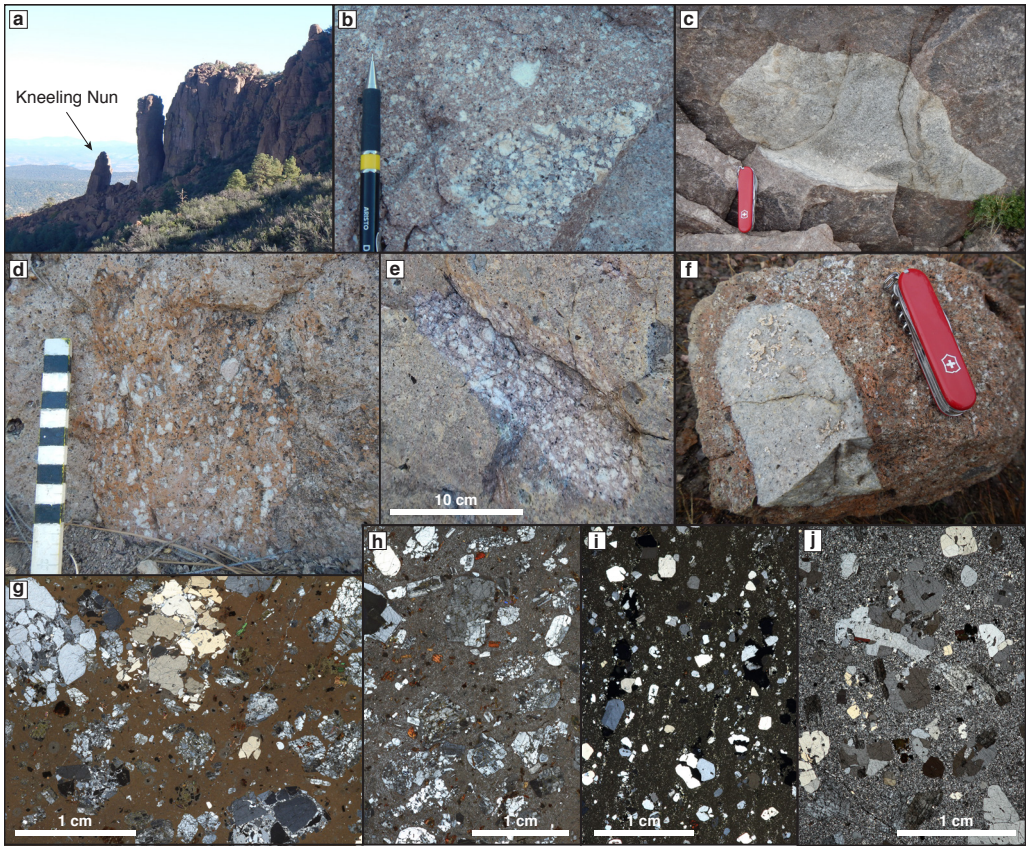

Figure 3.2. Field appearance and microscopic textures of studied lithologies. (**a**) The eruptive unit's namesake, the Kneeling Nun landmark near Santa Rita, NM. (**b–f**) Field appearance of studied clasts including crystal-rich pumice (**b**), plutonic clasts (**c,f**) and porphyries (**d,e**). The field scale in **d** is marked every 1 cm. (**g–j**) Cross-polarised light thin section images of representative samples of a porphyry (1509A, **g**), a crystal-rich pumice (1525-2, **h**), an evolved quartz-rich pumice (1434, **i**) and a holocrystalline granitic clast (1421, **j**).

situ trace element analyses of accessory zircon, followed by high-precision U–Pb isotope analyses of half-polished zircon crystals and crystal fragments.

Whole-rock compositions were determined following standard procedures by X-ray fluorescence (XRF) of fused glass beads with complementary laser ablation–inductively coupled plasma mass spectrometry (LA-ICPMS) analyses of trace elements. Feldspar and amphibole major elements were analysed in thin sections by electron probe microanalysis (EPMA). A subset of feldspar crystals was also analysed for trace elements by LA-ICPMS.

In order to obtain a time-resolved record of the KNT magma storage regime, a particular focus was placed upon studying the textures, compositions and crystallisation ages of zircon crystals separated from magmatic clasts found within the KNT ignimbrite. The analytical approach taken here is identical to that presented by Szymanowski et al. (2017, [*Chapter 2*]), which allows a direct comparison of zircons separated from a bulk

Table 3.1. Summary of crystallinities, compositions and intensive parameters calculated for key samples of Kneeling Nun Tuff and its magmatic clasts

Sample	crystallinity [%] [a]	SiO_2 [wt%] [b]	plagioclase An [c]	sanidine Or [c]	high-Ba rims	two-feldspar T [°C] [cd]	amphibole–plagioclase T [°C] [e]	amphibole P [kbar] [fg]
bulk ignimbrite								
1519	11		13–16	69–71		640–689		
1520	58	76.9	13–23	63–65		697–762		
1521	32	72.9	14–27	62–65		718–785		
1522	49	69.0	20–28	61–64	x	767–823	744–803	2.21±0.13
1402	46	69.5	21–28	61–66	x	729–822	746–801	2.21±0.09
1523	55	67.1	21–27	61–64	x	765–833		
1428	32	75.8	11–23	61–65		675–763		
1430	48	75.1	19–23	62–65	x	747–777		
1435	44	75.7	20–23	59–64	x	722–810		
pumices								
1434A	26	77.1	14–19	62–65		700–728		
1525-2	46	70.3	20–27	62–64	x	757–849	757–810	2.19±0.09
porphyrytic clasts								
1416A	56	73.8	18–24	64–68		729–780		
1509A	60	67.9	20–27	65–69	x	709–800	754–808	2.25±0.16
1511	62	69.0	22–26	66–68	x	727–797	761–800	2.22±0.09
plutonic clasts								
1421	100	75.6	15–22	61–63		695–740		
1510	100	77.0	16–19	61–62		684–750		

[a] crystallinity determined by point counting
[b] SiO_2 from XRF analyses, all major elements normalised to 100% on anhydrous basis
[c] excluding outliers as defined in Fig. B4
[d] equation 27b of Putirka (2008)
[e] thermometer B of Holland and Blundy (1994)
[f] Mutch et al. (2016)
[g] reported uncertainty (1σ) is a function of the scatter of Al_{tot} in amphibole; the uncertainty of the thermometer calibration is ca. 0.4 kbar

ignimbrite sample with those hosted by the various types of clasts. First, the zircons were mounted in epoxy, polished and imaged using cathodoluminescence (CL), which was followed by *in situ* analyses by LA-ICPMS for trace elements, and U–Pb isotopes to screen out inherited cores. Particular care was taken to ensure the accuracy of Ti analyses, which was made possible by the introduction of a Ti-rich zircon reference material GZ7 (Szymanowski et al., 2018 [*Chapter 4*]). Based on zircon compositions determined *in situ* and their CL textures, some crystals were selected for extraction from the epoxy mounts for dissolution and high-precision U–Pb analyses by chemical abrasion (CA)–isotope dilution–thermal ionisation mass spectrometry (ID-TIMS).

A complete description of all analytical procedures as well as tables with sample coordinates and all analytical data are provided as Supplementary Material (Appendix B).

3.5. Results

3.5.1. Whole-rock compositions and crystallinity

Bulk samples of KNT ignimbrite range in composition from (trachy-)dacite to rhyolite (67–77 wt% SiO_2, Fig. B1 and Table 3.1) with a crystallinity of 32–58% (11% in the basal fallout). Of the two outflow sheet sections studied in detail (Fig. 3.1), one (Lucky Bill Canyon; samples 1519–1523) displays clear, systematic variations from early-erupted, evolved (> 70 wt% SiO_2), less crystalline material to crystal-rich (46–55%), (trachy-)dacitic (67–69 wt% SiO_2), late-erupted material towards the top of the section (Fig. B2). The other section (Tierra Blanca; samples 1428–1435) does not show any substantial variability in compositions, but the earliest-erupted material is similarly crystal-poor. Key major and trace elements are characteristically correlated with SiO_2 (Fig. B1), and their trends are indicative of fractionation of feldspars, hornblende, Fe–Ti oxides, titanite, zircon and apatite, consistent with the observed mineral assemblage. The variability between early-erupted and late-erupted compositions can therefore be fully explained in terms of variable melt extraction and crystal accumulation within the upper-crustal magma reservoir. All sampled KNT-hosted clasts define the same compositional array (Fig. B1), with the bulk compositions corresponding to their mineral assemblage and crystallinity.

3.5.2. Feldspars

Feldspar occurs in the KNT as fragments of mostly euhedral plagioclase and sanidine that show little compositional variability within individual crystals, samples, between parts of the deposit, or within the juvenile/lithic clasts (Table 3.1; Fig. B3, B4). Plagioclase ranges mostly between An_{20} and An_{28} with rare cores of up to An_{51}, presumably inherited from deeper differentiation steps. An contents lower than ~20 are present exclusively in early-erupted material (samples 1519–1521, 1428), the crystal-poor pumice (1434) and the plutonic lithics (1421, 1510). Sanidine displays similarly little variability in major elements (Table 3.1; Fig. B3, B4); typical compositions are $Or_{61–66}$, with notable exceptions of elevated K in the porphyritic samples (1416A, 1509A, 1511; $Or_{64–69}$) and the basal fallout (1519, $Or_{69–71}$). Corresponding two-feldspar pairs reveal equilibrium temperatures (Putirka, 2008) of ~730–820 °C for most late-erupted material, crystal-rich pumice and porphyritic clasts, while the crystal-poor pumice, all early-erupted material and plutonic lithologies return lower temperatures ranging from ~760 °C down to 640 °C (in the basal fallout; Table 3.1, Fig. B2).

An additional feature of KNT sanidine is the common occurrence of one or more growth rims, present either as simple growth zones or surrounding a resorbed core, that are enriched in Ba (Fig. 3.3). The rims occur in most late-erupted parts of the ignimbrite as well as the porphyritic clasts, but are seemingly lacking in early-erupted and evolved-composition samples (Table 3.1). Their BaO contents are up to 2 wt% (Table B4); representative trace element data (Fig. 3.3) show that increased Ba is accompanied by enrichments in elements compatible in the bulk mineral assemblage such as Sr, Ti, P and REE and

depletions in the incompatible Rb. Additionally, Pb-isotopic compositions of these rims tend to be somewhat less radiogenic than the respective cores (Szymanowski et al., 2017 [*Chapter 2*]).

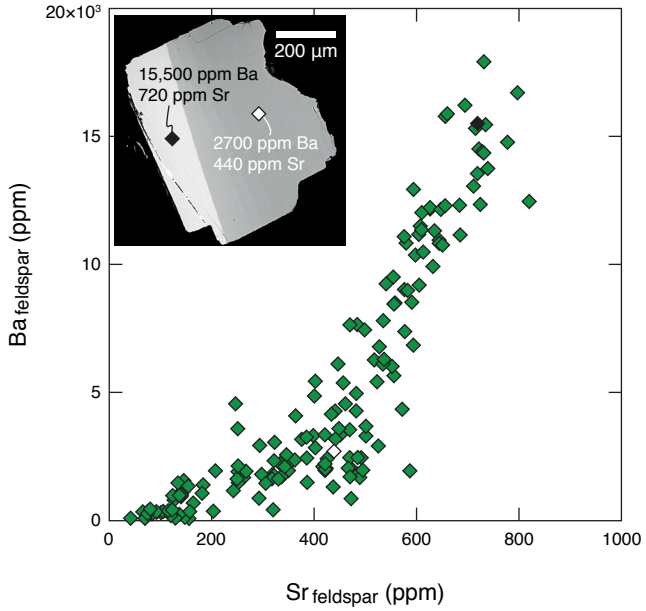

Figure 3.3. Trace element (Ba, Sr) compositions of representative KNT sanidine, illustrating the magnitude of enrichment in compatible elements. Inset: a backscattered electron image of a sanidine crystal typical for late-erupted material (Table 3.1) with a pronounced, high-Ba rim.

3.5.3. Amphibole

Except for rare ($n = 5$) cores of tschermakitic composition, all of the analysed amphibole crystals across bulk ignimbrite, pumice and porphyritic clast samples ($n = 115$) are Mg-hornblendes with a very restricted compositional range and no clear zoning within individual crystals (Table B5). The dominant, homogeneous population of hornblende satisfies criteria for equilibrium with the corresponding plagioclase at temperatures between 700–810 °C (Holland and Blundy, 1994), consistent with two-feldspar thermometry (Table 3.1) as well as the results of zircon- and titanite-based thermometry (Szymanowski et al., 2017 [*Chapter 2*]). Given the low-variance, near-solidus mineral assemblage of KNT, we applied the revised Al-in-hornblende geobarometer of Mutch et al. (2016), which yields a uniform pressure estimate of 2.22 ± 0.10 kbar (1σ) for the equilibrium hornblendes. The rare higher Al tschermakitic cores crystallised at pressures of 3–4 kbar and are interpreted as representing deeper stages of differentiation of magmas feeding the shallow KNT reservoir.

3.5.4. Zircon

3.5.4.1. Textures

Zircon crystals from the bulk KNT ignimbrite and the clasts hosted within it are typically euhedral and prismatic irrespectively of the sample lithology (Fig. 3.4). Nearly all grains display complex oscillatory (and rare sector) zoning testifying to their complex crystallisation histories. A subset of zircons, found in samples 1402, 1525-2 and 1509A, is characterised by large size (up to > 500 µm length), simple zonation patterns and conspicuously high CL intensities (Fig. 3.4) correlating to low rare earth element (REE) contents (section 3.5.4.3).

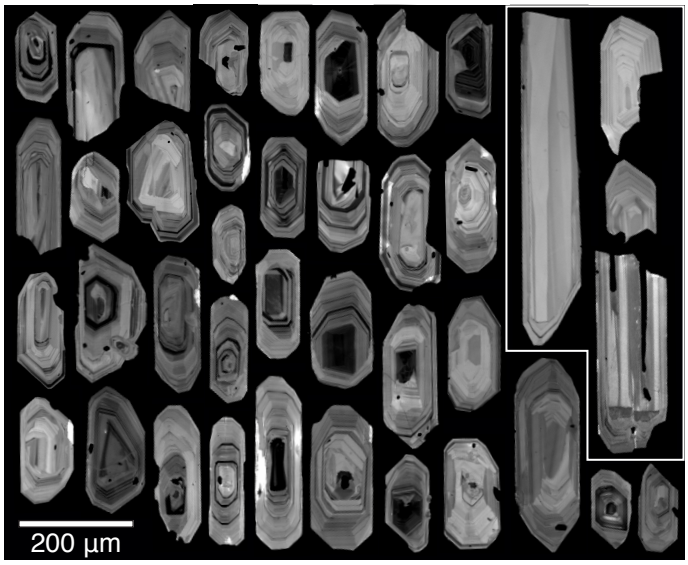

Figure 3.4. Cathodoluminescence (CL) images of representative Kneeling Nun Tuff zircon crystals from samples 1402, 1416, 1509A, 1511, and 1525-2. Note the frequent truncations and complex zonation patterns. The white frame highlights CL-bright, simply zoned, REE-depleted crystals with $^{206}Pb/^{238}U$ dates between 35.4 and 35.3 Ma.

3.5.4.2. High-precision U–Pb geochronology

ID-TIMS U–Pb dating was performed on single zircons extracted from three kinds of magmatic clasts; pumices (2 samples), porphyries (3 samples), and plutonic lithics (2 samples; Fig. 3.5). The targeted crystals were pre-screened based on CL imaging and *in situ* chemical analyses and except for one dated zircon (1416A z21) did not show any indication of inheritance. With the exception of one of the plutonic clasts (1510-1) which is distinctly older than the remaining samples, the ranges of individual zircon dates from each clast overlap to a large degree both between samples and with the bulk outflow ignimbrite zircons analysed previously by Szymanowski et al. (2017 [*Chapter 2*]). This supports field relationships between the clasts and the hosting Kneeling Nun Tuff

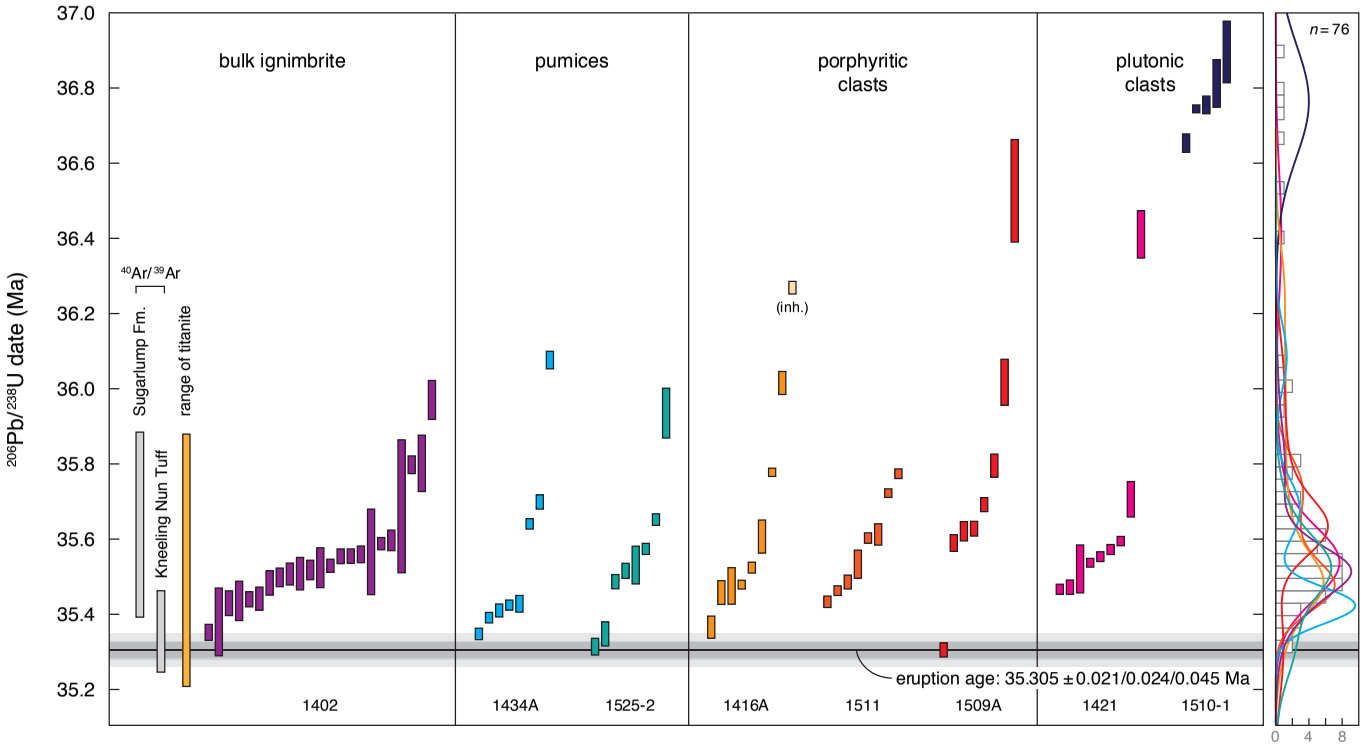

Figure 3.5. Texturally resolved geochronology of the Kneeling Nun magmatic system. Coloured bars represent ID-TIMS $^{206}Pb/^{238}U$ dates of individual zircon crystals together with their 2σ uncertainty. Bulk-ignimbrite zircon and titanite data for sample 1402 is reproduced from Szymanowski et al. (2017 [*Chapter 2*]). $^{40}Ar/^{39}Ar$ sanidine dates for KNT and uppermost Sugarlump tuffs (McIntosh et al., 1990) were recalculated to the calibration of Kuiper et al. (2008). The preferred eruption age is equivalent to the single youngest zircon crystal from sample 1509A and displayed with three uncertainty envelopes: internal only (including initial Th–U disequilibrium correction)/with tracer calibration/with tracer and ^{238}U decay constant. Side panel: colour-coded kernel density plots illustrating the zircon age distribution of individual samples, overlaid on a histogram of all zircon dates in this study.

and confirms that all overlapping samples, and likely also the granitic clast 1510-1, are sourced from the same upper-crustal magmatic system. The re-sampling of this system additionally confirms its longevity, with the zircon from clast samples spanning ranges of U–Pb dates from 341 ± 20 ky to as much as 1.22 ± 0.14 My comparable to 618 ± 56 ky obtained for the bulk ignimbrite.

The Kneeling Nun Tuff eruption age can now be defined as either the Th-corrected $^{206}Pb/^{238}U$ date of the single youngest zircon (35.305 ± 0.021/0.024/0.045 Ma) or the weighted mean of two overlapping, youngest Th-corrected zircon $^{206}Pb/^{238}U$ dates yielding 35.309 ± 0.016/0.019/0.043 Ma (2σ uncertainty given as internal only/with tracer calibration/with ^{238}U decay constant). The two estimates are indistinguishable and both are fully consistent with the existing $^{40}Ar/^{39}Ar$ sanidine dates of the KNT (McIntosh et al., 1990) recalculated to a modern standard and decay constant calibration (Fig. 3.5). The $^{40}Ar/^{39}Ar$ age of the uppermost Sugarlump tuffs (McIntosh et al., 1990) overlaps with most of the zircon crystallisation interval, suggesting a genetic relationship between at least some of the Sugarlump eruptions and the KNT.

Individual dates of zircons from both pumice samples (the evolved, high-Si 1434A, and the low-Si 1525-2) range from ones close to, or overlapping, eruption age at 35.309 ± 0.021 Ma and up to a maximum of 36.077 ± 0.023 Ma (Fig. 3.5). While the number of analysed zircons is smaller ($n = 8$) and consequently the sampled populations are less representative than the large bulk ignimbrite dataset, the pumices preserve an indistinguishable age distribution, suggesting that they sample a comparable age domain. In contrast to the pumices, the textures of the porphyries imply rapid cooling of these magma volumes some time before eruption. This appears true for all three porphyry samples as they record the same time of peak zircon crystallisation and apparent pre-eruptive gaps in zircon distributions of 61 ± 35, 128 ± 24 and 285 ± 29 ky. However, one exception is that sample 1509A contains one young zircon with a date overlapping (or indeed defining) the eruption age. The plutonic samples, consistently with textures requiring slow cooling pre-dating the eruption, only contain zircons with crystallisation ages significantly older than the eruption age. The granitic clast 1421, similarly to porphyry samples, records zircon crystallisation coeval with that found in pumices and in bulk ignimbrite, but with a pre-eruptive gap of 162 ± 23 ky. Clast 1510-1 represents an early period of intrusion with zircon crystallisation ages from 36.896 ± 0.082 to 36.653 ± 0.025 Ma. These granitic clasts show that during most of the time of magma reservoir assembly, portions of the reservoir were fully solid, forming 'cool' wall-rock around the active, eruptible domains.

3.5.4.3. Trace elements

Trace elements in KNT zircons (Fig. 3.6, Table B6) show large variability consistent with the complex CL textures and the complexity expected from sampling domains of the magmatic system with different thermal histories. The zircon compositions testify to the key control exerted by co-crystallising titanite and, to a lesser degree, hornblende

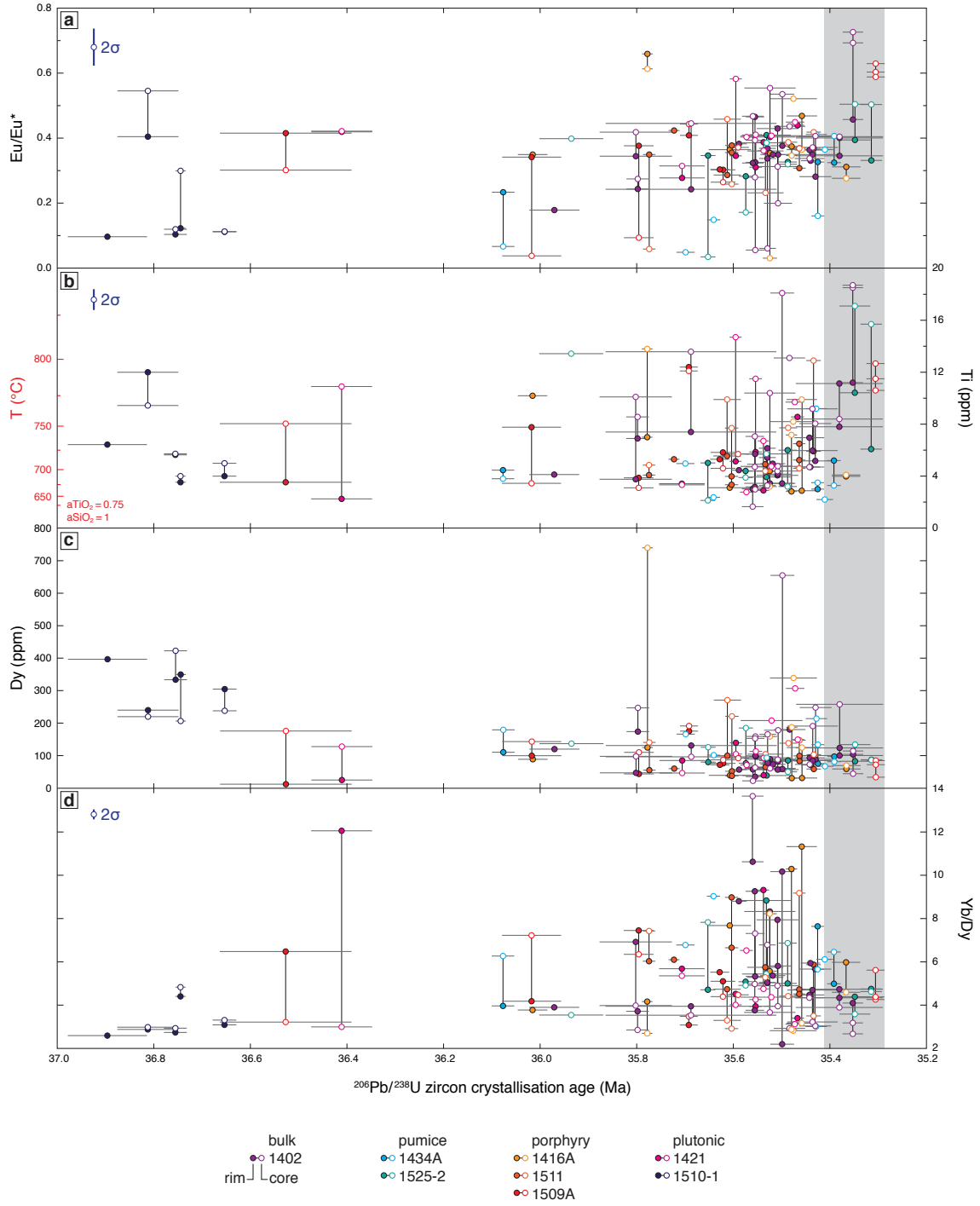

Figure 3.6. Variability of selected trace elements in Kneeling Nun Tuff zircon through time. Each point represents one *in situ* LA-ICPMS analysis prior to ID-TIMS U–Pb dating of the bulk crystal; in cases where multiple spot analyses of a crystal are available, they are assigned the same crystallisation age and connected with a vertical line. Note that the real crystallisation ages of the sampled spots may deviate from the assigned ones as bulk U–Pb dates are likely to be biased towards ages of rims and high-U zones. The grey shaded area highlights the time of gradual compositional changes in the system. Typical uncertainties are based on counting statistics for element ratios (Yb/Dy,

over REE budgets, which can be shown with simple geochemical models (Szymanowski et al., 2017 [*Chapter 2*]) for both REE contents and heavy/middle REE ratios (e.g. Yb/Dy). Strong correlations exist between titanite indicators (e.g. MREE or Th/U) and the temperature-dependent Ti contents (Ferry and Watson, 2007). This is particularly the case for low-Ti zircons, suggesting relatively low-T titanite saturation. Zr-in-titanite thermometry (Szymanowski et al., 2017 [*Chapter 2*]), recalculated to the amphibole pressure of 2.2 kbar, places titanite saturation for KNT at around 734 °C.

Combining trace elements with bulk-grain crystallisation ages (Fig. 3.6) reveals a complex history of zircon crystallisation within the KNT magma reservoir. While individual samples do not provide sufficient data points to evaluate any temporal trends, all data taken together reveal important reservoir-scale systematics. For most of the reservoir lifetime, the zircons are characterised by significant compositional scatter with dominant low-T, evolved compositions (e.g. Eu/Eu* of 0.2–0.5, Ti: 3-10 ppm, Dy < 200 ppm) punctuated by excursions suggesting both higher temperature (high Ti), less-evolved melts (e.g. high Eu/Eu*, Dy, low Yb/Dy) and lower temperature, more-evolved compositions (low Ti, Eu/Eu*, Dy, high Yb/Dy). However, crystals with bulk U–Pb ages between ~35.4 and eruption age at 35.305 Ma exhibit a striking reservoir-wide compositional focussing trend towards increased Eu/Eu* (0.3–0.7), Ti (4–19 ppm) and variably decreased REE (e.g. Dy < 150 ppm, Yb < 600 ppm), Yb/Dy (< 6) (Fig. 3.6). The sense of measured zonation within individual crystals is highly variable, with inner zones ('cores' in Fig. 3.6, B6) generally showing more scatter than rim compositions; however, both cores and rims separately define the described trend in time. The four youngest zircon crystals of this composition are also distinct texturally (Fig. 3.4). The observation of this compositional trend across five separate samples strongly suggests a critical change in magmatic storage conditions that affected large portions of the magma reservoir.

3.6. Discussion

3.6.1. Magmatic architecture and storage conditions determined from major mineral phases

Major mineral phases in the Kneeling Nun Tuff constrain the dominant magma storage conditions to a pressure of ~2.2 kbar (ca. 7–9 km depth) and temperatures between ~670 °C and 820 °C (Table 3.1), consistent with its near-solidus mineral assemblage. Pre-eruptive crystallinity of the dominant volume of erupted magma (as documented in the late-erupted samples) appears to have been on the order of 40–50 %, but locally or episodically reached values in excess of 60 % (Table 3.1). Such high crystallinity may

Figure 3.6. continued
Eu/Eu*) or counting statistics and the composition of primary reference materials for Ti, Dy. For Dy the error bar is smaller than symbol size. Ti was either analysed relative to reference zircon GZ7 (Szymanowski et al., 2018 [*Chapter 4*]) for clast-hosted zircon or recalculated to match the same calibration (via zircon 91500) for previously analysed zircon from bulk sample 1402. Ti-in-zircon temperature estimates use the model of Ferry and Watson (2007).

imply rheological lock-up in the form of a rigid crystal mush, which facilitates the long-term survival of the magma body but requires a process eventually reducing the crystal content for most of the reservoir volume to erupt (Marsh, 1981; Bachmann et al., 2002; Bachmann and Bergantz, 2003). Locally melts would get extracted from the mush zone, creating pools of more evolved, crystal-poor material, represented by crystal-poor pumice (1434), the basal fallout (1519) and, as variable mixtures with crystal-rich material, in early-erupted magma (Table 3.1).

Amphibole and feldspar compositions, as well as those of bulk rock (Fig. B1), reveal large-scale compositional homogeneity of the KNT magma reservoir. Most of the variability in whole-rock compositions is attributable to variable mineral proportions and crystallinity, while all deviations in feldspar compositions and temperatures (Table 3.1) result from either 1) local melt extraction or 2) variable cooling of different domains sampled by clasts. In particular, the lowest An contents of plagioclase are associated with extracted melts either in the evolved pumice (1434) or in all early-erupted material, as well as the slowly-cooled plutonic clasts (Fig. B4). Similarly, all deviations to higher orthoclase contents of K-feldspars occur either in extracted melts (1519) or in porphyry samples which presumably did not readjust their compositions to predominant conditions due to premature solidification.

The occurrence of high-Ba rims in sanidine (Fig. 3.3) requires the episodic presence of melts enriched, with respect to background values of melt in equilibrium with most of sanidine volume, in Ba and other bulk-compatible elements (section 3.5.2). Such compositions can generally be expected as a result of either 1) recharge of the system with less evolved melts, or 2) melting of the resident mush in response to a heat and volatile addition, with the melting phase assemblage dictating the elemental enrichments (Wolff et al., 2015; Forni et al., 2016). In the KNT, the enrichments would require the melting of cumulate sanidine + plagioclase (Ba, Sr), titanite (Ti, REE) and apatite (P), most likely accompanied by abundant quartz and biotite as low-temperature phases. The wide range of published partition coefficients for trace elements in sanidine are permissive of very large enrichments even at equilibrium, precluding a unique interpretation; additionally, it is doubtful that such cumulate-derived crystallisation reflects an equilibrium process (e.g. Arzilli et al., 2018). In reality the generation of any cumulate melt is likely caused by an influx of hotter recharge magma, so the two processes should be expected to always act together. In the Kneeling Nun magma reservoir, the presence of ubiquitous, often multi-stage high-Ba rims in the crystal-rich, late-erupted material as well as in the porphyry samples (which presumably cooled down before eruption) suggest that mafic recharge and cumulate melting are common and repeated processes. This is in line with the long-lived nature of the KNT system, which requires a persistent influx of heat delivered through recharge magma to remain thermally buffered over timescales of several hundred thousand years (Szymanowski et al., 2017 [*Chapter 2*]).

While the major mineral phases provide a relatively simple view of magmatic storage in the KNT reservoir, it is crucial to emphasise which 'time slice' of the prolonged, million-year history of the magmatic system they represent. For feldspar and amphibole (or any other magmatic mineral), the compositions of erupted crystals should represent conditions at time of crystallisation modified by any subsequent diffusion. In these minerals, the retention of most major and trace elements at magmatic conditions is relatively limited, and depends primarily on their post-crystallisation storage history (Cooper and Kent, 2014). If storage temperatures can be estimated independently, one can model the storage time of individual crystals since a given (e.g. high-Ba rim) crystallisation event, but this result remains relative to the assumptions made. Therefore, we prefer to focus on zircon petrochronology to provide a faithful, time-resolved record of magma reservoir evolution.

3.6.2. Time-resolved record of magmatic storage and rejuvenation

Zircon trace element compositions can be interpreted in terms of changes in both melt composition and intensive parameters such as temperature (Melnik and Bindeman, 2018). Given the comparable timescales of zircon growth and diffusive equilibration (Watson, 1996; Cherniak and Watson, 2003), except for sector zones, zircon compositions are expected to faithfully record the chemical and physical environment at time of growth. Consequently, with a basic understanding of the main factors controlling zircon compositions, both the temporal and the compositional information in zircon may be exploited to construct a chronology of major pre-eruptive events in a magma chamber (e.g. Wotzlaw et al., 2013; Barboni et al., 2016). In many cases, particularly for young rocks, the analytical age resolution may not be adequate to resolve events with sufficient certainty (Kent and Cooper, 2017). However, in the case presented here for the Kneeling Nun Tuff, the precision afforded by applying ID-TIMS dating provides a chance to describe such systematics with a high degree of confidence, at least in the time dimension (2σ uncertainties on individual dates 11–177 ka).

Figure 3.6 illustrates in a simplified way (where multiple zones of the same crystal are assigned identical age) that in the KNT, and by extension in other long-lived magmatic systems that experience continuous recharge, multiple conditions/melt compositions can coexist at the same time. In other words, the degree of magmatic evolution, e.g. along a liquid line of descent, does not equate to time (except for simply cooling magmatic systems, e.g. Samperton et al., 2015). Instead, the trace element compositions of KNT zircon show that within a large magma reservoir, environments of varying temperature, crystallinity, or mineral proportions (e.g. samples of cumulate character vs. extracted melts) can co-exist and can ultimately be sampled by the same eruption (Fig. 3.6, B5, B6). In detail, every *in situ* compositional data point averages compositions of multiple zones in the complex KNT zircons (Fig. 3.4) and the individual core–rim trajectories are not systematic, while the signatures themselves can be strongly affected by phases co-crystallising in the immediate vicinity of the zircon (Melnik and Bindeman, 2018).

However, a large dataset of such variably biased zircon compositions allows us to draw first-order conclusions about the character, magnitude, and duration of magma reservoir-wide processes.

The key trace element trajectories depicted in Fig. 3.6 all show large variability in zircon compositions for most of the KNT system's lifetime, ranging from ones corresponding to low-crystallinity, unevolved melts to some indicating highly fractionated, crystalline environments (mostly innermost cores, Fig. B6). However, at ~35.4 Ma, or ~100 ky prior to eruption, the system appears to undergo a significant change exhibited in more focussed, or systematically offset, compositions. The negative Eu anomaly (Eu/Eu*), primarily controlled by crystallisation/melting of feldspar, records a notable shallowing towards the eruption (Fig. 3.6a). At the same time, Dy and Yb/Dy, controlled by titanite crystallisation (i.e. in a titanite-saturated system, its crystallinity), record a shift towards titanite undersaturation (Fig. 3.6c,d). The increase in the temperature-dependent Ti towards the eruption may reflect an increase in melt temperature, assuming activities of Ti and Si in the melt remain constant (Ferry and Watson, 2007). Alternatively, influx of less evolved melts and the associated (non-modal?) melting of minerals may alter both the Ti and Si activity in a way that is difficult to predict or model, which could result in both completely masking (higher a_{TiO2} or lower a_{SiO2}) and strengthening (lower a_{TiO2}) the potential signal of temperature increase.

To understand the exact nature of the melts represented by the measured zircon compositions, we modelled melts in equilibrium with all KNT zircons using a temperature-dependent parametrisation of zircon–melt element partitioning that uses Ti-in-zircon as a temperature proxy (Claiborne et al., 2018). This approximation, while potentially strongly biased by the accuracy of Ti quantification, proves useful in simulating the first-order control of temperature on partitioning (Fig. 3.7). Assuming that differences in Ti represent real temperature variations, we inverted zircon trace element compositions (Fig. 3.7a) to their corresponding melts (Fig. 3.7b). This resulted in melt compositions that are broadly consistent with the KNT bulk rock trend, and display a remarkable transition between apparently hot, titanite-undersaturated melts (low Yb/Dy, high Dy in Fig. 3.7b) and relatively cold, near-solidus, titanite-saturated melts (high Yb/Dy, low Dy). In the KNT, where REEs are almost exclusively controlled by titanite (Szymanowski et al., 2017 [*Chapter 2*]), trends towards melts with high Yb/Dy can be explained only by co-crystallising titanite, while the reverse (to low Yb/Dy, high Dy) can be accomplished by both mixing with less evolved melts and melting of pre-existing titanite. At the same time, changes in Eu/Eu* (Fig. 3.6a) result in an identical interpretation for feldspar crystallisation and melting. As a consequence, zircon compositions alone are unable to discriminate between an influx of recharge melts and the melting of cumulates caused by the heat delivered by the same process (Wolff et al., 2015).

Plotting the resulting melt compositions against time (Fig. 3.8) creates a record of highly diverse conditions for most of the magma reservoir's lifetime, varying between hot,

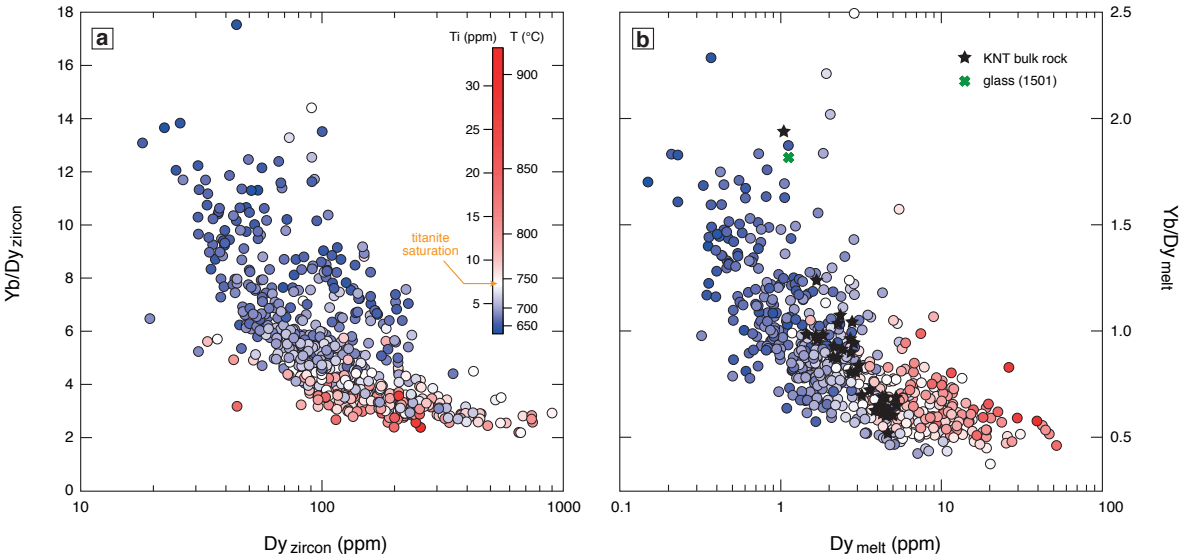

Figure 3.7. Trace elements in zircon and their corresponding melts, colour-coded for Ti content in zircon. (**a**) Results of LA-ICPMS measurements of KNT zircon across all dated samples. (**b**) Melts in equilibrium with individual measured zircon compositions, calculated using power-law fits between Ti and zircon–melt partition coefficients (Claiborne et al., 2018). Titanite saturation temperature is the average Zr-in-titanite temperature of Szymanowski et al. (2017, [*Chapter 2*]) adjusted for pressure of 2.2 kbar.

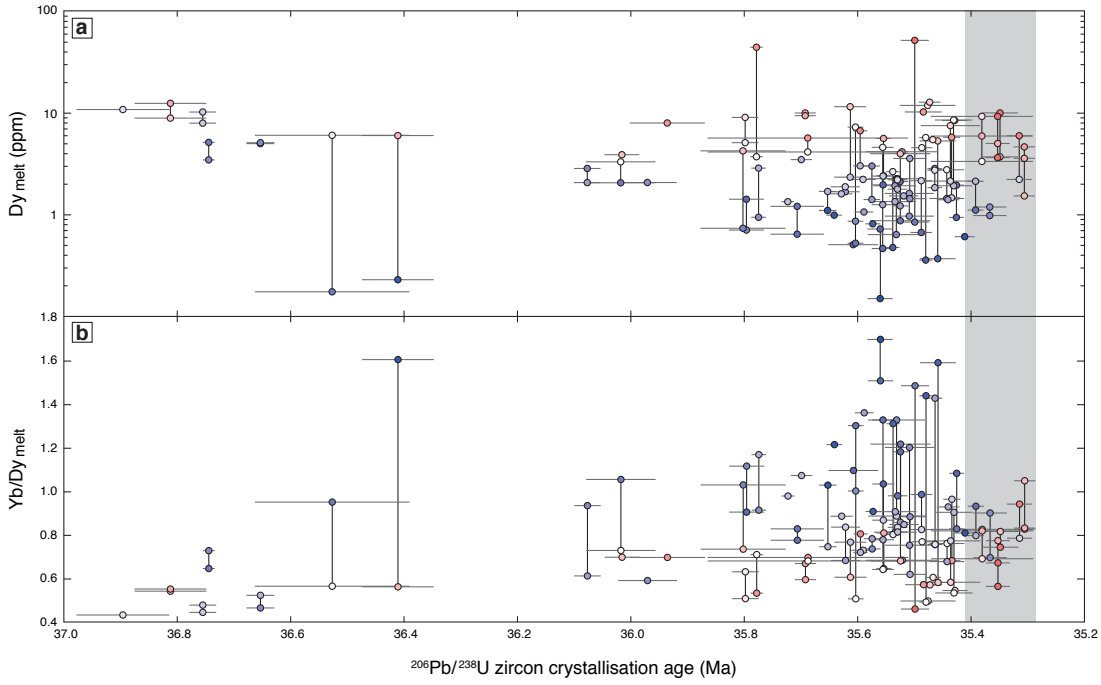

Figure 3.8. Composition of reconstructed Kneeling Nun Tuff melts through time. Each point corresponds to a datum in Fig. 6. The time coordinate is identical to that of coexisting whole-zircon crystallisation age, while the composition is recalculated from the respective *in situ* zircon analysis using the model of Claiborne et al. (2018) as in Fig. 3.7.

titanite-undersaturated and, more commonly, near-solidus, titanite-saturated (< 734 °C) melts. This is consistent with previous results for KNT implying magma storage dominantly within the titanite crystallisation window (Szymanowski et al., 2017 [*Chapter 2*]) as well as thermal models (Gelman et al., 2013; Karakas et al., 2017) suggesting that maintaining upper-crustal silicic magma reservoirs for timescales of 10^5–10^6 years is favoured for high-crystallinity, near-solidus bodies that receive their heat through episodic magma recharge (here likely represented by 'hot', high-REE, high-Eu/Eu* zircons). We interpret the last ~100 ky to represent a period of increased recharge heat and mass supply which resulted in decrease in crystallinity, increase in temperature and gradual homogenisation of the magma reservoir in the lead-up to eruption (Fig. 3.9). Similar mechanisms have been invoked as means of rejuvenating evolved magmatic systems from their baseline, high-crystallinity state to an intermediate-crystallinity state that is rheologically mobile and eruptible, with modelled timescales between months to years (Burgisser and Bergantz, 2011) to 10^3–10^5 years (Bachmann and Bergantz, 2003; Huber et al., 2012). Geological studies have inferred such timescales to be e.g. ~200 ky for the 5000 km^3 Fish Canyon Tuff (Wotzlaw et al., 2013), ~10 ky for the 1000 km^3 Lava Creek Tuff (Matthews et al., 2015), ~15–40 ky for Soufrière, St. Lucia (Barboni et al., 2016). Here we show that for the > 900 km^3 Kneeling Nun Tuff, rejuvenation took on the order of 100 ky, adding to the growing database of such well-described eruptive units.

3.6.3. Coeval environments of variable cooling history

Studying clasts erupted together with the KNT ignimbrite allows us to evaluate not only the homogeneity of the system in major and trace element compositions (section 3.6.1) but also its temporal evolution across multiple 'facies' of the magmatic source. The fact that there is no clear distinction in the mineral compositions between these clasts (Fig. B4), as well as the great overlap in zircon dates (Fig. 3.5) and trace elements (Fig. 3.6), show that all these lithologies are sampled from the same, voluminous, long-lived (> 1 My) upper-crustal magma reservoir. However, the textures of the clasts (Fig. 3.2) suggest different scenarios for their final cooling and solidification, ranging from slow cooling for the holocrystalline, plutonic samples, to rapid but sub-surface freezing of the porphyritic clasts and syn-eruptive quenching of the pumices. The textural information is aided by zircon age distributions (Fig. 3.5), creating a fingerprint of the thermal history of individual magma volumes in the context of the entire magma reservoir (Fig. 3.9). The plutonic clasts likely represent peripheral volumes of the system; we speculate that at some point of its maturation, insufficient heat is supplied from the recharging magma to keep the particular magma portion above solidus, resulting in slow cooling and formation of the plutonic rind (effectively the wall rock) of the system. Porphyritic clasts require rapid freezing, which may be a result of decompression, e.g. related to previous eruptions (such as the Sugarlump tuffs), or ascent and emplacement in much cooler surroundings. Long apparent hiatuses in zircon crystallisation (such as 280 ky in the porphyritic clast 1509A; Fig. 3.5) suggest that locally volumes of magma may become zircon under- or oversaturated, or, less likely, cool below solidus for extended periods of time.

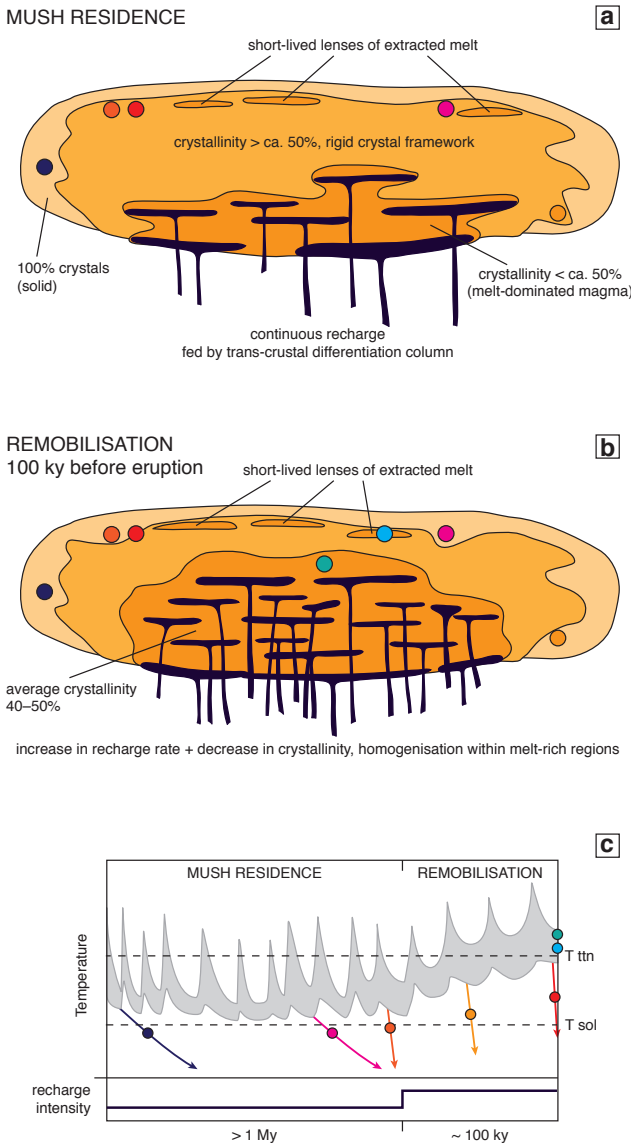

Figure 3.9. Conceptual model of the storage and remobilisation of the Kneeling Nun magmatic system. (**a–b**) Two key stages of evolution of the magma reservoir prior to eruption: long-term mush residence (**a**) and pre-eruptive remobilisation (**b**). Coloured circles correspond to locations of the magmatic clast samples. For most of the reservoir's lifetime (**a**), magma is stored at high but variable crystallinity depending on proximity to the recharge heat source. Most of the magma volume is stored as immobile, rigid crystal framework ('mush', > ca. 50 % crystals) below titanite saturation (T_{ttn} ~ 730 °C). Locally, pools of evolved melt may form by extraction from the crystal framework. Where the amount of supplied heat is insufficient, magma solidifies to form the plutonic rind of the system. (**b**) In the last ca. 100 ky prior to eruption, an increase in recharge rate results in a gradual, large-scale decrease in crystallinity (to about 40–50 %, i.e. eruptible state), which may facilitate homogenisation by overturn. The ultimately erupted material (and its crystals) is a mixture of different environments within the magma reservoir, volumetrically dominated by the mush zone, with a minor proportion of extracted melts. (**c**) A schematic depiction of the temperature evolution of the KNT reservoir, with temperature cycling as a function of recharge. Individual clasts sample the same maturation history but differ in the time and mode of final cooling, from early solidification of some porphyry and plutonic lithologies to quenching upon eruption for the pumices.

Finally, pumices represent batches of magma that were mobile at eruption (Fig. 3.9). Irrespective of the complexity of individual cooling paths of the clasts, the reproducibility of the age spectrum of the bulk ignimbrite sample in the clast-hosted zircons (Fig. 3.5) suggests that every sample may capture essentially the entire life of the KNT magmatic system from early intrusions to eruption.

3.6.4. Sampling eruption-age zircons

Accurately dating past eruptions is an invaluable component of many studies requiring independent information about the timing of events in the geological past. Indeed, ID-TIMS U–Pb dating of zircon from distal volcanic ash beds intercalated with sedimentary sequences has played a key role in the establishment of the absolute time framework of the geologic timescale (Gradstein et al., 2012). A key issue in deriving an eruption age from a population of volcanic zircon deposited in an ash bed is the likelihood of sampling age domains equivalent to the time of eruption (see e.g. Schmitz and Davydov, 2011; Schoene et al., 2015 for interpretation strategies). The large ($n = 76$) dataset of ID-TIMS dates generated here from a proximal deposit of a super-eruption (Fig. 3.5) may be a suitable proxy for the true distribution of zircon crystallisation ages in a magma body (as sampled by bulk U–Pb dating). It is important to note that the bulk-grain dates may not represent the true distribution of the volume of zircon crystallised in the system, as besides volume, the dates are biased primarily by U concentrations that vary between the zircon's growth zones (e.g. typically U-rich, CL-dark zones in Fig. 3.4). However, every set of ID-TIMS dates will be biased in a similar way, which justifies the comparison.

As is apparent from the temporal distribution of zircon crystallisation in the KNT magma (illustrated in Fig. 3.5), in this case randomly sampling the true eruption-age zircons (if at all present) may prove extremely challenging. Assuming here that the eruption occurred at time defined by either the Th-corrected $^{206}Pb/^{238}U$ date of the youngest (35.305 ± 0.021 Ma) or the weighted mean of the two youngest overlapping dates (35.309 ± 0.016 Ma), it is clear that at the current level of precision, the likelihood of randomly sampling this age domain is very small (2 out of 76 dates), in particular for typical ash bed datasets with $n \sim 6$ to 15. This is identical whether we consider all 76 zircon grains, or only ones from truly 'juvenile' samples of bulk ignimbrite and pumices ($n = 39$). A similar pattern emerges from other large ID-TIMS datasets, at least for calc-alkaline magmatic systems such as the Fish Canyon Tuff (Wotzlaw et al., 2013). In contrast, in intraplate settings, zircon age distributions appear to be very narrow, which significantly increases the chances of sampling the eruption age (Rivera et al., 2014; Wotzlaw et al., 2014). In the KNT, the measured distribution (Fig. 3.5) has the main peak of zircon crystallisation at 100–300 ky before the eruption, with relatively little crystallisation in the last 100 ky, during the inferred rejuvenation of the system. If pre-eruptive reheating is the reason for decreased zircon crystallisation in that period, then by extension such processes, increasingly observed in a range of volcanic systems

(e.g. Bachmann et al., 2002; Wark et al., 2007; Molloy et al., 2008; Huber et al., 2012), should commonly decrease zircon yield before eruptions.

Our data shows that KNT zircon crystals younger than ~35.4 Ma, i.e. ones interpreted to represent the rejuvenation interval, are distinct texturally (large, CL-bright, simple zoning; Fig. 3.4) and compositionally (low REE, high Eu/Eu*, Ti; Fig. 3.6). We propose that such systematics might be widespread in calc-alkaline magma chambers, including systems where the rejuvenation interval is significantly shorter or even unresolvable with geochronology. Therefore, careful textural and compositional characterisation of ash bed zircon, either *in situ* or with bulk measurements (Schoene et al., 2010; Schoene et al., 2015; Wotzlaw et al., 2017), might aid the process of zircon preselection and the interpretation of zircon age distributions for the purpose of timescale calibration. Compositional information of zircons from out-of-context or altered airfall ash beds (bentonites, tonsteins etc.) will additionally help to establish the tectonic affinity of the source of volcanism, which should further improve the age interpretations.

3.7. Conclusions

Zircon age and trace element data presented here for the Kneeling Nun magmatic system provide a detailed record of magma chamber maturation and rejuvenation in the build-up to one of the largest eruptions in the geological record. This unique, large dataset for a single eruption reveals long and complex storage of magma in the form of a high crystallinity mush, dominantly at near-solidus temperatures (< ca. 730 °C), but large internal temperature and crystallinity variations as a function of location with respect to the heat source. We show that the prolonged storage and maturation of KNT magmas of at least 1.5 million years culminated in a period of ~ 100 ky of increase in heat supply and related homogenisation, decrease in crystallinity, reversal in the degree of melt evolution and, potentially, increase in average melt temperature. The decrease in crystallinity in particular may have conditioned the magmatic system for the cataclysmic eruption by driving it from rheologically immobile to mobile conditions; however, with our data we cannot address the ultimate eruption trigger. The insights gained from the zircon record, aided by estimates of magma storage conditions from major mineral phases, make the Kneeling Nun Tuff an extraordinary subject to develop new ways of studying the pre-eruptive history of magmas.

Acknowledgements

This research was supported by Swiss National Science Foundation grant 200021–155923. We thank F. Forni for detailed discussions, M. Guillong for help with laser ablation analyses, and D. Klimentyeva, G. Ligęza, L. Zehnder and M. Castellanos for help with sample characterisation.

Appendix

Supplementary information to this chapter can be found in Appendix B.

References

Arzilli, F., Fabbrizio, A., Schmidt, M.W., Petrelli, M., Maimaiti, M., Dingwell, D.B., Paris, E., Burton, M., Carroll, M.R., 2018. The effect of diffusive re-equilibration time on trace element partitioning between alkali feldspar and trachytic melts. Chem. Geol. 495, 50–66.

Bachmann, O., Bergantz, G.W., 2003. Rejuvenation of the Fish Canyon magma body: A window into the evolution of large-volume silicic magma systems. Geology 31, 789-792.

Bachmann, O., Dungan, M.A., Lipman, P.W., 2002. The Fish Canyon magma body, San Juan volcanic field, Colorado: Rejuvenation and eruption of an upper-crustal batholith. J. Petrol. 43, 1469-1503.

Barboni, M., Boehnke, P., Schmitt, A.K., Harrison, T.M., Shane, P., Bouvier, A.-S., Baumgartner, L., 2016. Warm storage for arc magmas. Proc. Natl. Acad. Sci. USA 113, 13959-13964.

Burgisser, A., Bergantz, G.W., 2011. A rapid mechanism to remobilize and homogenize highly crystalline magma bodies. Nature 471, 212-215.

Chapin, C.E., Wilks, M., McIntosh, W.C., 2004. Space-time patterns of Late Cretaceous to present magmatism in New Mexico—Comparison with Andean volcanism and potential for future volcanism. N.M. Bur. Geol. Miner. Res. Bull. 160, 13-40.

Cherniak, D.J., Watson, E.B., 2003. Diffusion in zircon. Rev. Mineral. Geochem. 53, 113-143.

Claiborne, L.L., Miller, C.F., Gualda, G.A., Carley, T.L., Covey, A.K., Wooden, J.L., Fleming, M.A., 2018. Zircon as magma monitor: robust, temperature-dependent partition coefficients from glass and zircon surface and rim measurements from natural systems, in: Moser, D.E., Corfu, F., Darling, J.R., Reddy, S.M., Tait, K. (Eds.), Microstructural Geochronology: Planetary Records Down to Atom Scale, Geophysical Monograph 232.

Coleman, D.S., Gray, W., Glazner, A.F., 2004. Rethinking the emplacement and evolution of zoned plutons: Geochronologic evidence for incremental assembly of the Tuolumne Intrusive Suite, California. Geology 32, 433.

Coney, P.J., Reynolds, S.J., 1977. Cordilleran Benioff Zones. Nature 270, 403-406.

Cooper, K.M., 2015. Timescales of crustal magma reservoir processes: insights from U-series crystal ages. Geol. Soc. Spec. Publ. 422, 141-174.

Cooper, K.M., Kent, A.J.R., 2014. Rapid remobilization of magmatic crystals kept in cold storage. Nature 506, 480-483.

Costa, F., 2008. Residence times of silicic magmas associated with calderas, in: Gottsmann, J., Martí, J. (Eds.), Caldera Volcanism: Analysis, Modelling and Response: Developments in Volcanology Vol. 10. Elsevier, Amsterdam, pp. 1-55.

Costa, F., Dohmen, R., Chakraborty, S., 2008. Time scales of magmatic processes from modeling the zoning patterns of crystals. Rev. Mineral. Geochem. 69, 545-594.

Davis, J.M., Hawkesworth, C.J., 1993. The petrogenesis of 30–20 Ma basic and intermediate volcanics from the Mogollon-Datil Volcanic Field, New Mexico, USA. Contrib. Mineral. Petrol. 115, 165-183.

Elston, W.E., 1957. Geology and mineral resources of Dwyer quadrangle, Grant, Luna, and Sierra Counties, New Mexico. N.M. Bur. Mines Miner. Res. Bull. 38.

Elston, W.E., 1984. Mid-Tertiary ash flow tuff cauldrons, southwestern New Mexico. J. Geophys. Res. 89, 8733-8750.

Elston, W.E., 1989. Day 5: Field guide to the Emory caldera along NM-152 and in Tierra Blanca Canyon, in: Chapin, C.E., Zidek, J. (Eds.), Field excursions to volcanic terranes in the western United States, Volume I: Southern Rocky Mountain region, pp. 91-106.

Elston, W.E., Seager, W.R., Clemons, R.E., 1975. Emory Cauldron, Black Range, New Mexico, source of the Kneeling Nun Tuff, in: Seager, W.R., Clemons, R.E., Callender, J.F. (Eds.), N.M. Geol. Soc. 26th Fall Field Conf. Guidebook, pp. 283-292.

Farmer, G.L., Bailley, T., Elkins-Tanton, L.T., 2007. Mantle source volumes and the origin of the mid-Tertiary ignimbrite flare-up in the southern Rocky Mountains, western US. Lithos 102, 279-294.

Ferry, J.M., Watson, E.B., 2007. New thermodynamic models and revised calibrations for the Ti-in-zircon and Zr-in-rutile thermometers. Contrib. Mineral. Petrol. 154, 429-437.

Flinders, A.F., Shelly, D.R., Dawson, P.B., Hill, D.P., Tripoli, B., Shen, Y., 2018. Seismic evidence for significant melt beneath the Long Valley Caldera, California, USA. Geology 46, 799–802.

Forni, F., Bachmann, O., Mollo, S., De Astis, G., Gelman, S.E., Ellis, B.S., 2016. The origin of a zoned ignimbrite: Insights into the Campanian Ignimbrite magma chamber (Campi Flegrei, Italy). Earth Planet. Sci. Lett. 449, 259-271.

Gelman, S.E., Gutierrez, F.J., Bachmann, O., 2013. On the longevity of large upper crustal silicic magma reservoirs. Geology 41, 759-762.

Giles, D., 1965. Some aspects of the Kneeling Nun rhyolite tuff, in: Fitzsimmons, J.P., Balk, C.L. (Eds.), NM Geol. Soc. 16th Fall Field Conf. Guidebook, pp. 164-166.

Giles, D.L., 1968. Ash-flow tuffs of the Cobre Mountains, in: Titley, S.R. (Ed.), Arizona Geological Society Southern Arizona Guidebook III, pp. 289-291.

Gradstein, F., Ogg, J., Schmitz, M., Ogg, G., 2012. The Geologic Timescale 2012. Elsevier, Oxford.

Holland, T., Blundy, J., 1994. Non-ideal interactions in calcic amphiboles and their bearing on amphibole-plagioclase thermometry. Contrib. Mineral. Petrol. 116, 433-447.

Huber, C., Bachmann, O., Dufek, J., 2012. Crystal-poor versus crystal-rich ignimbrites: A competition between stirring and reactivation. Geology 40, 115-118.

Kaiser, J.F., de Silva, S., Schmitt, A.K., Economos, R., Sunagua, M., 2017. Million-year melt–presence in monotonous intermediate magma for a volcanic–plutonic assemblage in the Central Andes: Contrasting histories of crystal-rich and crystal-poor super-sized silicic magmas. Earth Planet. Sci. Lett. 457, 73-86.

Karakas, O., Degruyter, W., Bachmann, O., Dufek, J., 2017. Lifetime and size of shallow magma bodies controlled by crustal-scale magmatism. Nat. Geosci. 10, 446-450.

Kent, A.J.R., Cooper, K.M., 2017. How well do zircons record the thermal evolution of magmatic systems? Geology 46, 111-114.

Kuellmer, F.J., 1954. Geologic section of the Black Range at Kingston, New Mexico. N.M. Bur. Mines Miner. Res. Bull. 33.

Kuiper, K.F., Deino, A., Hilgen, F.J., Krijgsman, W., Renne, P.R., Wijbrans, J.R., 2008. Synchronizing rock clocks of Earth history. Science 320, 500-504.

Lipman, P.W., 2007. Incremental assembly and prolonged consolidation of Cordilleran magma chambers: Evidence from the Southern Rocky Mountain volcanic field. Geosphere 3, 42.

Lipman, P.W., Prostka, H.J., Christiansen, R.L., 1972. Cenozoic volcanism and plate-tectonic evolution of the western United States. I. Early and middle Cenozoic. Philos. T. Roy. Soc. A 271, 217-248.

Marsh, B.D., 1981. On the crystallinity, probability of occurrence, and rheology of lava and magma. Contrib. Mineral. Petrol. 78, 85-98.

Mason, B.G., Pyle, D.M., Oppenheimer, C., 2004. The size and frequency of the largest explosive eruptions on Earth. Bull. Volcanol. 66, 735-748.

Matthews, N.E., Vazquez, J.A., Calvert, A.T., 2015. Age of the Lava Creek supereruption and magma chamber assembly at Yellowstone based on $^{40}Ar/^{39}Ar$ and U–Pb dating of sanidine and zircon crystals. Geochem. Geophys. Geosyst. 16, 2508-2528.

McDowell, F.W., McIntosh, W.C., 2012. Timing of intense magmatic episodes in the northern and central Sierra Madre Occidental, western Mexico. Geosphere 8, 1505.

McIntosh, W.C., Chapin, C.E., Ratté, J.C., Sutter, J.F., 1992. Time-stratigraphic framework for the Eocene-Oligocene Mogollon-Datil volcanic field, southwest New Mexico. Geol. Soc. Am. Bull. 104, 851-871.

McIntosh, W.C., Sutter, J.F., Chapin, C.E., Kedzie, L.L., 1990. High-precision $^{40}Ar/^{39}Ar$ sanidine geochronology of ignimbrites in the Mogollon-Datil volcanic field, southwestern New Mexico. Bull. Volcanol. 52, 584-601.

Melnik, O.E., Bindeman, I.N., 2018. Modeling of trace elemental zoning patterns in accessory minerals with emphasis on the origin of micrometer-scale oscillatory zoning in zircon. Am. Mineral. 103, 355-368.

Molloy, C., Shane, P., Nairn, I., 2008. Pre-eruption thermal rejuvenation and stirring of a partly crystalline rhyolite pluton revealed by the Earthquake Flat Pyroclastics deposits, New Zealand. J. Geol. Soc. London 165, 435-447.

Mutch, E.J.F., Blundy, J.D., Tattitch, B.C., Cooper, F.J., Brooker, R.A., 2016. An experimental study of amphibole stability in low-pressure granitic magmas and a revised Al-in-hornblende geobarometer. Contrib. Mineral. Petrol. 171, 85.

Putirka, K.D., 2008. Thermometers and barometers for volcanic systems. Rev. Mineral. Geochem. 69, 61-120.

Rivera, T.A., Schmitz, M.D., Crowley, J.L., Storey, M., 2014. Rapid magma evolution constrained by zircon petrochronology and $^{40}Ar/^{39}Ar$ sanidine ages for the Huckleberry Ridge Tuff, Yellowstone, USA. Geology 42, 643-646.

Samperton, K.M., Schoene, B., Cottle, J.M., Brenhin Keller, C., Crowley, J.L., Schmitz, M.D., 2015. Magma emplacement, differentiation and cooling in the middle crust: Integrated zircon geochronological–geochemical constraints from the Bergell Intrusion, Central Alps. Chem. Geol. 417, 322-340.

Schaltegger, U., Brack, P., Ovtcharova, M., Peytcheva, I., Schoene, B., Stracke, A., Marocchi, M., Bargossi, G.M., 2009. Zircon and titanite recording 1.5 million years of magma accretion, crystallization and initial cooling in a composite pluton (southern Adamello batholith, northern Italy). Earth Planet. Sci. Lett. 286, 208-218.

Schmitz, M.D., Davydov, V.I., 2011. Quantitative radiometric and biostratigraphic calibration of the Pennsylvanian-Early Permian (Cisuralian) time scale and pan-Euramerican chronostratigraphic correlation. Geol. Soc. Am. Bull. 124, 549-577.

Schoene, B., Latkoczy, C., Schaltegger, U., Günther, D., 2010. A new method integrating high-precision U–Pb geochronology with zircon trace element analysis (U–Pb TIMS-TEA). Geochim. Cosmochim. Acta 74, 7144-7159.

Schoene, B., Samperton, K.M., Eddy, M.P., Keller, G., Adatte, T., Bowring, S.A., Khadri, S.F., Gertsch, B., 2015. U-Pb geochronology of the Deccan Traps and relation to the end-Cretaceous mass extinction. Science 347, 182-184.

Schoene, B., Schaltegger, U., Brack, P., Latkoczy, C., Stracke, A., Günther, D., 2012. Rates of magma differentiation and emplacement in a ballooning pluton recorded by U–Pb TIMS-TEA, Adamello batholith, Italy. Earth Planet. Sci. Lett. 355-356, 162-173.

Self, S., 2006. The effects and consequences of very large explosive volcanic eruptions. Philos. T. Roy. Soc. A 364, 2073-2097.

Stelten, M.E., Cooper, K.M., Vazquez, J.A., Reid, M.R., Barfod, G.H., Wimpenny, J., Yin, Q.-z., 2013. Magma mixing and the generation of isotopically juvenile silicic magma at Yellowstone caldera inferred from coupling 238U–230Th ages with trace elements and Hf and O isotopes in zircon and Pb isotopes in sanidine. Contrib. Mineral. Petrol. 166, 587-613.

Szymanowski, D., Fehr, M.A., Guillong, M., Coble, M.A., Wotzlaw, J.F., Nasdala, L., Ellis, B.S., Bachmann, O., Schönbächler, M., 2018. Isotope-dilution anchoring of zircon reference materials for accurate Ti-in-zircon thermometry. Chem. Geol. 481, 146-154.

Szymanowski, D., Wotzlaw, J.F., Ellis, B.S., Bachmann, O., Guillong, M., von Quadt, A., 2017. Protracted near-solidus storage and pre-eruptive rejuvenation of large magma reservoirs. Nat. Geosci. 10, 777-782.

Tierney, C.R., Schmitt, A.K., Lovera, O.M., de Silva, S.L., 2016. Voluminous plutonism during volcanic quiescence revealed by thermochemical modeling of zircon. Geology 44, 683-686.

Vazquez, J.A., Reid, M.R., 2004. Probing the accumulation history of the voluminous Toba magma. Science 305, 991-994.

Wark, D.A., Hildreth, W., Spear, F.S., Cherniak, D.J., Watson, E.B., 2007. Pre-eruption recharge of the Bishop magma system. Geology 35, 235-238.

Watson, E.B., 1996. Dissolution, growth and survival of zircons during crustal fusion: Kinetic principles, geological models and implications for isotopic inheritance. Trans. R. Soc. Edinburgh Earth Sci. 87, 43-56.

Wolff, J.A., Ellis, B.S., Ramos, F.C., Starkel, W.A., Boroughs, S., Olin, P.H., Bachmann, O., 2015. Remelting of cumulates as a process for producing chemical zoning in silicic tuffs: A comparison of cool, wet and hot, dry rhyolitic magma systems. Lithos 236–237, 275-286.

Wotzlaw, J.F., Brack, P., Storck, J.C., 2017. High-resolution stratigraphy and zircon U–Pb geochronology of the Middle Triassic Buchenstein Formation (Dolomites, northern Italy): precession-forcing of hemipelagic carbonate sedimentation and calibration of the Anisian–Ladinian boundary interval. J. Geol. Soc. London 175, 71-85.

Wotzlaw, J.F., Bindeman, I.N., Watts, K.E., Schmitt, A.K., Caricchi, L., Schaltegger, U., 2014. Linking rapid magma reservoir assembly and eruption trigger mechanisms at evolved Yellowstone-type supervolcanoes. Geology 42, 807-810.

Wotzlaw, J.F., Schaltegger, U., Frick, D.A., Dungan, M.A., Gerdes, A., Günther, D., 2013. Tracking the evolution of large-volume silicic magma reservoirs from assembly to supereruption. Geology 41, 867-870.

Chapter 4

Isotope-dilution anchoring of zircon reference materials for accurate Ti-in-zircon thermometry‡

D. Szymanowski, M. A. Fehr, M. Guillong, M. A. Coble, J. F. Wotzlaw, L. Nasdala, B. S. Ellis, O. Bachmann, M. Schönbächler

ABSTRACT

The temperature-dependence of Ti incorporation into zircon can be used to estimate crystallisation conditions and to make inferences about the petrogenesis of host rocks or parental melts. However, the foundation for such temperature estimates —Ti concentration in zircon — is currently determined by a variety of techniques with no common reference. Analyses of Ti in zircon commonly utilise *in situ* microbeam techniques such as secondary ion mass spectrometry (SIMS), laser ablation–inductively coupled plasma mass spectrometry (LA-ICP-MS), and electron probe microanalysis (EPMA). These techniques require external calibrations that are prone to matrix effects, potentially imposing significant errors on Ti concentrations and the derived model temperatures. To improve the accuracy of these determinations, we present a new framework of zircon reference materials for Ti built around two thoroughly characterised zircons, the widely distributed zircon 91500 and the new reference zircon GZ7. Laser ablation ICP-MS and SIMS analyses reveal that the homogeneity with respect to Ti/Si is on the order of 4.1–8.2 % (relative standard deviation, RSD) for zircon 91500 and 1.1 % for zircon GZ7, which is considered sufficient for their use as primary calibration materials. We present independent determinations of Ti concentration in multiple fragments of these two zircon crystals using isotope dilution (ID)-ICP-MS employing a precisely calibrated ^{47}Ti–^{49}Ti double spike. The recommended ID Ti concentration values are $4.73 \pm 0.15\ \mu g\ g^{-1}$ for zircon 91500 and $25.08 \pm 0.18\ \mu g\ g^{-1}$ for zircon GZ7 (95 % confidence level). A set of complementary secondary reference materials is also characterised using LA-ICP-MS with Ti concentrations anchored to the new isotope dilution values, thereby permitting comparisons of Ti-in-zircon datasets whenever data for these secondary reference materials are reported.

‡*This chapter is equivalent to a paper published in* Chemical Geology *(481, 146–154, 2018)*

4.1. Introduction

The temperature-dependence of Ti incorporation into zircon has been exploited as a powerful tool to estimate zircon crystallisation temperatures (Ti-in-zircon thermometer; Watson et al., 2006; Ferry and Watson, 2007). Since the original calibration, the Ti-in-zircon thermometer has been extensively applied to a range of natural zircon crystals to study a wide variety of geological problems, including the formation of the Earth's early crust (Watson and Harrison, 2005; Coogan and Hinton, 2006; Harrison and Schmitt, 2007; Harrison et al., 2007; Trail et al., 2007; Hiess et al., 2008; Darling et al., 2009; Kenny et al., 2016), modern oceanic and continental crust generation (Grimes et al., 2009; Barth et al., 2017; Schmitt et al., 2017), the thermal conditions of silicic magma generation and storage (Fu et al., 2008; Claiborne et al., 2010; Reid et al., 2011; Klemetti and Clynne, 2014; Matthews et al., 2015; Barboni et al., 2016; Rivera et al., 2016; Kaiser et al., 2017; Szymanowski et al., 2017), kimberlite formation (Page et al., 2007) or metamorphic P–T paths (Baldwin et al., 2007; Clark et al., 2009; Ewing et al., 2013). The accuracy of model Ti-in-zircon temperatures depends fundamentally on the accuracy of the thermometer calibration, assumptions made about the activities of TiO_2 and SiO_2 in the chemical environment (particularly in the absence of co-crystallising rutile or quartz), and potentially crystallisation pressure (Ferry and Watson, 2007; Ferriss et al., 2008). However, given informed choices of chemical potentials (e.g. Hayden and Watson, 2007; Wark et al., 2007; Ickert et al., 2011; Reid et al., 2011; Ghiorso and Gualda, 2013; Kularatne and Audétat, 2014) and an adequate pressure correction can be made, the accuracy of Ti-in-zircon temperature estimates ultimately hinges on the ability to accurately determine low Ti concentrations in zircon.

The analytical techniques commonly employed for measuring Ti *in situ* in zircon crystals include secondary ion mass spectrometry (SIMS), laser ablation–inductively coupled plasma mass spectrometry (LA-ICP-MS), and electron probe microanalysis (EPMA). The applicability of EPMA is limited to only the highest-Ti zircons (>>10 μg g^{-1} Ti). Therefore, Ti concentrations pertinent to most igneous and metamorphic zircons (<1 to ~50 μg g^{-1} Ti corresponding to crystallisation temperatures of ~500–900 °C) are most commonly determined by SIMS or LA-ICP-MS, as these methods achieve high sensitivity, yielding detection limits at the sub-ppm level for Ti and other elements. However, accurate calibration of these two analytical techniques requires the use of primary reference materials that are compositionally and structurally matrix-matched (Shimizu and Hart, 1982; Durrant, 1999; Arevalo, 2014; Ireland, 2014). Currently, despite the rapidly growing popularity of *in situ* trace element and isotopic analyses of zircon, there is an evident lack of suitable zircon reference materials that have an independently determined and traceable value for Ti concentration that can be used for relative trace element determinations via SIMS or LA-ICP-MS.

To improve the accuracy of *in situ* analyses of Ti in zircon, we evaluated the homogeneity of existing zircon reference materials with respect to their Ti concentration. We

have identified two zircon reference materials, zircon 91500 (Wiedenbeck et al., 1995; 2004) and zircon GZ7, to be sufficiently rich and homogeneous in Ti to serve as primary reference materials for SIMS and LA-ICP-MS analyses of Ti in zircon. We present independent determinations of the Ti concentration in multiple fragments of these two zircon crystals using isotope dilution (ID)-ICP-MS employing a precisely calibrated ^{47}Ti–^{49}Ti double spike. We then evaluate the effect of using matrix-matched reference materials for analyses of Ti in zircon and use the new ID concentration values to derive Ti contents in a range of other zircons to be used as either primary or secondary reference materials.

4.2. Materials

In search of an ideal zircon reference material for Ti in zircon, the following criteria were considered: (1) homogeneity in Ti on a variety of spatial scales, (2) a suitably high Ti concentration that would limit the amount of extrapolation in analyses of high-Ti zircons, (3) long-term availability and wide distribution across many laboratories, and, if possible, (4) good existing characterisation for other elements and isotopic systems (e.g. U–Pb, Hf, O). Since homogeneity in Ti is difficult to evaluate based on available analytical data, we chose to test promising zircon reference materials for intra-crystalline variability in Ti. The exceptionally well-characterised zircon 91500 at ~5 μg g^{-1} Ti and the newly-characterised zircon GZ7 at ~25 μg g^{-1} Ti were found to satisfy the stated criteria most closely.

4.2.1. Zircon 91500

Zircon 91500 is a large, inclusion-free zircon crystal initially proposed as a reference material by Wiedenbeck et al. (1995). This single crystal of original mass of 238 g obtained from the Harvard Mineralogical Museum is sourced from a 1065 Ma syenitic pegmatite in Renfrew County, Ontario, Canada. Initial characterisation (Wiedenbeck et al., 1995) included U–Pb and Lu–Hf systematics, major element and rare earth element analyses; the high degree of homogeneity in U–Pb and Lu–Hf resulted in many laboratories adopting 91500 as a reference material predominantly for these two isotopic systems. A more detailed second characterisation (Wiedenbeck et al., 2004) included a multi-laboratory comparison of the composition of 91500 in major elements (EPMA), trace elements (SIMS, LA-ICP-MS) and oxygen isotopes (laser fluorination). A high degree of inter- and intra-grain homogeneity was shown for Si, Zr, O isotopes and a suite of high-abundance trace elements (Y+REE typically within a standard deviation of 5–25% except the low-abundance La, Pr). However, some samples were found to be heterogeneous in several light elements (Li, Be, B, F, Cl). Importantly, cathodoluminescence (CL) and backscattered electron (BSE) imaging of Wiedenbeck et al. (2004) identified a significant proportion of crystal fragments containing anomalous banding associated with increased U, Y and REE contents as well as enhanced radiation damage. The authors advised initial CL and BSE screening of used crystal fragments in order to avoid such domains. No Ti concentration data were reported by either of the characteri-

sation exercises, but available *in situ* data for zircon 91500 utilising SIMS or LA-ICP-MS with diverse calibration approaches (Yuan et al., 2004; Schmitt and Vazquez, 2006; Liu et al., 2010; Reid et al., 2011; Bruand et al., 2014) suggest a Ti content in the range of 4.0–6.8 μg g^{-1}.

4.2.2. Zircon GZ7

Zircon GZ7 was a cut and faceted, clear, apparently unzoned, light orange-brownish gemstone specimen. The oval stone had a maximum dimension of 16.75 mm and a weight of 19.2 ct (3.84 g). The gem was purchased in the Ratnapura, Sri Lanka, gem market in 2014. The stone originated from a placer deposit in the Kalu Ganga valley in the Ratnapura area, which belongs to the Sri Lankan Highland Complex (Kröner et al., 1994; Zoysa, 2014). The original rocks that hosted such homogeneous zircon specimens remain unknown to date. Based on extensive $\delta^{18}O$ analyses, Cavosie et al. (2011) concluded that at least some of the homogeneous Sri Lankan zircon specimens cannot be of igneous origin but likely have formed in a marble or a metamorphic Ca-silicate rock.

A comprehensive description of GZ7, including its proposal as U–Pb reference, is currently in preparation (Nasdala et al., in press). Zircon GZ7 is characterised by a lack of any noticeable zoning, or other features of internal heterogeneity, observed in BSE and CL images, EPMA element maps, and spectroscopic hyperspectral maps. According to U–Pb results obtained by means of isotope dilution–thermal ionisation mass spectrometry (ID-TIMS), zircon GZ7 has an age of ca. 530 Ma that is concordant within the uncertainties of the decay constants. By means of LA-ICP-MS analysis, mean actinide contents of 680 μg g^{-1} U and 611 μg g^{-1} Th were determined. Consequently, zircon GZ7 has been affected by a moderate time-integrated alpha-decay dose of 1.49×10^{18} g^{-1} since the time of closure of its U–Pb isotope system. This is consistent with the moderate unit-cell expansion and Raman-band broadening observed, indicating a significant but still moderate degree of self-irradiation damage. (U–Th)/He analyses of zircon GZ7 yielded an age of ca. 438 Ma. This apparent cooling age is consistent with (U–Th)/He ages of other unheated Sri Lankan zircon samples (Hurley, 1954; Nasdala et al., 2004) and, therefore, allows us to conclude that gem specimen GZ7 had never been subjected to heat treatment for colour enhancement or other purposes.

4.3. Analytical methods

4.3.1. LA-ICP-MS trace element analyses

Laser ablation ICP-MS analyses were performed with an ASI Resolution 155 laser ablation system coupled to a Thermo Element XR sector-field ICP-MS at the Institute of Geochemistry and Petrology, ETH Zürich using a 193 nm ArF excimer laser. Ablation spot size was 30 μm, energy density on the sample was set to 2.5 J cm^{-2} and the repetition rate was 5 Hz (Guillong et al., 2014). All analyses were performed using the triple detector mode automatically switching between pulse-counting secondary electron multiplier (SEM), analog SEM, and Faraday detectors; the analog conversion factor (ACF)

was updated automatically. Isotopes acquired were $^{27}Al^+$, $^{29}Si^+$, $^{31}P^+$, $^{91}Zr^+$, and $^{49}Ti^+$ which was chosen to avoid interferences from Zr^{2+} that dominate the signal on other Ti masses (46–48) in low mass resolution mode. Al and P were monitored for the presence of mineral and melt inclusions. Intensities were recorded for 70 s, which included 30 s gas blank and 40 s sample signal. Raw integrated count rates were corrected for gas blank and for drift based on interspersed analyses of either GJ-1 zircon (Jackson et al., 2004) during homogeneity tests or 91500/GZ7 in the remaining analytical sessions.

4.3.2. SIMS trace element analyses

Zircon trace element analyses by SIMS were performed using the SHRIMP-RG (sensitive high resolution ion microprobe–reverse geometry) ion microprobe co-operated by the U.S. Geological Survey and Stanford University. Secondary ions were sputtered from the target using an O^{2-} primary ion beam with an intensity varying from 2.3 to 2.6 nA. The primary ion spot had a diameter between 16–18 µm and a depth of ~1.5 µm. Before every analysis, the sample surface was cleaned by rastering the primary beam for 60 s, and the primary and secondary beams were auto-tuned to maximise transmission. The acquisition routine included analysis of $^{23}Na^+$, $^{27}Al^+$, $^{30}Si^+$, $^{31}P^+$, $^{39}K^+$, $^{40}Ca^+$, $^{48}Ti^+$, $^{49}Ti^+$, $^{56}Fe^+$, and $^{96}Zr^+$. All analyses were performed using a single scan by peak-hopping cycles through the mass table, and each mass was measured on a single ETP® discrete-dynode electron multiplier operated in pulse counting mode. Counting times for trace element measurements ranged from 2 to 10 s per mass to optimise counting statistics for each isotope.

Measurements were performed using a mass resolution of M/ΔM~10,500 (10% peak height), which eliminates interfering ionic and molecular species. At *m/z* 48, the major interferences include $^{48}Ca^+$ and $^{96}Zr^{2+}$, which require a mass resolution of 10,480 and 7,165 to fully resolve from $^{48}Ti^+$, respectively. The less abundant isotope ^{49}Ti was also measured, and the natural $^{48}Ti/^{49}Ti = 13.6$ was monitored to ensure accurate measurement. Ti concentrations were calculated using ^{48}Ti and normalised to ^{30}Si to correct for differences in instrument conditions between subsequent analyses. Other trace elements (Na, Al, P, K, Ca, and Fe) were monitored to ensure that analyses did not include surface contamination, micro-inclusions or cracks.

4.3.3. ID-ICP-MS Ti concentration analyses

Titanium concentration analyses by ID-ICP-MS were performed using a ^{47}Ti–^{49}Ti double spike that was prepared and calibrated for Ti stable isotope analyses (Williams, 2014; Williams et al., 2014). The spike concentration was determined relative to a gravimetrically prepared Ti standard by reverse isotope dilution. The accuracy of the spike calibration and the Ti isotope dilution procedure is additionally verified by Ti concentration determinations of magmatic rock reference materials, which agree well with reference values (Table C1).

Aliquots of 1–10 mg zircon were prepared by rinsing the fragments with 4 M HNO_3, ultrapure water and acetone. Prior to dissolution, 15–100 µl of ^{47}Ti–^{49}Ti double spike was added to pre-cleaned 300 µl Savillex microcapsules, weighed repeatedly on a Mettler Toledo UMX2 microbalance and dried. Zircon grains were then placed in the pre-spiked containers and weighed repeatedly using the same balance. 20 drops (~150 µl) of 29 M HF were added to the microcapsules, which were then assembled in a Teflon liner filled with 7 ml HF + trace HNO_3 that was sealed in a Parr pressure vessel for dissolution following Krogh (1973). Due to the large size of the zircon fragments, samples were digested and equilibrated with the tracer for one week at 210 °C. In every case zircon digestion in HF created a residue of fluoride salts that was completely re-dissolved within a few hours in 6 M HCl in a Parr bomb held at 180 °C. At this stage samples were visually inspected under a microscope for any undissolved residue; if any remaining zircon fragments were identified, the digestion procedure was repeated for another week. The final solutions were evaporated and re-dissolved in 0.5 M HNO_3 – 0.012 M HF for ICP-MS analysis, with target concentrations of 2–15 ng g^{-1} Ti. The maximum Ti concentrations of the analysed solutions were limited by the corresponding amount of matrix elements (mostly Zr + Hf) introduced into the mass spectrometer and varied between samples of 91500 and GZ7. Along with the samples, both spiked and unspiked total procedural blanks were prepared identically; the unspiked blanks were dissolved into smaller volumes of solution (0.5 ml) to maximise the likelihood of detection.

The sample solutions were analysed on a Thermo Element XR ICP-MS at the Institute of Geochemistry and Petrology, ETH Zürich. A single measurement typically consumed 0.45 ml of solution (~1–7 ng Ti) with an acquisition time of 4.5 min including a 2 min take-up time. The analyses were performed using a discrete-dynode SEM, acquiring $^{44}Ca^+$, $^{46}Ti^+$, $^{47}Ti^+$, $^{48}Ti^+$, $^{49}Ti^+$, $^{50}Ti^+$, $^{51}V^+$, $^{52}Cr^+$, $^{56}Fe^+$. Measured intensities were corrected for background measured in the 0.5 M HNO_3 – 0.012 M HF acid matrix before and after every sample run. The analyses were run in 'medium' mass resolution ($M/\Delta M \sim 4000$), which cannot fully resolve interferences of $^{92}Zr^{2+}$, $^{94}Zr^{2+}$ and $^{96}Zr^{2+}$ from $^{46}Ti^+$, $^{47}Ti^+$ and $^{48}Ti^+$ respectively. Therefore, analyses of Ti in zircon were focussed on $^{49}Ti^+$ (mostly from the spike) and $^{50}Ti^+$ (dominated by sample contribution) because these masses do not have overlapping interferences from the abundant Zr. While *m/z* 49 is practically interference-free, minor unresolvable interferences from $^{50}Cr^+$ and $^{50}V^+$ were present at *m/z* 50, both metals likely sourced from the digestion procedure in a metal bomb. Both interferences were corrected by peak-stripping based on the measured $^{52}Cr^+$ and $^{51}V^+$ and assuming natural Cr, V isotopic abundances. The interference-corrected $^{50}Ti/^{49}Ti$ ratio was then calculated and corrected for instrumental mass bias determined from $^{50}Ti/^{49}Ti$ measured in natural Ti standards (Alfa Aesar Specpure) bracketing the samples, using the exponential law. Finally, the total mass of Ti in the sample (including blank) was calculated from the background-, interference-, and mass bias-corrected $^{50}Ti/^{49}Ti$, assuming an average terrestrial Ti isotopic composition of the zircon (based on analyses of natural Ti standards by multi-collector ICP-MS). In the last step, the resulting mass

of Ti was corrected for blank contribution. The average mass of the blank was estimated from 25 total procedural blanks that were above detection limit of ~0.01 ng (out of a total of 34 blanks prepared). The blank mass in analytical sessions including zircon 91500 averaged 0.06 ± 0.05 ng Ti ($n = 15$), excluding two outliers of 0.7 and 1.1 ng. In sessions including GZ7 the blank mass was 0.10 ± 0.10 ng Ti ($n = 7$), excluding one outlier of 1.1 ng. The overall consistency of the procedural blank measurements supports their dominantly low level; however, an elevated blank of ~1 ng would result in overestimating the Ti contents of an aliquot by as much as 2–5 % and 2–3 % for 91500 and GZ7, respectively.

4.4. Results

4.4.1. Homogeneity testing

In order to evaluate the homogeneity of the two zircons with respect to their Ti concentration and their suitability as primary Ti reference materials, multiple fragments of the crystals were analysed by LA-ICP-MS (91500, GZ7) and SIMS (91500). Quantification of Ti concentrations in zircons by either LA-ICP-MS or SIMS is typically accomplished by internally normalising the measured Ti intensity to the intensity of a stoichiometric species such as Si (e.g. Harrison and Schmitt, 2007) where both Ti and Si can be measured as cations or anions, and as metal, oxide, dioxide, or doubly-charged species. Assuming that the Si content of the individual zircon crystals is invariable (e.g. Wiedenbeck et al., 2004 for 91500), we therefore report the results of the homogeneity tests in terms of the Ti/Si ratio measured using the two techniques (Fig. 4.1).

4.4.1.1. Zircon 91500

LA-ICP-MS data were collected across 15 fragments of zircon 91500 chosen without screening for dark-CL regions, with up to 5 ablation spots per fragment (Fig. 4.1a). The results show a large degree of homogeneity both within the individual shards (standard deviations of 1.1–5.1 %) and between them (4.1 % RSD of all analyses). The small difference between the intra- and inter-grain scatter suggests that no systematic difference between individual fragments exists at the precision and spatial resolution of LA-ICP-MS.

The SHRIMP-RG ion microprobe analyses were performed with two to eight spots across a separate set of 11 fragments of zircon 91500, depending on their size (Fig. 4.1b). Spot locations were chosen indiscriminately, without bias towards bright or dark regions in CL. The results show significantly more inter-grain scatter than the LA-ICP-MS data, but with a similar degree of homogeneity of the individual shards. Standard deviations of Ti/Si within single fragments were between 0.3–5.8 %. The SHRIMP-RG results display a larger overall scatter (1 RSD of 8.2 %) than both the LA-ICP-MS data and analyses of any individual fragment by SHRIMP-RG, which suggests that some real piece-to-piece Ti/Si variability may exist in the 91500 zircon. It is also important to note that the total analyte volume of SIMS measurements (1.5–2 ng) is ~40 to 60 times smaller than the volume of material consumed by LA-ICP-MS. Thus, compositional heterogeneity on the micron scale may be averaged in LA-ICP-MS analyses, whereas the relatively

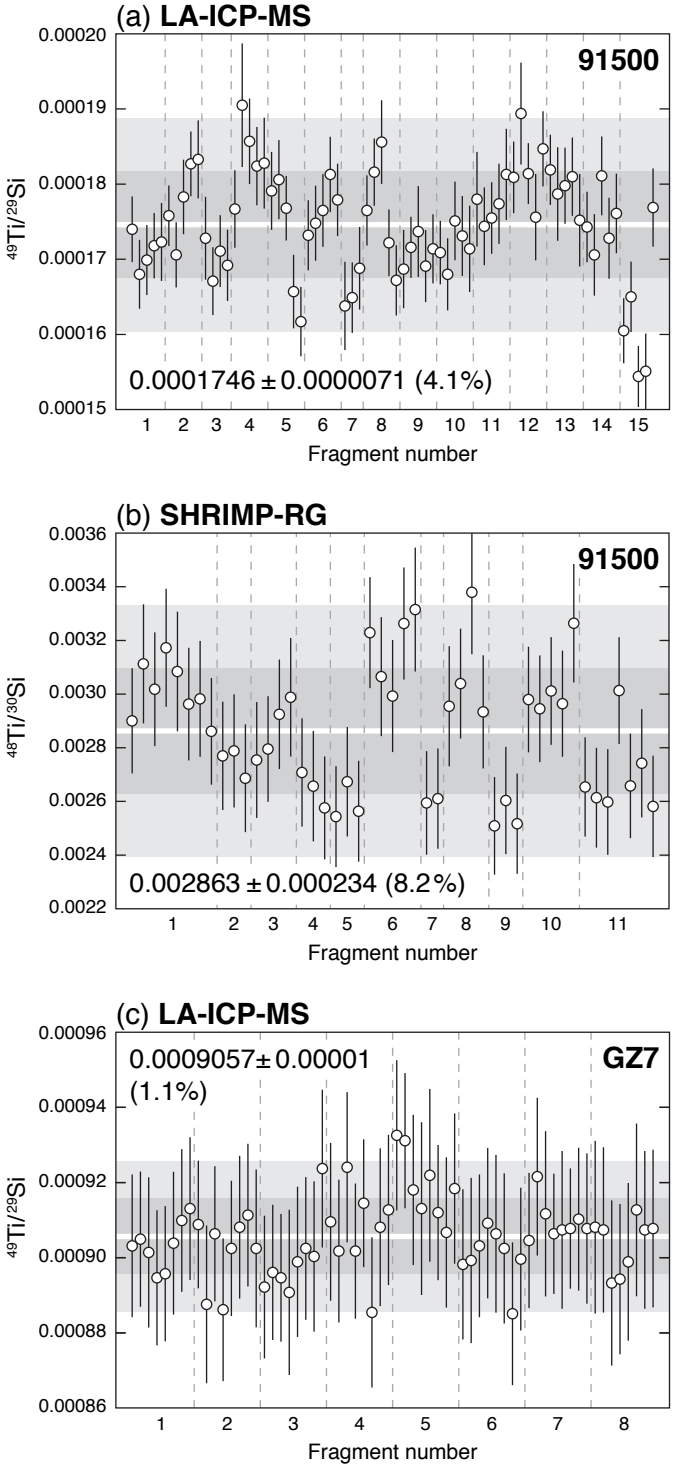

Figure 4.1. Variability of Ti/Si across multiple fragments of zircons 91500 and GZ7 determined by (**a**, **c**) LA-ICP-MS at ETH Zürich and (**b**) SIMS using the SHRIMP-RG at the Stanford–USGS Ion Microprobe Laboratory. Individual analyses are shown with 2σ error bars. The dark and light grey areas represent 1 and 2 SD of the data, respectively; the white lines denote the mean. 1 RSD is given in brackets.

slow sputter rate of SIMS makes it more sensitive to heterogeneity at such small spatial scales.

The reproducibility across multiple fragments is 4.1 and 8.2 % (1 RSD) for LA-ICP-MS and SHRIMP-RG, respectively, which indicates non-negligible heterogeneity of 91500 in terms of Ti/Si. However, the magnitude of the between-grain differences is comparable to analytical uncertainties achieved by both *in situ* methods. Therefore, the reported level of homogeneity of zircon 91500 is considered sufficient for it to be used as a primary reference material, with the caveat that it may require collecting large datasets measured across multiple fragments of this zircon to fully capture its internal variability.

4.4.1.2. Zircon GZ7

The homogeneity of zircon GZ7 was evaluated by LA-ICP-MS by repeated analyses across 8 separate, large fragments of the gem. The results (Fig. 4.1c) show a remarkable degree of homogeneity of this zircon with overall reproducibility of all Ti/Si measurements of 1.1 % (1 RSD). No systematic differences between the fragments were observed, while the degree of homogeneity of individual fragments is similar to that of the entire dataset (RSD of 0.5–1.2 %). Given its high Ti contents and the remarkable homogeneity, the newly characterised zircon GZ7 appears an ideal candidate for a primary reference material.

4.4.2. Isotope dilution ICP-MS analyses

4.4.2.1. Zircon 91500

Eight aliquots consisting of multiple fragments of zircon 91500 were analysed in two separate sequences of dissolution followed by ICP-MS measurements (Table 4.1, Fig. 4.2). The first cycle included three ~4 mg aliquots, for the second set sample sizes were increased to 5–10 mg with the aim of reducing the magnitude of the blank correction. Each solution was analysed 4–6 times which allowed the $^{50}Ti/^{49}Ti$ to be determined with an analytical uncertainty of 0.4–2.9 % (2 SE). The final individual uncertainties on the mass of Ti in the sample are 4.3–5.5 % (Table 4.1), where the difference is dominated by the contribution from the uncertainty on the instrumental mass bias (60–98 % contribution to variance). Most samples required minor interference corrections mostly from $^{50}Cr^{+}$ (1–4 % of total intensity on *m/z* 50); aliquots 7 and 8 had elevated levels of Cr which required larger corrections (15 and 18 % respectively). However, the consistency between these two samples and the rest of the dataset suggests that even the large corrections were accurate.

The Ti concentration data (Fig. 4.2a) are entirely consistent across the two experimental sessions and independent of sample size. The data display moderate scatter (3.7 % RSD) which is less than the scatter in Ti determined by *in situ* methods (4.1 and 8.2 %); we attribute the apparent reduction in variability to averaging over 4–10 mg of dissolved ma-

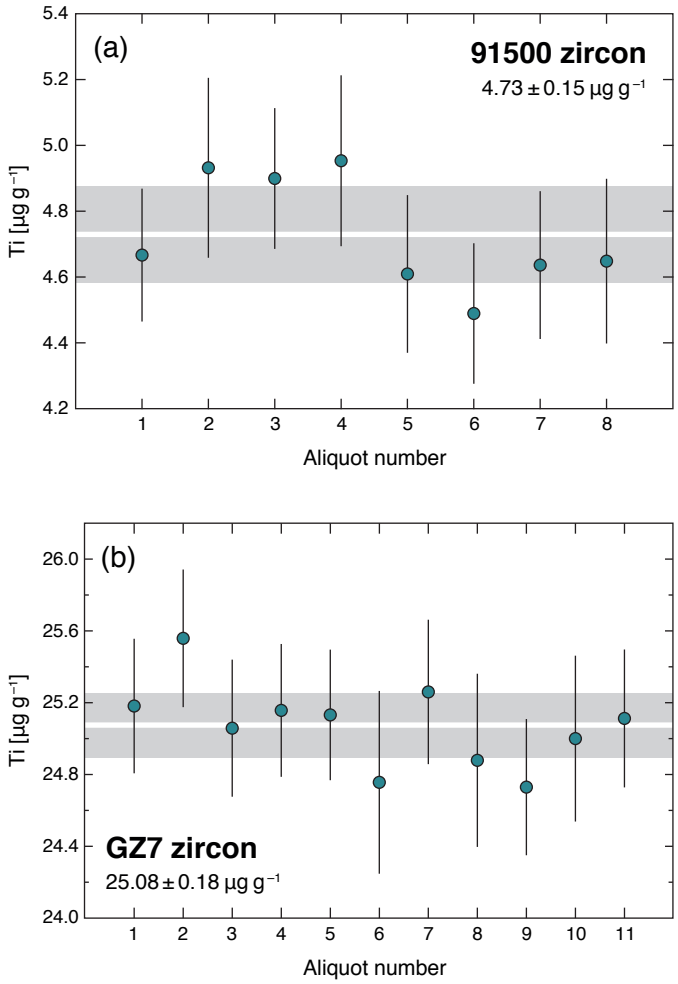

Figure 4.2. Ti contents of zircons 91500 (**a**) and GZ7 (**b**) determined by isotope dilution. The grey shaded area represents the 95 % confidence interval around the mean of the measurements.

terial. The unweighted mean Ti concentration in zircon 91500 is 4.73 ± 0.15 µg g^{-1} (95 % confidence interval; CI), which is our preferred reference value for this zircon.

4.4.2.2. Zircon GZ7

Eleven aliquots comprised of one or two fragments of zircon GZ7 were measured in two separate analytical sessions (sessions 3, 4; Table 4.1). Compared to 91500, the high Ti content of GZ7 allowed smaller aliquots (mostly ≤ 2 mg) which facilitated full dissolution and permitted a larger number of analyses to be performed. The analyses were also run at higher intensities which resulted in improved counting statistics and analytical uncertainties of 0.2–1.0 % (2 SE) for $^{50}Ti/^{49}Ti$. Similarly, higher intensities of the correspondingly more concentrated standards improved the precision of the instrumental mass bias determination, which led to final propagated uncertainties of 1.4–2.0 % (Table 4.1). The interferences from $^{50}Cr^{+}$ comprised 1–6 % of the intensity on *m/z* 50.

Table 4.1. Ti contents of zircons 91500 and GZ7 determined by isotope dilution

Aliquot	Session	Weight [µg]	Ti [ng][a]	Ti [µg g^{-1}]
91500				
1	1	4051 ± 2	18.90 ± 0.82	4.67 ± 0.20
2	1	4188 ± 3	20.65 ± 1.15	4.93 ± 0.27
3	1	4163 ± 2	20.39 ± 0.89	4.90 ± 0.21
4	2	9634 ± 1	47.72 ± 2.50	4.95 ± 0.26
5	2	9009 ± 2	41.52 ± 2.16	4.61 ± 0.24
6	2	9760 ± 2	43.81 ± 2.09	4.49 ± 0.21
7	2	9223 ± 1	42.75 ± 2.07	4.64 ± 0.22
8	2	4816 ± 2	22.38 ± 1.21	4.65 ± 0.25
91500 mean[b]				**4.73 ± 0.15**
blank (*n*=15)			0.06 ± 0.05	
GZ7				
1	3	1537 ± 2	38.70 ± 0.57	25.18 ± 0.37
2	3	1361 ± 1	34.78 ± 0.52	25.56 ± 0.38
3	3	1077 ± 1	26.99 ± 0.41	25.06 ± 0.38
4	3	1163 ± 2	29.26 ± 0.43	25.16 ± 0.37
5	3	1031 ± 1	25.91 ± 0.37	25.13 ± 0.36
6	4	1443 ± 4	35.74 ± 0.73	24.77 ± 0.51
7	4	1174 ± 2	29.67 ± 0.47	25.27 ± 0.40
8	4	2033 ± 3	50.59 ± 0.98	24.89 ± 0.48
9	4	1154 ± 2	28.54 ± 0.44	24.74 ± 0.38
10	4	1629 ± 1	40.75 ± 0.75	25.01 ± 0.46
11	4	1613 ± 1	40.53 ± 0.62	25.12 ± 0.38
GZ7 mean[b]				**25.08 ± 0.18**
blank (*n*=7)			0.10 ± 0.10	

All uncertainties given at 2σ level.
[a] includes uncertainty from spike weight, isotope ratio measurement, instrumental mass bias and Ti blank mass
[b] uncertainty of the sample means, including propagated uncertainty on spike calibration, is given as 95 % CI (confidence interval)

In the case of GZ7, the isotope dilution concentration data are equally consistent between the two analytical sessions (Fig. 4.2b). The scatter of the individual aliquot Ti concentrations is 0.9 % (1 RSD) which is essentially identical to the results of LA-ICP-MS homogeneity tests (1.1 %) and additionally confirms the high degree of homogeneity of this reference material. The unweighted mean Ti concentration of GZ7 is 25.08 ± 0.18 µg g^{-1} Ti (95 % CI), which is our recommended reference value for this zircon.

4.5. The importance of using matrix-matched reference materials

Independent and absolute isotope dilution values for Ti concentration in zircons 91500 and GZ7 allow an assessment of potential inaccuracies of *in situ* analyses that utilise primary reference materials that are not matrix-matched, such as commonly used multi-element glasses (e.g. NIST, USGS, MPI-DING reference materials). We evaluated this effect by compiling analyses of unknown zircons from the ETH LA-ICP-MS lab that were measured together with both a glass reference material (NIST SRM 610) and a zircon reference material (91500 zircon). The compilation (Fig. 4.3) shows that standardising to NIST 610 results in apparent Ti contents that are 5–27 % (average 15 %) lower than results of the same analyses standardised to zircon 91500. The magnitude of the difference is particularly important for the calculated model Ti-in-zircon temperatures, which could be underestimated by 5–33 °C when quantifying Ti relative to NIST 610 (Fig. 4.3).

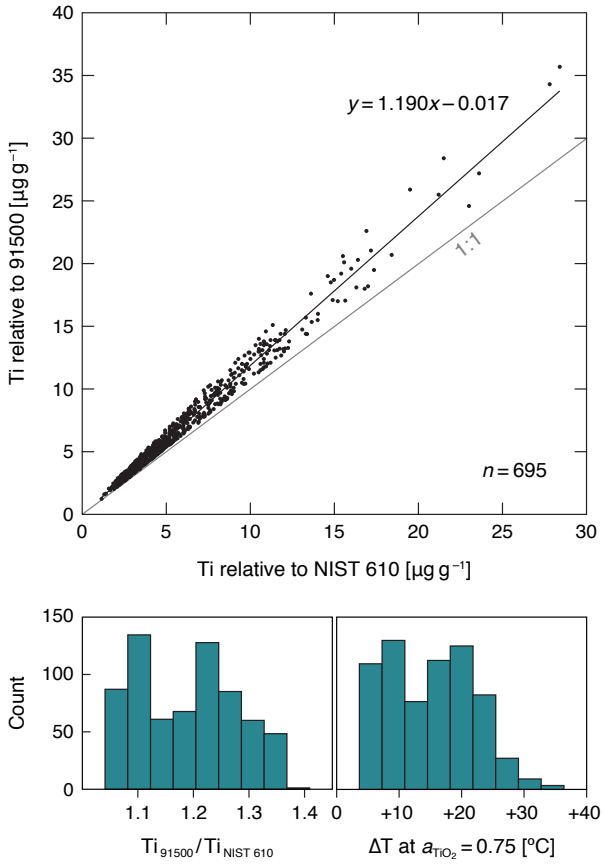

Figure 4.3. Effect of using primary zircon reference materials compared to a NIST SRM glass for quantifying Ti in a suite of zircons from the Kneeling Nun magmatic system. The Ti concentrations were measured by LA-ICP-MS at ETH Zürich and evaluated twice: relative to NIST SRM 610 glass and relative to the newly derived value for Ti in zircon 91500. Using 91500 zircon as primary reference material results in an increase in the obtained Ti concentrations by a factor of 1.06–1.37 which translates into a model temperature increase of 5–33 °C using the formulation of Ferry and Watson (2007) at $a_{TiO_2} = 0.75$, $a_{SiO_2} = 1.0$.

This discrepancy is likely due to contrasting ablation behaviour of zircon and glass, in particular owing to the structural differences between a crystalline and an amorphous material (i.e. mismatched matrix). The effects of such mismatched calibration material are also likely to vary between the *in situ* techniques (LA-ICP-MS vs. SIMS), laser systems, mass spectrometers, analytical sessions (differences in tuning, gas flow or make-up etc.) and the reference materials used (e.g. NIST vs. USGS glasses; Jochum et al., 2007; Liu et al., 2010). In the case of the ETH LA-ICP-MS setup, the offset for a given calibration material appears reproducible over long periods; measurements of 91500 zircon standardised to NIST 610 over an entire year (2016) averaged 4.22 ± 0.42 µg g^{-1} Ti (1 SD, n > 300) which is 11 % lower than the new reference value.

Irrespective of the exact reasons for the 'matrix effects' between glass and zircon, it is important that they are not ignored in applications requiring high accuracy of Ti concentration data in zircon. A potential systematic analytical error of several tens of degrees may significantly bias the interpretations of thermometry results, which is particularly important at low Ti contents (< 5 µg g^{-1}) corresponding to temperatures close to the granitic solidus (~600–750 °C). For example, interpretations of the origin of Hadean zircons from wet minimum melting (Watson and Harrison, 2005; Harrison et al., 2007) rely to a high degree on the accuracy of the model temperatures, in particular their apparent proximity to the position of the water-saturated solidus. Similarly, the conclusions of studies attempting to retrieve the pre-eruptive storage conditions of silicic magmas from Ti-in-zircon thermometry (Reid et al., 2011; Klemetti and Clynne, 2014; Barboni et al., 2016; Kaiser et al., 2017; Szymanowski et al., 2017) strongly depend on whether the model temperatures are accurate, especially when physical properties of magma (such as crystallinity) are inferred. While the activities of titania and silica remain major sources of uncertainty for such calculations, introducing an additional, potentially significant analytical bias should be avoided. For accurate titanium measurements, it is therefore recommended to standardise analyses to a primary zircon calibration material such as GZ7 or 91500.

4.6. Secondary calibration of additional zircon reference materials by LA-ICP-MS

Our newly-determined, accurate Ti concentrations for the proposed primary reference zircons 91500 and GZ7 enable a reassessment of the Ti contents of other commonly used zircons suitable for use as either secondary or primary reference materials. In the following experiment, we therefore analysed a range of zircon reference materials by LA-ICP-MS together with interspersed analyses of zircons 91500 and GZ7, using an identical analytical setup as for the homogeneity tests (section 4.3.1). The *in situ* determined Ti abundances were then assessed relative to the two proposed primary reference materials in order to derive suggested Ti concentration values for those additional reference samples (Table 4.2, Fig. 4.4). The analyses also allowed an independent verification of the consistency of the isotope dilution results presented above.

Table 4.2. Recalibrated Ti concentrations of zircon reference materials determined by LA-ICP-MS

Sample	Reference	Fragments	Analyses	relative to 91500			relative to GZ7			recommended value[a]	
				Ti [µg g^{-1}]	SD	RSD [%]	Ti [µg g^{-1}]	SD	RSD [%]	Ti [µg g^{-1}]	95 % CI[b]
primary reference materials											
91500	Wiedenbeck et al. (1995)	14	26				4.77	0.18	3.7	4.73	0.15
GZ7	Nasdala et al. (2018)	8	26	24.84	0.66	2.7				25.08	0.18
additional reference materials											
GJ-1 O	Jackson et al. (2004)	1	10	3.34	0.10	3.0	3.42	0.08	2.3		
GJ-1 A	Jackson et al. (2004)	1	10	3.55	0.13	3.7	3.55	0.12	3.5		
GJ-1 77	Jackson et al. (2004)	1	10	3.70	0.10	2.6	3.69	0.11	3.0		
GJ-1 all	Jackson et al. (2004)	3	30	3.53	0.18	5.2	3.55	0.15	4.2	3.55	0.06
Mud Tank dark[c]	Black and Gulson (1978)	1	10	4.27	1.44	34	4.33	1.45	34		
Mud Tank 1[c]	Black and Gulson (1978)	1	10	8.25	0.88	11	8.29	0.83	10		
Mud Tank 2[c]	Black and Gulson (1978)	10	10	7.61	0.79	10	7.70	0.76	10		
Mud Tank 1+2[c]	Black and Gulson (1978)	11	20	7.93	0.88	11	7.99	0.83	10	7.99	0.39
AusZ2	Kennedy et al. (2014)	1	10	2.19	0.10	4.5	2.20	0.08	3.8	2.20	0.06
AusZ5	Kennedy et al. (2014)	1	10	3.28	0.40	12	3.29	0.39	12	3.29	0.28
AusZ7-1	in-house reference material (ETH)	1	20	1.72	0.23	13	1.73	0.23	13	1.73	0.11
AusZ7-5	in-house reference material (ETH)	1	20	3.63	0.40	11	3.63	0.40	11	3.63	0.19
MAD-1	Barth and Wooden (2010)	5	20	16.96	0.57	3.3	17.08	0.34	2.0	17.08	0.20
MAD-559	Coble et al. (2018)	6	20	3.97	0.17	4.3	4.00	0.16	4.1	4.00	0.08
SL13	Claoué-Long et al. (1995)	1	15	6.32	0.22	3.5	6.30	0.19	3.0	6.30	0.11
CZ3	in-house reference material (Curtin)	2	10	4.83	0.10	2.1	4.87	0.09	1.9	4.87	0.08

[a] for primary reference materials, the recommended value is the ID value, for additional reference materials it is the mean LA–ICP–MS value relative to GZ7

[b] CI–confidence interval, including propagated uncertainty on the primary reference material GZ7

[c] analysed Mud Tank zircons included a single crystal from ETH ('1'), 10 crystals from Stanford University ('2') and a single anomalously dark crystal from ETH ('dark')

Analyses of GZ7 relative to 91500 ($n = 26$) yielded a mean Ti concentration of 24.84 ± 0.66 µg g^{-1} (1 SD) which agrees within uncertainty with the ID value of 25.08 ± 0.18 µg g^{-1} (Table 4.2). The reverse standardisation of 91500 relative to GZ7 returned a mean Ti concentration of 4.77 ± 0.18 µg g^{-1} (1 SD, $n = 26$) in 91500, a value fully consistent with 4.73 ± 0.15 µg g^{-1} derived from the isotope dilution measurements. The two ID values are therefore internally consistent which indicates that the two primary reference materials can be used interchangeably without compromising accuracy. However, whenever both zircons are available, GZ7 should be the preferred primary reference material, given its superior homogeneity and overall higher content of Ti compared to 91500. Due to the minor heterogeneity of 91500, when standardising to this zircon we recommend analysing multiple spots on multiple fragments to obtain a large sample set, so that the calculated mean captures the variation averaged by the whole-grain dissolution technique.

The assessment of other zircon reference materials included the samples presented in Table 4.2 and Fig. 4.4. The selected samples showed variable levels of inter- and intragrain homogeneity; all reference materials are reported with a recommended average Ti value evaluated relative to the isotope dilution value for zircon GZ7. For the purpose of deriving Ti concentrations, Si was used as internal standard assuming constant Si contents of all zircons. EPMA measurements of zircons suggest deviations in Si on the order of no more than 5% (e.g. Belousova et al., 2002) which in most cases can be considered a minor effect compared to inaccuracies due to matrix effects discussed here. Highest accuracy applications, however, may require direct EPMA measurements of major elements such as Si or Hf for internal standardisation of *in situ* analyses.

Three separate grains of zircon GJ-1 (Jackson et al., 2004) were found to have high levels of within-grain homogeneity in Ti (Table 4.2; Fig. 4.4); however, the variability between these grains should limit their use to secondary quality checks. The Mud Tank zircons (Black and Gulson, 1978) are highly heterogeneous in Ti content (typical light-coloured grains), additionally one grain was anomalously dark in colour and significantly depleted in Ti. From the selection of Australian zircons introduced by Kennedy et al. (2014) (AusZ2, AusZ5) and similar zircons from the same source routinely analysed at ETH (AusZ7-1, AusZ7-5), only AusZ2 showed Ti homogeneity comparable to that of the primary reference materials. Finally, other well-characterised zircons SL13 (Claoué-Long et al., 1995; Harrison and Schmitt, 2007), CZ3 (Ireland and Williams, 2003), MAD-1 (Madagascar green zircon; Barth and Wooden, 2010), and MAD-559 (Coble et al., 2018) all showed high degrees of homogeneity in Ti, which permits their potential application as reference materials for Ti-in-zircon thermometry.

In summary, our reassessment by LA-ICP-MS has identified five additional zircon samples sufficiently homogeneous in Ti to be used as reference materials. Their use may be either alongside one (or both) of GZ7, 91500 as primary reference, or, in the absence of either of the two, as primary calibration materials. In particular, zircons MAD-1 (with a high Ti of 17.08 µg g^{-1}), SL13, CZ3, and MAD-559 (all ≥ 4 µg g^{-1} Ti) are sufficiently

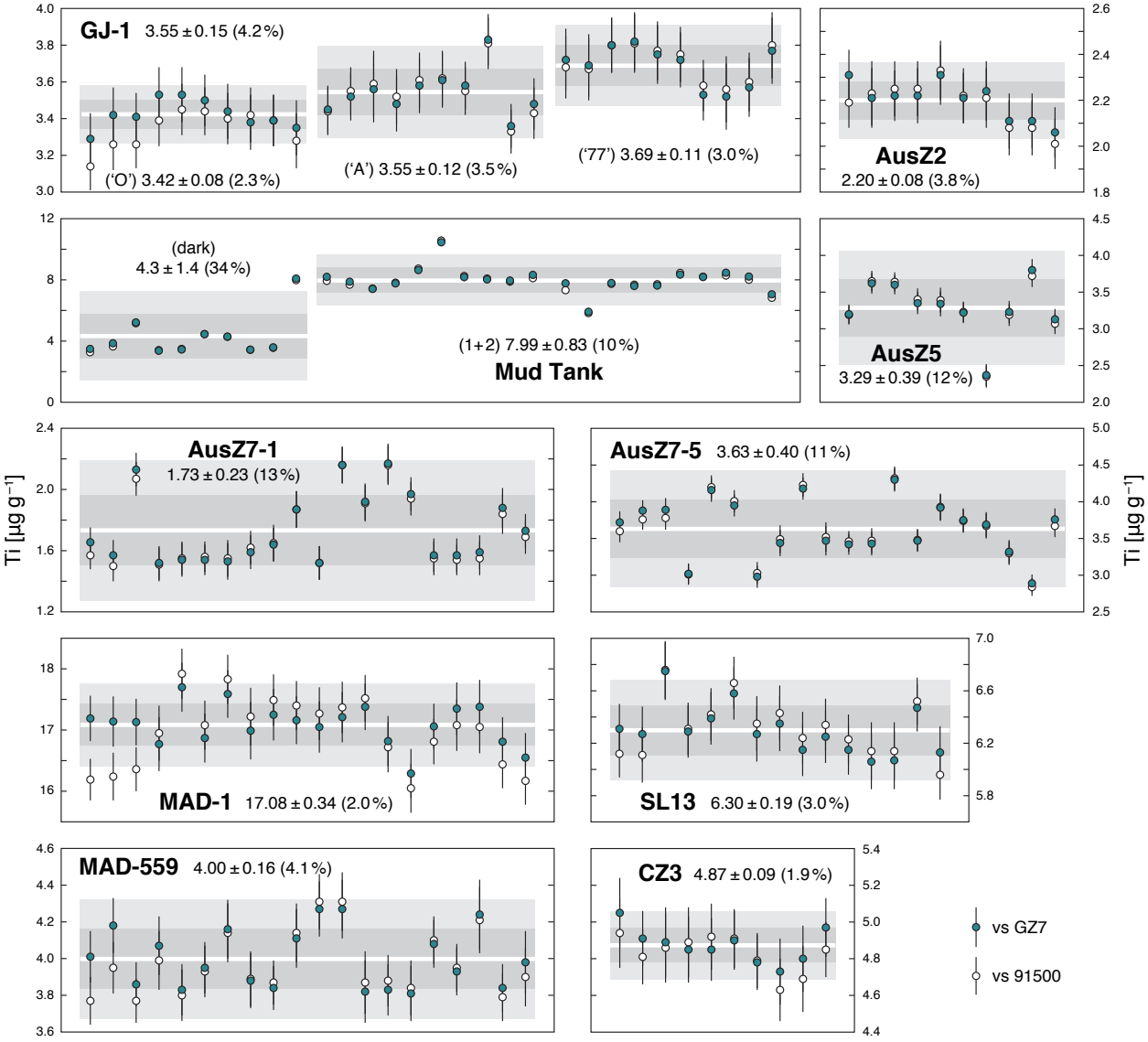

Figure 4.4. Results of the reassessment of Ti contents in zircon reference materials by LA-ICP-MS. Results both relative to zircon 91500 (white) and relative to zircon GZ7 (teal) are presented, with the mean value, 1 SD and 2 SD (grey backgrounds) shown for the preferred data relative to GZ7. 1 RSD is given in brackets. The difference between the two standardisations is a function of the relative placement of the reference materials in the analytical sequence (resulting in different drift corrections) as well as the differences in homogeneity between GZ7 and 91500. Note that in most cases using the more homogeneous primary reference material (GZ7) leads to decreased scatter of the results compared to using 91500 (Table 4.2).

rich in Ti to limit the amount of extrapolation and the related error magnification when applied as the primary reference material in evaluating most natural zircons. AusZ2 (2.20 µg g^{-1} Ti) is at the low end of natural Ti concentrations, and consequently suitable only as a quality-check reference material. All the recommended values presented in

Table 4.2 are directly anchored to the isotope dilution data for zircon GZ7, and as such create an internally consistent framework that ensures the accuracy of future determinations of Ti-in-zircon.

4.7. Conclusions and recommendations

This work shows the importance of using matrix-matched reference materials for *in situ* analyses of Ti in zircon using LA-ICP-MS or SIMS. Applying glass (i.e. 'matrix-mismatched') reference materials for such analyses can induce significant inaccuracy (as much as 30 % offset) biasing the calculated Ti concentrations and consequently model Ti-in-zircon temperatures. Therefore, to ensure the accuracy of the analytical input to temperature calculations, it is recommended to standardise these analyses to zircon reference materials rather than glass.

Two zircon reference materials of varied composition and levels of homogeneity, zircon 91500 and zircon GZ7, are proposed as primary reference materials for Ti. Independent isotope dilution (ID) determinations of Ti in multiple fragments of both zircons are presented and their consistency confirmed by LA-ICP-MS analyses. Additionally, a number of secondary zircon reference materials that encompass a range of compositions were analysed by LA-ICP-MS to reassess their Ti concentrations, now anchored to the newly obtained GZ7 ID value. The reassessment of secondary reference material Ti concentrations will permit comparisons of Ti-in-zircon datasets whenever such values are reported.

The efforts described here are aimed at creating a self-consistent datum of accurately measured Ti in zircon reference materials, ensuring the accuracy of the key input parameter to the increasingly popular Ti-in-zircon thermometry (Watson et al., 2006; Ferry and Watson, 2007). However, in order for the model temperatures to be significant, a robust model for the interpretation of zircon crystallisation conditions is fundamental. While the analytical improvements are an important step forward, it is crucial that more work is invested in refining the methods used to determine or model the applicable TiO_2 and SiO_2 activities in the chemical environment of zircon crystallisation, as well as the potential effect of pressure on Ti partitioning into zircon.

Acknowledgements

This work was supported by the Swiss National Science Foundation (grants 200021–155923 to OB and 200021–149282 to MS), the Austrian Science Fund (grant P244481-N19 to LN), and ETH Zürich (Postdoctoral Fellowship to JFW). Niel Williams is thanked for preparation and calibration of the Ti double spike and for Ti isotope analyses of magmatic reference samples. We thank Max Mandl for discussions on ICP-MS analyses of Ti and Michael Wiedenbeck for providing the 91500 zircon. LN is indebted to E. Gamini Zoysa and Bhuwadol Wanthanachaisaeng for assistance in the acquisition of the GZ7 gem specimen. Yue-Heng Yang and Sarah Gain are thanked for preliminary trace-ele-

ment analyses of zircon GZ7. James Darling, an anonymous reviewer, and editor Klaus Mezger are acknowledged for constructive comments on the manuscript.

Appendix

Supplementary information to this chapter can be found in Appendix C.

References

Arevalo, R.J., 2014. Laser Ablation ICP-MS and Laser Fluorination GS-MS. In: Holland, H.D., Turekian, K.K. (Eds.), Treatise on Geochemistry (Second Edition). Elsevier, Oxford, pp. 425–441.

Baldwin, J., Brown, M., Schmitz, M., 2007. First application of titanium-in-zircon thermometry to ultrahigh-temperature metamorphism. Geology 35, 295–298.

Barboni, M., Boehnke, P., Schmitt, A.K., Harrison, T.M., Shane, P., Bouvier, A.S., Baumgartner, L., 2016. Warm storage for arc magmas. Proc. Natl. Acad. Sci. USA 113, 13959–13964.

Barth, A.P., Tani, K., Meffre, S., Wooden, J.L., Coble, M.A., Arculus, R.J., Ishizuka, O., Shukle, J.T., 2017. Generation of silicic melts in the early Izu–Bonin arc recorded by detrital zircons in proximal arc volcaniclastic rocks from the Philippine Sea. Geochem. Geophys. Geosyst. 18, 3576–3591.

Barth, A.P., Wooden, J.L., 2010. Coupled elemental and isotopic analyses of polygenetic zircons from granitic rocks by ion microprobe, with implications for melt evolution and the sources of granitic magmas. Chem. Geol. 277, 149–159.

Belousova, E., Griffin, W., O'Reilly, S.Y., Fisher, N., 2002. Igneous zircon: trace element composition as an indicator of source rock type. Contrib. Mineral. Petrol. 143, 602–622.

Black, L.P., Gulson, B.L., 1978. The age of the Mud Tank carbonatite, Strangways Range, Northern Territory. BMR J. Aust. Geol. Geophys. 3, 227–232.

Bruand, E., Storey, C., Fowler, M., 2014. Accessory mineral chemistry of high Ba–Sr granites from northern Scotland: Constraints on petrogenesis and records of whole-rock signature. J. Petrol. 55, 1619–1651.

Cavosie, A.J., Valley, J.W., Kita, N.T., Spicuzza, M.J., Ushikubo, T., Wilde, S.A., 2011. The origin of high $\delta^{18}O$ zircons: marbles, megacrysts, and metamorphism. Contrib. Mineral. Petrol. 162, 961–974.

Claiborne, L.L., Miller, C.F., Wooden, J.L., 2010. Trace element composition of igneous zircon: a thermal and compositional record of the accumulation and evolution of a large silicic batholith, Spirit Mountain, Nevada. Contrib. Mineral. Petrol. 160, 511–531.

Claoué-Long, J.C., Compston, W., Roberts, J., Fanning, C.M., 1995. Two carboniferous ages: A comparison of SHRIMP zircon dating with conventional zircon ages and $^{40}Ar/^{39}Ar$ analysis. In: Berggren, W.A., Kent, D.V., Aubrey, M.P., Hardenbol, J. (Eds.), Geochronology Time Scales and Global Stratigraphic Correlation. Society for Sedimentary Geology Special Publication 54, Tulsa, OK, pp. 3–21.

Clark, C., Collins, A.S., Santosh, M., Taylor, R., Wade, B.P., 2009. The P-T-t architecture of a Gondwanan suture: REE, U–Pb and Ti-in-zircon thermometric constraints from the Palghat Cauvery shear system, South India. Precambrian Res. 174, 129–144.

Coble, M.A., Vazquez, J., Barth, A.P., Wooden, J., Burns, D., Kylander-Clark, A., Jackson, S., Vennari, C.E., 2018. Trace element characterisation of MAD-559 zircon reference material for ion microprobe analysis. Geostand. Geoanal. Res.

Coogan, L.A., Hinton, R.W., 2006. Do the trace element compositions of detrital zircons require Hadean continental crust? Geology 34, 633–636.

Darling, J., Storey, C., Hawkesworth, C., 2009. Impact melt sheet zircons and their implications for the Hadean crust. Geology 37, 927–930.

Durrant, S.F., 1999. Laser ablation inductively coupled plasma mass spectrometry: achievements, problems, prospects. J. Anal. At. Spectrom. 14, 1385–1403.

Ewing, T.A., Hermann, J., Rubatto, D., 2013. The robustness of the Zr-in-rutile and Ti-in-zircon thermometers during high-temperature metamorphism (Ivrea–Verbano Zone, northern Italy). Contrib. Mineral. Petrol. 165, 757–779.

Ferriss, E.D., Essene, E.J., Becker, U., 2008. Computational study of the effect of pressure on the Ti-in-zircon geothermometer. Eur. J. Mineral. 20, 745–755.

Ferry, J.M., Watson, E.B., 2007. New thermodynamic models and revised calibrations for the Ti-in-zircon and Zr-in-rutile thermometers. Contrib. Mineral. Petrol. 154, 429–437.

Fu, B., Page, F.Z., Cavosie, A.J., Fournelle, J., Kita, N.T., Lackey, J.S., Wilde, S.A., Valley, J.W., 2008. Ti-in-zircon thermometry: applications and limitations. Contrib. Mineral. Petrol. 156, 197–215.

Ghiorso, M.S., Gualda, G.A.R., 2013. A method for estimating the activity of titania in magmatic liquids from the compositions of coexisting rhombohedral and cubic iron-titanium oxides. Contrib. Mineral. Petrol. 165, 73–81.

Grimes, C.B., John, B.E., Cheadle, M.J., Mazdab, F.K., Wooden, J.L., Swapp, S., Schwartz, J.J., 2009. On the occurrence, trace element geochemistry, and crystallization history of zircon from in situ ocean lithosphere. Contrib. Mineral. Petrol. 158, 757–783.

Guillong, M., von Quadt, A., Sakata, S., Peytcheva, I., Bachmann, O., 2014. LA-ICP-MS Pb–U dating of young zircons from the Kos–Nisyros volcanic centre, SE Aegean arc. J. Anal. At. Spectrom. 29, 963–970.

Harrison, T.M., Schmitt, A.K., 2007. High sensitivity mapping of Ti distributions in Hadean zircons. Earth Planet. Sci. Lett. 261, 9–19.

Harrison, T.M., Watson, E.B., Aikman, A.B., 2007. Temperature spectra of zircon crystallization in plutonic rocks. Geology 35, 635–638.

Hayden, L.A., Watson, E.B., 2007. Rutile saturation in hydrous siliceous melts and its bearing on Ti-thermometry of quartz and zircon. Earth Planet. Sci. Lett. 258, 561–568.

Hiess, J., Nutman, A.P., Bennett, V.C., Holden, P., 2008. Ti-in-zircon thermometry applied to contrasting Archean metamorphic and igneous systems. Chem. Geol. 247, 323–338.

Hurley, P.M., 1954. The helium age method and the distribution and migration of helium in rocks. In: Faul, H. (Ed.), Nuclear geology. Wiley, New York, pp. 301–329.

Ickert, R.B., Williams, I.S., Wyborn, D., 2011. Ti in zircon from the Boggy Plain zoned pluton: implications for zircon petrology and Hadean tectonics. Contrib. Mineral. Petrol. 162, 447–461.

Ireland, T.R., 2014. Ion Microscopes and Microprobes. In: Holland, H.D., Turekian, K.K. (Eds.), Treatise on Geochemistry (Second Edition). Elsevier, Oxford, pp. 385–409.

Ireland, T.R., Williams, I.S., 2003. Considerations in zircon geochronology by SIMS. Rev. Mineral. Geochem. 53, 215–241.

Jackson, S.E., Pearson, N.J., Griffin, W.L., Belousova, E.A., 2004. The application of laser ablation-inductively coupled plasma-mass spectrometry to in situ U–Pb zircon geochronology. Chem. Geol. 211, 47–69.

Jochum, K., Stoll, B., Herwig, K., Willbold, M., 2007. Validation of LA-ICP-MS trace element analysis of geological glasses using a new solid-state 193 nm Nd: YAG laser and matrix-matched calibration. J. Anal. At. Spectrom. 22, 112–121.

Kaiser, J.F., de Silva, S., Schmitt, A.K., Economos, R., Sunagua, M., 2017. Million-year melt-presence in monotonous intermediate magma for a volcanic–plutonic assemblage in the Central Andes: Contrasting histories of crystal-rich and crystal-poor super-sized silicic magmas. Earth Planet. Sci. Lett. 457, 73–86.

Kennedy, A.K., Wotzlaw, J.F., Schaltegger, U., Crowley, J.L., Schmitz, M., 2014. Eocene zircon reference material for microanalysis of U–Th–Pb isotopes and trace elements. Can. Mineral. 52, 409–421.

Kenny, G.G., Whitehouse, M.J., Kamber, B.S., 2016. Differentiated impact melt sheets may be a potential source of Hadean detrital zircon. Geology 44, 435–438.

Klemetti, E.W., Clynne, M.A., 2014. Localized rejuvenation of a crystal mush recorded in zircon temporal and compositional variation at the Lassen Volcanic Center, northern California. PLoS ONE 9, e113157.

Krogh, T.E., 1973. A low-contamination method for hydrothermal decomposition of zircon and extraction of U and Pb for isotopic age determinations. Geochim. Cosmochim. Acta 37, 485–494.

Kröner, A., Kehelpannala, K.V.W., Kriegsman, L.M., 1994. Origin of compositional layering and mechanism of crustal thickening in the high-grade gneiss terrain of Sri Lanka. Precambrian Res. 66, 21–37.

Kularatne, K., Audétat, A., 2014. Rutile solubility in hydrous rhyolite melts at 750–900 °C and 2 kbar, with application to titanium-in-quartz

(TitaniQ) thermobarometry. Geochim. Cosmochim. Acta 125, 196–209.

Liu, Y., Gao, S., Hu, Z., Gao, C., Zong, K., Wang, D., 2010. Continental and oceanic crust recycling-induced melt–peridotite interactions in the Trans–North China Orogen: U–Pb dating, Hf isotopes and trace elements in zircons from mantle xenoliths. J. Petrol. 51, 537–571.

Matthews, N.E., Vazquez, J.A., Calvert, A.T., 2015. Age of the Lava Creek supereruption and magma chamber assembly at Yellowstone based on $^{40}Ar/^{39}Ar$ and U–Pb dating of sanidine and zircon crystals. Geochem. Geophys. Geosyst. 16, 2508–2528.

Nasdala, L., Corfu, F., Schoene, B., Tapster, S.R., Condon, D.J., Wall, C.J., Schmitz, M.D., Ovtcharova, M., Schaltegger, U., Kennedy, A.K., Kronz, A., Reiners, P.W., Yang, Y.H., Wu, F.Y., Gain, S.E.M., Griffin, W.L., Szymanowski, D., Chanmuang, C., Ende, M., Valley, J.W., Spicuzza, M.J., Wanthanachaisaeng, B., Giester, G., 2018. GZ7 and GZ8—two zircon reference materials for SIMS U–Pb geochronology. Geostand. Geoanal. Res.

Nasdala, L., Reiners, P.W., Garver, J.I., Kennedy, A.K., Stern, R.A., Balan, E., Wirth, R., 2004. Incomplete retention of radiation damage in zircon from Sri Lanka. Am. Mineral. 89, 219–231.

Page, F.Z., Fu, B., Kita, N.T., Fournelle, J., Spicuzza, M.J., Schulze, D.J., Viljoen, F., Basei, M.A.S., Valley, J.W., 2007. Zircons from kimberlite: New insights from oxygen isotopes, trace elements, and Ti in zircon thermometry. Geochim. Cosmochim. Acta 71, 3887–3903.

Reid, M.R., Vazquez, J.A., Schmitt, A.K., 2011. Zircon-scale insights into the history of a Supervolcano, Bishop Tuff, Long Valley, California, with implications for the Ti-in-zircon geothermometer. Contrib. Mineral. Petrol. 161, 293–311.

Rivera, T.A., Schmitz, M.D., Jicha, B.R., Crowley, J.L., 2016. Zircon petrochronology and $^{40}Ar/^{39}Ar$ sanidine dates for the Mesa Falls Tuff: Crystal-scale records of magmatic evolution and the short lifespan of a large Yellowstone magma chamber. J. Petrol. 57, 1677–1704.

Schmitt, A.K., Konrad, K., Andrews, G.D.M., Horie, K., Brown, S.R., Koppers, A.A.P., Pecha, M., Busby, C.J., Tamura, Y., 2017. $^{40}Ar/^{39}Ar$ ages and zircon petrochronology for the rear arc of the Izu-Bonin-Marianas intra-oceanic subduction zone. Int. Geol. Rev. 60, 956–976.

Schmitt, A.K., Vazquez, J.A., 2006. Alteration and remelting of nascent oceanic crust during continental rupture: Evidence from zircon geochemistry of rhyolites and xenoliths from the Salton Trough, California. Earth Planet. Sci. Lett. 252, 260–274.

Shimizu, N., Hart, S.R., 1982. Applications of the ion micro-probe to geochemistry and cosmochemistry. Annu. Rev. Earth Planet. Sci. 10, 483–526.

Szymanowski, D., Wotzlaw, J.F., Ellis, B.S., Bachmann, O., Guillong, M., von Quadt, A., 2017. Protracted near-solidus storage and pre-eruptive rejuvenation of large magma reservoirs. Nat. Geosci. 10, 777–782.

Trail, D., Mojzsis, S.J., Harrison, T.M., Schmitt, A.K., Watson, E.B., Young, E.D., 2007. Constraints on Hadean zircon protoliths from oxygen isotopes, Ti-thermometry, and rare earth elements. Geochem. Geophys. Geosyst. 8, Q06014.

Wark, D.A., Hildreth, W., Spear, F.S., Cherniak, D.J., Watson, E.B., 2007. Pre-eruption recharge of the Bishop magma system. Geology 35, 235–238.

Watson, E.B., Harrison, T.M., 2005. Zircon thermometer reveals minimum melting conditions on earliest Earth. Science 308, 841–844.

Watson, E.B., Wark, D.A., Thomas, J.B., 2006. Crystallization thermometers for zircon and rutile. Contrib. Mineral. Petrol. 151, 413–433.

Wiedenbeck, M., Allé, P., Corfu, F., Griffin, W., Meier, M., Oberli, F., von Quadt, A., Roddick, J., Spiegel, W., 1995. Three natural zircon standards for U–Th–Pb, Lu–Hf, trace element and REE analyses. Geostand. Newsl. 19, 1–23.

Wiedenbeck, M., Hanchar, J.M., Peck, W.H., Sylvester, P., Valley, J., Whitehouse, M., Kronz, A., Morishita, Y., Nasdala, L., Fiebig, J., Franchi, I., Girard, J.P., Greenwood, R.C., Hinton, R., Kita, N., Mason, P.R.D., Norman, M., Ogasawara, M., Piccoli, R., Rhede, D., Satoh, H., Schulz-Dobrick, B., Skar, O., Spicuzza, M.J., Terada, K., Tindle, A., Togashi, S., Vennemann, T., Xie, Q., Zheng, Y.F., 2004. Further characterisation of the 91500 zircon crystal. Geostand. Geoanal. Res. 28, 9–39.

Williams, N.H., 2014. Titanium isotope cosmochemistry. PhD Thesis, University of Manchester.

Williams, N.H., Schönbächler, M., Fehr, M.A., Akram, W.M., Parkinson, I.J., 2014. Different heterogeneously distributed titanium isotope components in solar system materials and mass-dependent titanium isotope variations. Lunar Planet. Sci. Conf. 45, 2183.

Yuan, H., Gao, S., Liu, X., Li, H., Günther, D., Wu, F., 2004. Accurate U–Pb age and trace element determinations of zircon by laser ablation-inductively coupled plasma-mass spectrometry. Geostand. Geoanal. Res. 28, 353–370.

Zoysa, G., 2014. The geology and gem deposits of Sri Lanka. InColor 27, 38–41.

Chapter 5

Summary and outlook

5.1. The accessory-mineral perspective

The main goal of the research presented in this thesis was to contribute a new perspective to the debate about the modes and timescales of storage of evolved magma in the upper crust. The particular focus was on looking through the lens of two accessory minerals found within volcanic deposits, zircon and titanite, and taking advantage of their exceptional ability to record both their crystallisation conditions and the time of crystallisation. The idea of using accessory minerals (particularly zircon) in this way is not new in itself, and has been applied with success in many settings, using both *in situ* (e.g. Vazquez and Reid, 2004; Rivera et al., 2014; Barboni et al., 2016; Kaiser et al., 2017; Reid and Vazquez, 2017) and bulk-grain compositional data (e.g. Schoene et al., 2012; Wotzlaw et al., 2013; Samperton et al., 2015). However, the particular combination of high-precision zircon and titanite geochronology, trace-element geochemistry and texturally-constrained sampling provided interesting new insights into the behaviour of magmas in the Kneeling Nun system and, by extension, other evolved, upper-crustal magmatic reservoirs feeding large volcanic eruptions. Below, I review the main findings presented in this thesis, focussing on the geological implications of the Kneeling Nun Tuff study (Chapters 1–3). The analytical developments relevant to Ti-in-zircon thermometry presented in Chapter 4 are important for the practice of obtaining accurate Ti contents of unknown zircons, but in my view do not require further discussion here.

The first striking result of this work is the full range of bulk-grain U–Pb crystallisation ages of both zircon and titanite found within the Kneeling Nun Tuff magma. The total U–Pb age range reaches 618 ± 56 ky for zircon in the mixed, bulk ignimbrite sample (Chapter 2), 771 ± 30 ky if all strictly juvenile material is considered, and as much as 1.6 My from the oldest intrusion represented in the lithic fraction (Chapter 3). This range exceeds most of those found so far in individual eruptive units (e.g. Reid et al., 1997; Brown and Fletcher, 1999; Vazquez and Reid, 2004; Charlier et al., 2005; Claiborne et al., 2010; Wotzlaw et al., 2013) but is comparable to some of the million-year timescales reported

very recently (Tierney et al., 2016; Kaiser et al., 2017; Reid and Vazquez, 2017). Such results on zircon crystals isolated from their host rocks are often contested with respect to their autocrystic, antecrystic, or xenocrystic character, i.e. it proves notoriously difficult to know whether a zircon crystal or its zone represents the main magmatic episode or whether it is recycled from an early growth period or an elusive precursor magmatic rock (Miller et al., 2007; Reid, 2008; Reid and Vazquez, 2017). In the case of bulk-grain analyses (e.g. by ID–TIMS), one also has to consider possible age mixing between younger outside zones and potentially much older cores, which might artificially expand the apparent timescale beyond what is expected from a coherently developing magma reservoir. In the interest of identifying inheritance, in this study we carefully characterised all zircons selected for high-precision dating with cathodoluminescence imaging, trace-element analyses and pre-screening *in situ* U–Pb dating. While the screening does not eliminate the possibility of including significantly older domains into the analysed crystal volume, this approach remains at the limit of practical application to zircon studies. Thus, the application of such precautions, as well as the fact that different lithologies reproduce similar zircon crystallisation age spectra (Chapter 3), lends some confidence to the zircon selection and the resulting U–Pb timescales. The zircon dates themselves inform about timescales of multiple related processes: the minimum construction time of the upper-crustal magmatic system (1.6 My from the first intrusion), the maturation time of the ultimately eruptible part of that reservoir (> 700 ky, all juvenile material) or the timescale of mush rejuvenation (~100 ky). Given that the Kneeling Nun Tuff formed as a result of a particularly voluminous eruption and may not be entirely representative of smaller systems, the relationship between the timescales of magma reservoir processes and their size might be worth exploring further.

By sampling different domains of the magma reservoir (lithologically constrained sampling), we could gain insight into the KNT reservoir structure, the relationships between its mobile and eruptible, and immobile parts (e.g. the granitic lithic clasts), as well as the timescales over which they develop. Only one of the lithic clasts characterised and sampled for zircon geochronology was distinguishably older than most of the erupted material. All other samples appeared cogenetic and showed compositional affinity, while their zircon age distributions were essentially indistinguishable. The only notable difference was in their final cooling age and the cooling path represented in the variable textures. These observations imply that for most of the KNT reservoir's lifetime, either (1) the magma was well mixed, thereby efficiently redistributing the zircon cargo, or (2) the reservoir was capable of crystallising zircon over a broad range of conditions, which resulted in apparently continuous zircon crystallisation over at least 700 ky, irrespectively of the location within the system. Given the differences in major mineral phase compositions are slight and easily re-equilibrated, proving one or the other remains a challenge.

One advantage of studying accessory minerals is their limited re-equilibration at magmatic conditions, which allowed us to trace the evolution of the conditions within the magma reservoir over time. We documented highly scattered zircon compositions that do not systematically vary over time (with the exception of the last 100 ky). Furthermore, at any given time, zircons of multiple, highly variable compositions apparently co-existed. The main implication is that within the KNT magma reservoir, and presumably other high-crystallinity magmatic systems, the conditions of magma storage are highly variable in both space and time. It follows that the 'degree of magmatic evolution', understood e.g. as position of the melt composition along a liquid line of descent, is independent of time. The common misconception equating the two may be sourced from a liquid-dominated model of a magma chamber and is only applicable to small, unidirectionally cooling magma bodies. In a model where the magma is crystal-dominated, the response of the system to changing conditions (mostly variations in heat input) is non-uniform and occurs at different rates depending on the location, giving rise to multiple co-existing melt compositions. We could use zircon trace elements to model the variable conditions across the whole magma reservoir as a function of co-crystallising mineral phases. The trace-element variations can be understood in terms of crystallinity (assuming that the mineral assemblage and the trace-element partitioning is known well) and crystallisation temperature (via the Ti-in-zircon thermometer). However, these parameters refer to the time and conditions of zircon crystallisation, which might give an idea of the range of conditions achieved in the reservoir, but tells us little about the subsequent magmatic storage.

In order to constrain the storage conditions of the KNT magma, we developed an approach utilising titanite geochemistry and geochronology (Chapter 2). A well-calibrated geothermometer for this accessory phase (Hayden et al., 2008) returned a narrow range of crystallisation temperatures (~710–740 °C) which suggested that in the KNT magma titanite was not stable above that temperature. By showing that, similarly to zircon, there is a prolonged timescale of titanite crystallisation, we could then constrain the temperature of magma storage to within the field of titanite stability. Importantly, this estimate of storage temperature represents the dominant conditions in the magma reservoir—but may not be applicable to the whole volume of magma and all 'time slices'. The mush model requires that the system is kept at magmatic temperatures by intermittent recharge supplying heat and resulting in positive temperature excursions, but the imprint of those events may be spatially restricted. The particular titanites analysed in this study must have been stored mostly at temperatures < ca. 730 °C as they did not fully dissolve and their U–Pb isotope ratios did not get (fully) reset. It is a reasonable supposition that these crystals represent typical KNT storage conditions, but the possibility that the older crystals analysed here are sampled from particularly low-T domains of the system cannot be discounted.

Using an approach complementary to exploiting titanite to constrain the first-order magma storage temperature, we created a precise, time-resolved record for the KNT reservoir based on zircon compositions. This work was made possible primarily by recent analytical developments in ID-TIMS U–Pb geochronology (reduced sample size, routine characterisation prior to dissolution) and the particular age, size and compositions of KNT zircon crystals. Using high-precision geochronology to generate this compositional record limits the uncertainty common to similar *in situ* zircon geochronology studies (Kent and Cooper, 2017). Additionally, new approaches to approximate the temperature-dependent partitioning of trace elements into zircon (e.g. Claiborne et al., 2018) let us speculate about the composition and nature of the melts involved in their crystallisation. The most important finding from this part (Chapter 3) is the recognition of a focussing compositional trend occurring prior to the Kneeling Nun Tuff eruption. To my knowledge, there have only been a few studies that could show such a trend while placing it in absolute time (Wotzlaw et al., 2013; Matthews et al., 2015; Barboni et al., 2016). With our data we could show that the gradual compositional changes developed over ~100 ky prior to eruption. While it is doubtful that this process was responsible for triggering the eruption, it appears that we were able to observe a prolonged period of priming, a transition of the highly crystalline magma reservoir to eruptible state through reduction of crystallinity (unlocking). Combining the zircon data with the relatively well-constrained behaviour of titanite in the system, we could see a probable increase in temperature (increase in Ti in zircon) and a partial transition to titanite-undersaturated melts prior to eruption. The preservation of abundant titanite in all erupted products shows that titanite was not quantitatively dissolved, so the average reservoir temperature upon eruption must have been still very close to the titanite saturation temperature. The mild increase in temperature upon rejuvenation is in perfect agreement with both observations from other systems (e.g. Bachmann and Dungan, 2002) and models showing that in wet, near-solidus mushes large amounts of melting required for unlocking can occur near-isothermally (e.g. Spera and Bohrson, 2018).

5.2. Open questions

The results for the Kneeling Nun Tuff summarised here provide new insights into the details of silicic magma evolution in the upper crust, particularly the timescales of magma reservoir construction, maturation, and rejuvenation prior to one of the largest eruptions so far recognised in the geological record. However, a number of aspects, of both technical and geological nature, remain open and could benefit from further study or future development:

- A better understanding of the behaviour of titanite in evolved magmatic systems. In this thesis we attempted to date titanite to the highest precision and accuracy possible, but the time-intensive nature of these analyses limited the size of the dataset. The *in situ* measured trace elements (particularly the temperature-dependent Zr contents) were very coherent across the magma reservoir, which constrains the

titanite stability well, but an expanded geochronological survey might be necessary to prove that the preservation of 'old' titanite is a universal feature that is not restricted to low-temperature storage domains.

- Approaches to integrate bulk-grain and *in situ* compositional information from accessory phases in a more meaningful way. This problem is particularly clear for zircon, where bulk-grain ID-TIMS guarantees by far the best age precision for samples older than ~ Quaternary, but solution trace element determinations on the same analytical volume (TIMS-TEA of Schoene et al., 2010) may limit the amount of useful information otherwise recovered from compositional zoning. Additionally, studies using TIMS-TEA have been so far incapable of analysing Ti. *In situ* (SIMS or LA-ICPMS) analyses can recover much more of the mineral's crystallisation history, but it is challenging to relate zone/spot compositions to exact crystallisation age. A model for deconvolving the time information for each spot composition as a function of core–rim volumetric proportions, ages, U contents etc. may provide some informative results, though it is likely to result in very large uncertainties.

- The partitioning of trace elements in magmatic systems. Well-constrained behaviour of elements is key to interpreting any mineral compositions one might measure. For the purpose of reconstructing an absolute chronology of events in a magma body, it is particularly important to constrain the mechanisms of element exchange between melt and accessory phases such as zircon. For example, the recent attempt to constrain the key effect of temperature on trace element partitioning used in Chapter 3 (Claiborne et al., 2018) is a useful first-order approximation. However, ultimately, the goal should be a coherent set of experimentally obtained, temperature-dependent partition coefficients.

- More studies on conditions and timescales of accessory mineral crystallisation in magmatic systems, building a database suitable for statistical analysis. Of particular importance is the resolution of the dichotomy between (zircon) crystallisation timescales of subduction-related and intraplate systems, and the relationship between these apparent accessory mineral timescales and the true system lifetimes.

- Integration of geochronological results with diffusion-related timescales. To get a fuller picture of magma storage within single magma bodies, it is important to use all chronological information available in the geochemical toolbox. For an eruption such as the KNT, one could obtain additional constraints on magma storage conditions by focussing on mineral phases that show abrupt compositional breaks. Two suitable candidates in the KNT would be (1) sanidine, which commonly features one or more rims enriched in Ba, Sr and other compatible trace elements (Fig. 3.3), or (2) titanite, with REE-enriched rims (Fig. 2.1b).

- Direct or indirect dating of individual crystals of major mineral phases, particularly combined with intra-crystal diffusion modelling. While currently high detection limits restrict U–series disequilibrium dating of major phases to large mineral separates, it is conceivable that future analytical techniques might allow to directly date single crystals of e.g. feldspars. This would allow interpretations similar to those for accessory phases, and remove much of the difficulty of interpreting bulk mineral separate U-series data. Alternatively, for older systems outside the disequilibrium range, zircon inclusions in crystals of a major phase could be dated with enough precision to constrain their growth timelines (e.g. Barboni and Schoene, 2014).

- Relationships between magmatic system sizes and timescales. As more and more geochronological and diffusion chronometry data are gathered by the community, for a better understanding of active systems it might be worthwhile to explore whether the time it takes for processes (such as magma accumulation, recharge, mush rejuvenation etc.) to occur scales with their size or whether it is largely universal and independent of system volume.

References

Bachmann, O., Dungan, M.A., 2002. Temperature-induced Al-zoning in hornblendes of the Fish Canyon magma, Colorado. Am. Mineral. 87, 1062–1076.

Barboni, M., Boehnke, P., Schmitt, A.K., Harrison, T.M., Shane, P., Bouvier, A.S., Baumgartner, L., 2016. Warm storage for arc magmas. Proc. Natl. Acad. Sci. USA 113, 13959–13964.

Barboni, M., Schoene, B., 2014. Short eruption window revealed by absolute crystal growth rates in a granitic magma. Nat. Geosci. 7, 524–528.

Brown, S.J.A., Fletcher, I.R., 1999. SHRIMP U-Pb dating of the preeruption growth history of zircons from the 340 ka Whakamaru Ignimbrite, New Zealand: Evidence for >250 k.y. magma residence times. Geology 27, 1035–1038.

Charlier, B., Wilson, C., Lowenstern, J., Blake, S., Van Calsteren, P., Davidson, J., 2005. Magma generation at a large, hyperactive silicic volcano (Taupo, New Zealand) revealed by U–Th and U–Pb systematics in zircons. J. Petrol. 46, 3–32.

Claiborne, L.L., Miller, C.F., Flanagan, D.M., Clynne, M.A., Wooden, J.L., 2010. Zircon reveals protracted magma storage and recycling beneath Mount St. Helens. Geology 38, 1011–1014.

Claiborne, L.L., Miller, C.F., Gualda, G.A., Carley, T.L., Covey, A.K., Wooden, J.L., Fleming, M.A., 2018. Zircon as magma monitor: robust, temperature-dependent partition coefficients from glass and zircon surface and rim measurements from natural systems, in: Moser, D.E., Corfu, F., Darling, J.R., Reddy, S.M., Tait, K. (Eds.), Microstructural Geochronology: Planetary Records Down to Atom Scale, Geophysical Monograph 232.

Hayden, L.A., Watson, E.B., Wark, D.A., 2008. A thermobarometer for sphene (titanite). Contrib. Mineral. Petrol. 155, 529–540.

Kaiser, J.F., de Silva, S., Schmitt, A.K., Economos, R., Sunagua, M., 2017. Million-year melt–presence in monotonous intermediate magma for a volcanic–plutonic assemblage in the Central Andes: Contrasting histories of crystal-rich and crystal-poor super-sized silicic magmas. Earth Planet. Sci. Lett. 457, 73–86.

Kent, A.J.R., Cooper, K.M., 2017. How well do zircons record the thermal evolution of magmatic systems? Geology 46, 111–114.

Matthews, N.E., Vazquez, J.A., Calvert, A.T., 2015. Age of the Lava Creek supereruption and magma chamber assembly at Yellowstone based on $^{40}Ar/^{39}Ar$ and U–Pb dating of sanidine and zircon crystals. Geochem. Geophys. Geosyst. 16, 2508–2528.

Miller, J.S., Matzel, J.E., Miller, C.F., Burgess, S.D., Miller, R.B., 2007. Zircon growth and recycling during the assembly of large, composite arc plutons. J. Volcanol. Geoth. Res. 167, 282–299.

Reid, M.R., 2008. How long does it take to supersize an eruption? Elements 4, 23–28.

Reid, M.R., Coath, C.D., Harrison, T.M., McKeegan, K.D., 1997. Prolonged residence times for the youngest rhyolites associated with Long Valley Caldera: $^{230}Th–^{238}U$ ion microprobe dating of young zircons. Earth Planet. Sci. Lett. 150, 27–39.

Reid, M.R., Vazquez, J.A., 2017. Fitful and protracted magma assembly leading to a giant eruption, Youngest Toba Tuff, Indonesia. Geochem. Geophys. Geosyst. 18, 156–177.

Rivera, T.A., Schmitz, M.D., Crowley, J.L., Storey, M., 2014. Rapid magma evolution constrained by zircon petrochronology and $^{40}Ar/^{39}Ar$ sanidine ages for the Huckleberry Ridge Tuff, Yellowstone, USA. Geology 42, 643–646.

Samperton, K.M., Schoene, B., Cottle, J.M., Keller, C.B., Crowley, J.L., Schmitz, M.D., 2015. Magma emplacement, differentiation and cooling in the middle crust: Integrated zircon geochronological–geochemical constraints from the Bergell Intrusion, Central Alps. Chem. Geol. 417, 322–340.

Schoene, B., Latkoczy, C., Schaltegger, U., Günther, D., 2010. A new method integrating high-precision U–Pb geochronology with zircon trace element analysis (U–Pb TIMS-TEA). Geochim. Cosmochim. Acta 74, 7144–7159.

Schoene, B., Schaltegger, U., Brack, P., Latkoczy, C., Stracke, A., Günther, D., 2012. Rates of magma differentiation and emplacement in a ballooning pluton recorded by U–Pb TIMS-TEA, Adamello batholith, Italy. Earth Planet. Sci. Lett. 355–356, 162–173.

Spera, F.J., Bohrson, W.A., 2018. Rejuvenation of crustal magma mush: A tale of multiply nested processes and timescales. Am. J. Sci. 318, 90–140.

Tierney, C.R., Schmitt, A.K., Lovera, O.M., de Silva, S.L., 2016. Voluminous plutonism during

volcanic quiescence revealed by thermochemical modeling of zircon. Geology 44, 683–686.
Vazquez, J.A., Reid, M.R., 2004. Probing the accumulation history of the voluminous Toba magma. Science 305, 991–994.
Wotzlaw, J.F., Schaltegger, U., Frick, D.A., Dungan, M.A., Gerdes, A., Günther, D., 2013. Tracking the evolution of large-volume silicic magma reservoirs from assembly to supereruption. Geology 41, 867–870.

Acknowledgements

First and foremost, I would like to thank Ben Ellis for absolutely brilliant supervision over the course of the PhD and the preceding Masters at ETH. Ben came up with the initial idea of this project and made it happen in the best style I can imagine. He agreed to take me on when I walked into his office with a satchel 6 years ago, with little idea about volcanic rocks and not really sure what he was saying to me… A few years of work together, many weeks in the field and one rodeo burger later, I can say I've learned a lot! Who knows where I would be now if it wasn't for Ben?

I am also extremely grateful to Olivier Bachmann for his open-door policy and support given to any ideas I had over the course of these last years. Even though since coming to ETH Olivier has grown increasingly busy (those classes in German!), he was always there to provide the big-picture thinking we as PhD students needed. The working environment of the Bachmann group is something fantastic, and I could not imagine doing this job anywhere else.

A big 'thank you' to Jörn Wotzlaw who taught me most of what I know about geochronology, and provided the technical expertise essential to the success of the project. This cake-loving character was an infinite source of ideas, some of which critically influenced the direction in which this study ultimately went.

I also want to thank other collaborators and colleagues at ETH who I worked with directly, particularly Marcel Guillong, Manuela Fehr, Yannick Buret and Albrecht von Quadt, who helped with or ran many of the analyses and were particularly open to trying new analytical approaches. Thank you: Yannick, Jörn, Simon, Özge and Julian for the good work in the clean lab, and that together we managed to keep it going all this time…

I am grateful to external collaborators involved in the work presented here, particularly Lutz Nasdala and Matt Coble, for providing crucial materials and data.

I'd also like to thank all the great people I met at ETH for an unforgettable experience the last few years. Particularly Jule and Jakub, with whom I shared the complete ETH adventure, from my first to (it would seem) the last day, but also an array of other characters: Nico, Anna, Maren, Yannick, Annina, Özge, Julia, Razvan, Matthias, Simon, Max, Giuliano, Kati, Sebbo, Alina, Natalia, Iris, Julien, Julian, Caro, Lotta, Stephane, Vanni, Fabio, Andrea, Wim, Ingrid, Michael…

I want to thank Francesca for her patience and endless support during the PhD. For the amount of complaining you had to endure, you should be an author on all the papers!

Finally, a big 'thank you' to my parents who have always unconditionally supported my every step, no matter how far I wanted to go.

Appendix A

Protracted near-solidus storage and pre-eruptive rejuvenation of large magma reservoirs

D. Szymanowski, J. F. Wotzlaw, B. S. Ellis, O. Bachmann, M. Guillong, A. von Quadt

SUPPLEMENTARY MATERIAL

Sample description

The Kneeling Nun Tuff (KNT) sample DS 1402 was collected from the KNT type area south of Santa Rita, New Mexico (32.7269° N 108.1181° W) (Fig. 2.1). It was sampled from the proximal outflow ignimbrite sheet, in this area between 60–100 m thick and ranging in crystallinity between 25–60 % (Elston. 1957; Giles, 1965, 1968). The sampled KNT facies is intensely welded and devitrified, with variably abundant cm-scale fiamme. The crystallinity of the sample was assessed by compositional mapping of a thin section performed with a Thermo Scientific NORAN System 7 EDS on a JEOL JSM-6390 LA scanning electron microscope at ETH Zürich, followed by analysis with the iSpectra toolbox (Liebske, 2015) allowing us to create a mineral phase map of a thin section (Fig. A1). The mapping identified a crystallinity of ~34 area % with plagioclase, sanidine, quartz, biotite, amphibole, magnetite + ilmenite (in order of decreasing abundance). For the purpose of trace element modelling (Fig. 2.2b) the area (~volume) proportions of minerals were converted to mass fractions. The abundances of zircon (0.04 wt.%) and titanite (0.3 wt.%) were approximated based on Zr (zircon) and Nd, Y (titanite) mass balance constraints.

References

Elston, W.E., 1957. Geology and mineral resources of Dwyer quadrangle, Grant, Luna, and Sierra Counties, New Mexico. N.M. Bur. Mines Miner. Res. Bull. 38.

Giles, D., 1965. Some aspects of the Kneeling Nun rhyolite tuff, in: Fitzsimmons, J.P., Balk, C.L. (Eds.), N.M. Geol. Soc. 16th Fall Field Conf. Guidebook, pp. 164–166.

Giles, D.L., 1968. Ash-flow tuffs of the Cobre Mountains, in: Titley, S.R. (Ed.), Arizona Geological Society Southern Arizona Guidebook III, pp. 289–291.

Liebske, C., 2015. iSpectra: An open source toolbox for the analysis of spectral images recorded on scanning electron microscopes. Microsc. Microanal. 21, 1006–1016 .

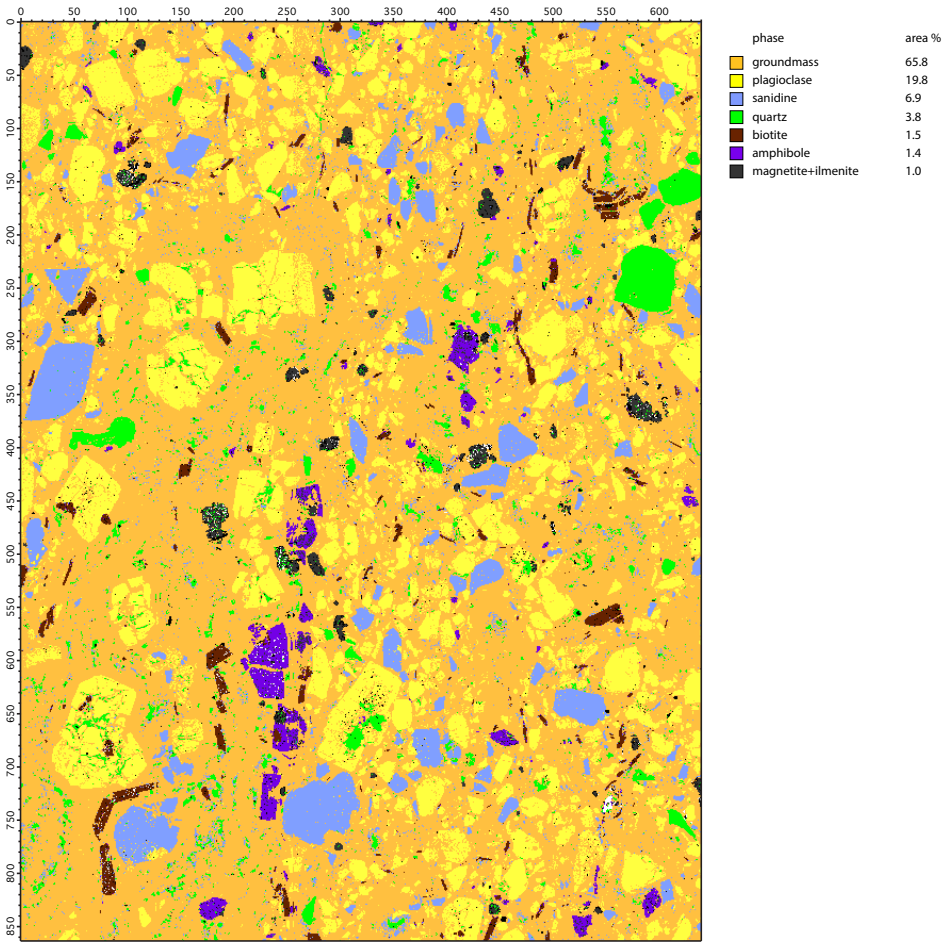

Fig. A1. Results of phase classification with the iSpectra toolbox.

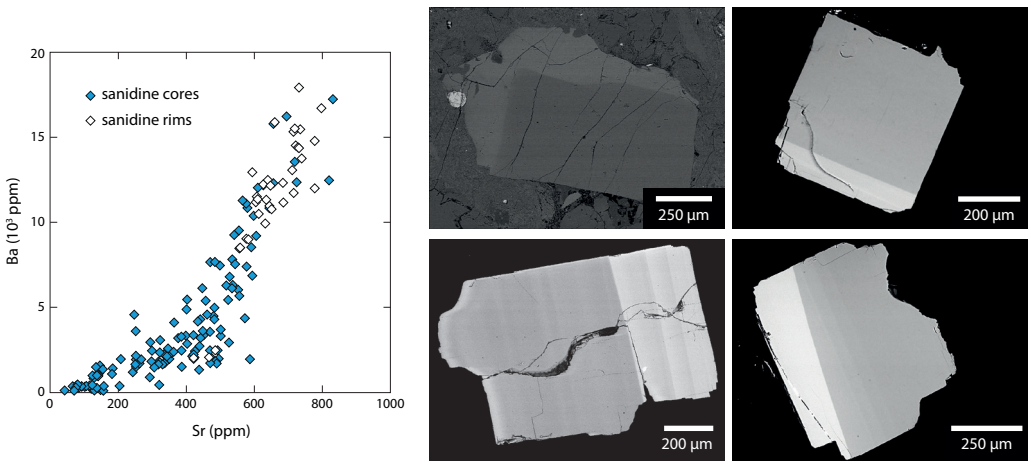

Fig. A2. Textures and compositions of Kneeling Nun Tuff sanidine illustrating the common presence of high-Ba rims (also enriched in Sr, Ti, P, and REE) crystallising from an enriched melt.

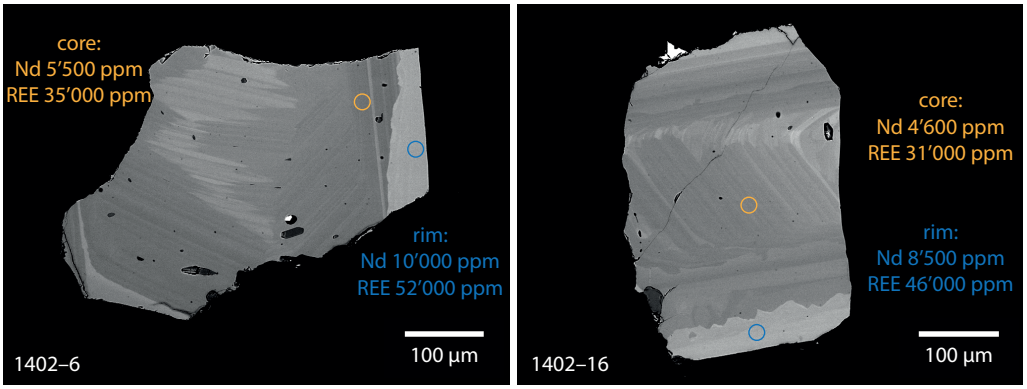

Fig. A3. Textures and compositions of Kneeling Nun Tuff titanite illustrating the common presence of high-REE rims (also enriched in Sr, Ba, Zr) crystallising from an enriched melt.

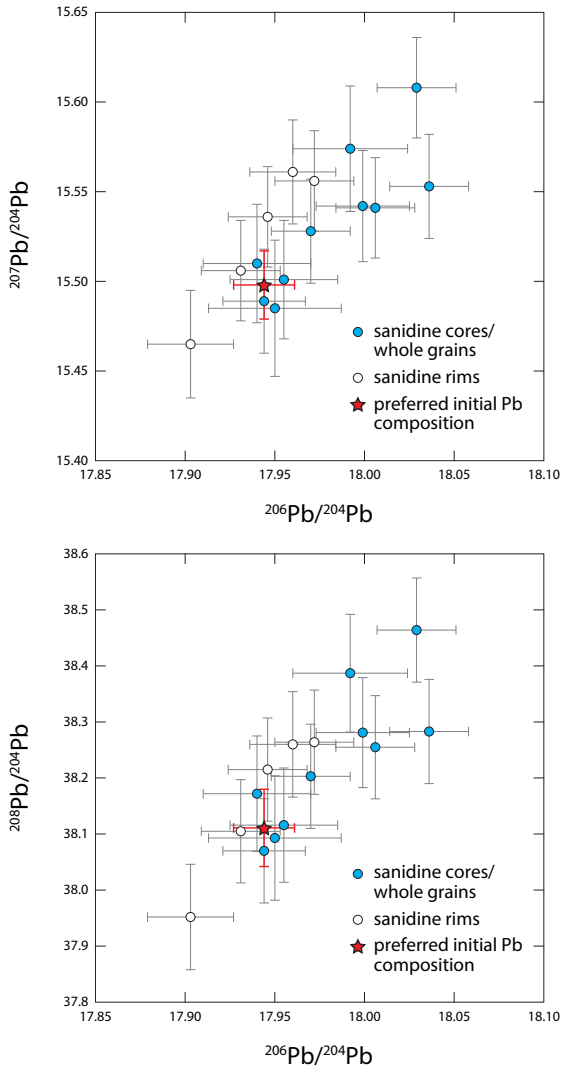

Fig. A4. Pb isotopic compositions of sanidine cores and rims measured by TIMS and the preferred initial Pb composition used for calculation of titanite U–Pb dates.

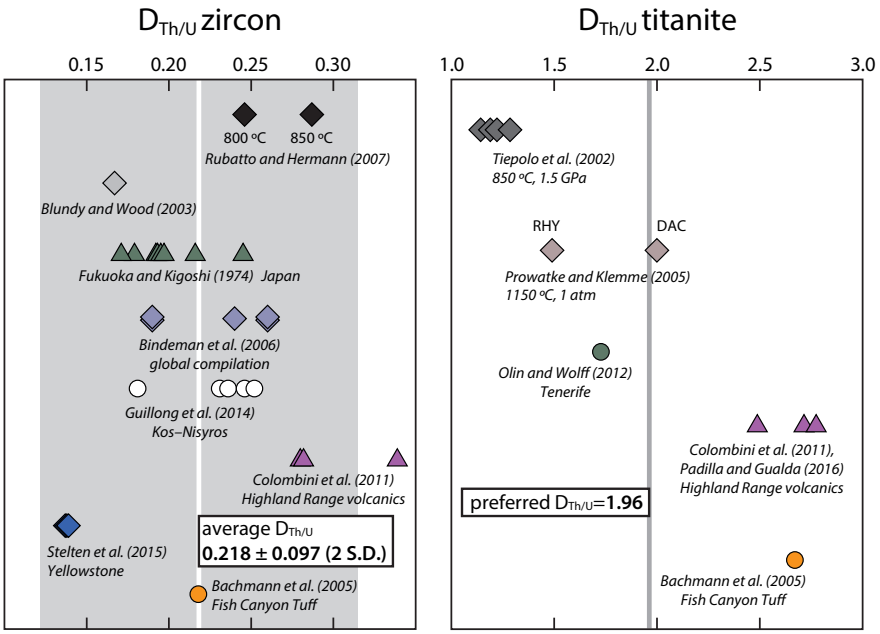

Fig. A5. Th–U partition coefficients used for the initial ^{230}Th disequilibrium correction of zircon and titanite U–Pb dates. For references see Chapter 2.

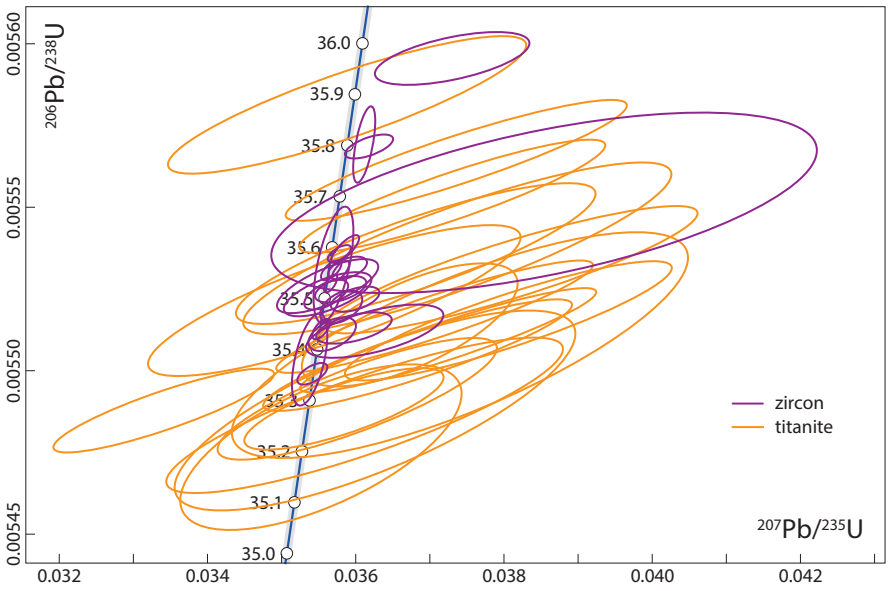

Fig. A6. Concordia diagram for KNT zircon and titanite dated by ID–TIMS (full data presented in Table A1).

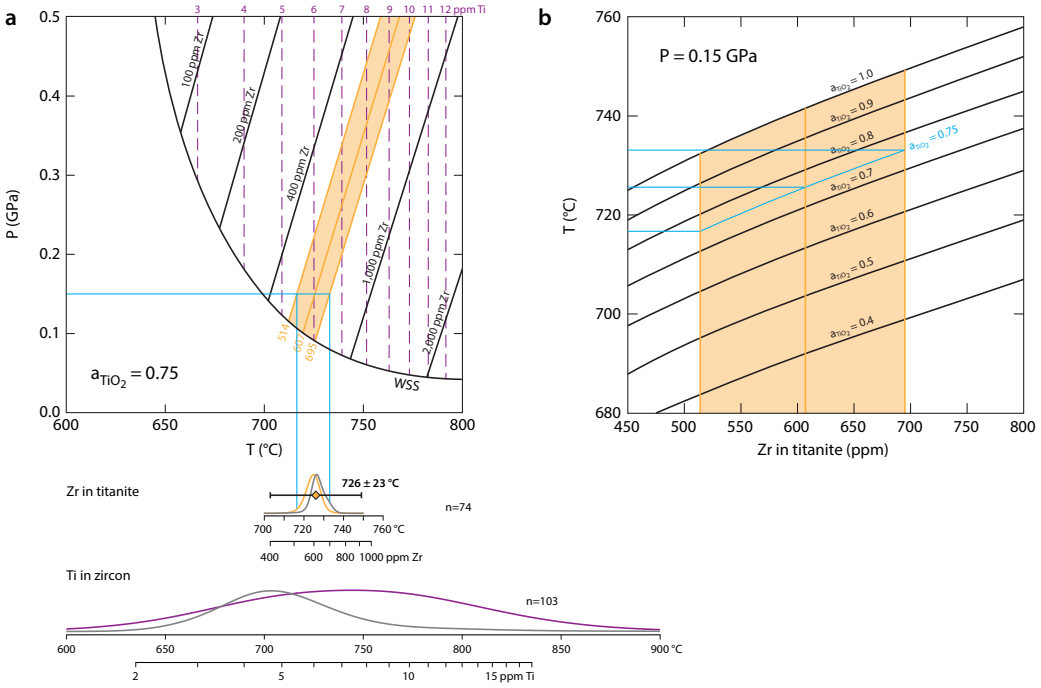

Fig. A7. Diagrams illustrating the sensitivity of the Zr-in-titanite thermometer to changes in pressure (**a**) and a_{TiO_2} (**b**). Yellow fields are delimited by Zr contents measured in KNT titanite, blue lines indicate temperatures returned by the thermometer for preferred values of P = 0.15 GPa (**a**) and a_{TiO_2} = 0.75 (**b**). WSS—water-saturated solidus.

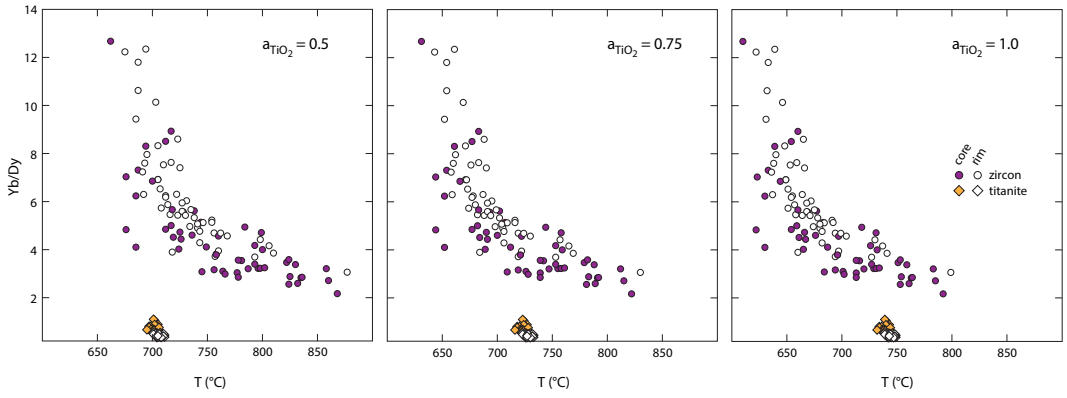

Fig. A8. Diagrams illustrating the sensitivity of Ti-in-zircon and Zr-in-titanite thermometry results to changing a_{TiO_2}. Using endmember a_{TiO_2} values for titanite-bearing systems results in either collapsing (with decreasing a_{TiO_2}) or expanding (increasing a_{TiO_2}) the interpreted window of storage temperature.

Table A1. ID-TIMS zircon and titanite U–Pb data.

Fraction	Composition				Isotopic ratios								Dates [Ma]					
	Th/U[a]	Pb* [pg][b]	Pbc [pg][c]	Pb*/Pbc[d]	$^{206}Pb/^{204}Pb$[e]	$^{206}Pb/^{238}U$[f]	±2σ [%]	$^{207}Pb/^{235}U$[f]	±2σ [%]	$^{207}Pb/^{206}Pb$[f]	±2σ [%]	Corr.	$^{206}Pb/^{238}U$[g]	±2σ	$^{206}Pb/^{238}U$[h]	±2σ	$^{207}Pb/^{235}U$[g]	±2σ
DS1402 zircon																		
b5	0.77	10.46	0.12	87.9	4893	0.0055174	0.056	0.03579	0.32	0.04707	0.29	0.678	35.469	0.020	35.554	0.020	35.71	0.11
b9	0.80	10.84	0.52	20.9	1167	0.0054979	0.094	0.03568	0.90	0.04709	0.86	0.498	35.345	0.033	35.430	0.033	35.60	0.31
b10B	0.92	4.93	0.11	46.6	2515	0.0055226	0.046	0.03578	0.44	0.04701	0.41	0.644	35.503	0.016	35.588	0.016	35.69	0.15
b10T	0.91	4.55	0.11	41.0	2216	0.005519	0.32	0.03570	0.75	0.04693	0.62	0.582	35.48	0.11	35.57	0.11	35.62	0.26
b14	0.74	16.24	0.25	66.3	3719	0.005556	0.21	0.03611	0.41	0.04716	0.33	0.617	35.717	0.075	35.802	0.075	36.02	0.15
b16	0.87	14.59	0.66	22.1	1213	0.0055182	0.063	0.03589	0.73	0.04719	0.70	0.480	35.475	0.022	35.559	0.022	35.80	0.26
b19C	0.75	7.69	0.36	21.5	1217	0.0055063	0.092	0.03580	0.79	0.04718	0.76	0.442	35.398	0.033	35.483	0.033	35.72	0.28
b19R	0.87	15.30	0.37	41.6	2270	0.0055240	0.077	0.03586	0.52	0.04710	0.46	0.786	35.512	0.027	35.597	0.027	35.77	0.18
b31	0.97	2.70	0.13	20.9	1126	0.0055553	0.066	0.03618	0.90	0.04726	0.86	0.620	35.713	0.024	35.798	0.023	36.09	0.32
s1	0.84	3.98	0.73	5.5	317	0.0055823	0.15	0.0373	2.8	0.04848	2.7	0.578	35.886	0.052	35.970	0.052	37.2	1.0
s2	0.87	10.71	0.59	18.0	993	0.0055086	0.070	0.03599	0.91	0.04741	0.88	0.513	35.414	0.025	35.498	0.025	35.90	0.32
s19	0.95	6.76	0.56	12.1	660	0.0054998	0.087	0.03598	1.4	0.04746	1.4	0.529	35.357	0.031	35.442	0.031	35.89	0.50
s24	0.85	3.69	0.36	10.1	570	0.0055126	0.15	0.03562	1.9	0.04689	1.8	0.720	35.439	0.053	35.524	0.053	35.54	0.67
s34	1.15	4.43	0.66	6.8	361	0.0054988	0.15	0.03626	2.6	0.04784	2.5	0.606	35.351	0.052	35.436	0.052	36.16	0.91
z2	0.93	4.48	0.10	44.1	2372	0.005490	0.26	0.03538	0.67	0.04676	0.58	0.533	35.295	0.090	35.380	0.090	35.30	0.23
z3	0.82	1.45	0.12	12.1	680	0.0055101	0.12	0.03562	1.7	0.04691	1.6	0.662	35.423	0.043	35.508	0.043	35.54	0.58
z10	1.08	4.42	0.10	45.6	2366	0.0054858	0.060	0.03541	0.57	0.04684	0.54	0.606	35.267	0.021	35.352	0.021	35.34	0.20

[a] Th contents calculated from radiogenic ^{208}Pb and ^{230}Th-corrected $^{206}Pb/^{238}U$ date of the sample, assuming concordance between U-Pb and Th-Pb systems.
[b] Total mass of radiogenic Pb.
[c] Total mass of common Pb.
[d] Ratio of radiogenic Pb (including ^{208}Pb) to common Pb.
[e] Measured ratio corrected for fractionation and spike contribution only.
[f] Measured ratios corrected for fractionation, tracer and blank.
[g] Isotopic dates calculated using $\lambda_{238} = 1.55125 \times 10^{-10}$ yr^{-1} and $\lambda_{235} = 9.8485 \times 10^{-10}$ yr^{-1} (Jaffey et al., 1971).
[h] Corrected for initial Th/U disequilibrium using radiogenic ^{208}Pb and $D_{Th/U}$ zircon–melt = 0.218, $D_{Th/U}$ titanite–melt = 1.96.

Table A1 continued. ID-TIMS zircon and titanite U–Pb data.

Fraction	Composition				Isotopic ratios								Dates [Ma]					
	Th/U [a]	Pb* [pg] [b]	Pbc [pg] [c]	Pb*/Pbc [d]	$^{206}Pb/^{204}Pb$ [e]	$^{206}Pb/^{238}U$ [f]	±2σ [%]	$^{207}Pb/^{235}U$ [f]	±2σ [%]	$^{207}Pb/^{206}Pb$ [f]	±2σ [%]	Corr.	$^{206}Pb/^{238}U$ [g]	±2σ	$^{206}Pb/^{238}U$ [h]	±2σ	$^{207}Pb/^{235}U$ [g]	±2σ
z11	1.00	5.86	0.07	82.6	4347	0.0054995	0.057	0.03553	0.34	0.04688	0.31	0.647	35.355	0.020	35.440	0.020	35.45	0.12
z12	0.85	2.39	0.09	26.4	1457	0.0055100	0.083	0.03560	0.83	0.04688	0.79	0.594	35.422	0.029	35.507	0.029	35.52	0.29
z18	0.79	10.16	0.18	55.4	3080	0.0055175	0.055	0.03567	0.38	0.04691	0.35	0.643	35.470	0.019	35.555	0.019	35.59	0.13
z20	1.13	1.01	0.63	1.6	100	0.0055381	0.50	0.0385	9.5	0.05050	9.3	0.583	35.60	0.18	35.69	0.18	38.4	3.6
z28	0.89	6.51	0.38	17.3	951	0.0055117	0.073	0.03580	0.97	0.04712	0.93	0.505	35.433	0.026	35.518	0.026	35.71	0.34
z30	0.83	14.27	0.12	119.9	6571	0.0055134	0.049	0.03566	0.25	0.04693	0.22	0.651	35.444	0.017	35.529	0.017	35.579	0.087
DS1402 titanite																		
t1c	8.59	50.16	73.64	0.7	31	0.005581	0.33	0.0374	6.2	0.0486	5.9	0.909	35.87	0.12	35.77	0.12	37.2	2.3
t2	7.65	17.05	23.33	0.7	33	0.005570	0.31	0.0373	5.5	0.0486	5.3	0.901	35.80	0.11	35.70	0.11	37.2	2.0
t6c	7.97	32.30	52.03	0.6	30	0.005598	0.38	0.0359	6.7	0.0465	6.4	0.869	35.98	0.14	35.88	0.13	35.8	2.4
t7	8.95	12.16	16.15	0.8	32	0.005503	0.43	0.0361	7.4	0.0476	7.0	0.855	35.37	0.15	35.27	0.15	36.0	2.6
t8	8.72	22.52	29.56	0.8	32	0.005533	0.31	0.0371	5.8	0.0486	5.5	0.920	35.57	0.11	35.46	0.11	37.0	2.1
t12	6.98	28.66	37.06	0.8	35	0.005508	0.34	0.0360	5.2	0.0475	5.0	0.834	35.41	0.12	35.30	0.12	35.9	1.8
t18	8.77	15.74	19.96	0.8	33	0.005524	0.62	0.0374	8.2	0.0491	7.8	0.775	35.51	0.22	35.41	0.22	37.3	3.0
t19	7.04	15.04	22.17	0.7	33	0.005504	0.55	0.0363	7.5	0.0478	7.0	0.772	35.38	0.20	35.28	0.20	36.2	2.6
t21	8.04	12.26	16.17	0.8	33	0.005552	0.39	0.0368	6.6	0.0481	6.3	0.850	35.69	0.14	35.59	0.14	36.7	2.4
t32	8.09	50.09	72.55	0.7	32	0.005521	0.31	0.0368	5.7	0.0484	5.4	0.904	35.49	0.11	35.39	0.11	36.7	2.0
t33	8.81	20.05	26.35	0.8	32	0.005532	0.33	0.0381	5.8	0.0499	5.5	0.888	35.56	0.12	35.46	0.12	37.9	2.2

[a] Th contents calculated from radiogenic ^{208}Pb and ^{230}Th-corrected $^{206}Pb/^{238}U$ date of the sample, assuming concordance between U-Pb and Th-Pb systems.
[b] Total mass of radiogenic Pb.
[c] Total mass of common Pb.
[d] Ratio of radiogenic Pb (including ^{208}Pb) to common Pb.
[e] Measured ratio corrected for fractionation and spike contribution only.
[f] Measured ratios corrected for fractionation, tracer and blank.
[g] Isotopic dates calculated using $\lambda_{238} = 1.55125 \times 10^{-10}$ yr^{-1} and $\lambda_{235} = 9.8485 \times 10^{-10}$ yr^{-1} (Jaffey et al., 1971).
[h] Corrected for initial Th/U disequilibrium using radiogenic ^{208}Pb and $D_{Th/U}$ zircon–melt = 0.218, $D_{Th/U}$ titanite–melt = 1.96.

Table A1 continued. ID-TIMS zircon and titanite U–Pb data.

Fraction	Composition				Isotopic ratios								Dates [Ma]					
	Th/U [a]	Pb* [pg] [b]	Pbc [pg] [c]	Pb*/Pbc [d]	$^{206}Pb/^{204}Pb$ [e]	$^{206}Pb/^{238}U$ [f]	±2σ [%]	$^{207}Pb/^{235}U$ [f]	±2σ [%]	$^{207}Pb/^{206}Pb$ [f]	±2σ [%]	Corr.	$^{206}Pb/^{238}U$ [g]	±2σ	$^{206}Pb/^{238}U$ [h]	±2σ	$^{207}Pb/^{235}U$ [g]	±2σ
t47	4.07	34.12	52.48	0.7	38	0.005504	0.24	0.0334	4.5	0.0440	4.3	0.877	35.384	0.083	35.280	0.082	33.4	1.5
t49	8.81	19.70	26.46	0.7	32	0.005547	0.35	0.0381	6.6	0.0498	6.3	0.887	35.66	0.12	35.56	0.12	38.0	2.5
t61	7.67	10.71	14.29	0.7	33	0.005538	0.42	0.0357	7.0	0.0468	6.7	0.840	35.60	0.15	35.50	0.15	35.6	2.5
t66	8.01	9.93	12.59	0.8	34	0.005554	0.47	0.0374	7.7	0.0488	7.3	0.864	35.70	0.17	35.60	0.17	37.3	2.8
t78	8.64	24.39	30.96	0.8	33	0.005526	0.29	0.0372	5.4	0.0489	5.1	0.924	35.52	0.10	35.42	0.10	37.1	2.0
t_1	8.84	50.51	71.67	0.7	31	0.005505	0.23	0.0358	3.8	0.0472	3.6	0.778	35.387	0.080	35.283	0.080	35.8	1.3
t_3	9.01	19.51	26.84	0.7	31	0.005493	0.46	0.0355	5.3	0.0469	5.1	0.647	35.31	0.16	35.21	0.16	35.5	1.9
t_5	7.97	23.44	30.42	0.8	33	0.005530	0.34	0.0367	4.0	0.0482	3.7	0.676	35.55	0.12	35.45	0.12	36.6	1.4

[a] Th contents calculated from radiogenic ^{208}Pb and ^{230}Th-corrected $^{206}Pb/^{238}U$ date of the sample, assuming concordance between U-Pb and Th-Pb systems.
[b] Total mass of radiogenic Pb.
[c] Total mass of common Pb.
[d] Ratio of radiogenic Pb (including ^{208}Pb) to common Pb.
[e] Measured ratio corrected for fractionation and spike contribution only.
[f] Measured ratios corrected for fractionation, tracer and blank.
[g] Isotopic dates calculated using $\lambda_{238} = 1.55125 \times 10^{-10}$ yr^{-1} and $\lambda_{235} = 9.8485 \times 10^{-10}$ yr^{-1} (Jaffey et al., 1971).
[h] Corrected for initial Th/U disequilibrium using radiogenic ^{208}Pb and $D_{Th/U}$ zircon–melt = 0.218, $D_{Th/U}$ titanite–melt = 1.96.

Table A2. Hf isotopic data for Kneeling Nun Tuff zircon (DS1402).

Sample	$^{176}Hf/^{177}Hf$	2 SE	Lu/Hf laser (rim)	$^{176}Lu/^{177}Hf$	$^{176}Hf/^{177}Hf$ (t)	εHf (t)	2σ
b5	0.282577	0.000044	0.0144	0.00201	0.282575	-6.63	1.63
b9	0.282617	0.000008	0.0082	0.00114	0.282616	-5.18	0.45
b14	0.282622	0.000005	0.0053	0.00073	0.282622	-4.98	0.53
b16	0.282632	0.000006	0.0115	0.00160	0.282631	-4.65	0.42
b17	0.282629	0.000010	0.0093	0.00130	0.282628	-4.77	0.51
b19a	0.282644	0.000015	0.0103	0.00143	0.282643	-4.23	0.73
b19b	0.282628	0.000007	0.0103	0.00143	0.282627	-4.80	0.55
b31	0.282673	0.000015	0.0112	0.00157	0.282672	-3.21	0.73
s1	0.282593	0.000023	0.0070	0.00097	0.282593	-6.00	0.88
s2	0.282625	0.000007	0.0115	0.00160	0.282624	-4.91	0.45
s7	0.282541	0.000056	0.0428	0.00596	0.282537	-7.99	2.00
s8	0.282627	0.000060	0.0083	0.00116	0.282626	-4.84	2.16
s9	0.282614	0.000006	0.0085	0.00119	0.282614	-5.27	0.42
s10	0.282601	0.000006	0.0093	0.00129	0.282600	-5.74	0.43
s19	0.282598	0.000009	0.0080	0.00111	0.282597	-5.86	0.48
s24	0.282667	0.000041	0.0090	0.00126	0.282666	-3.43	1.48
s29	0.282630	0.000006	0.0073	0.00102	0.282630	-4.71	0.43
s34	0.282589	0.000009	0.0077	0.00107	0.282588	-6.18	0.49
z3	0.282504	0.000026	0.0079	0.00110	0.282503	-9.19	1.04
z10	0.282515	0.000020	0.0058	0.00081	0.282514	-8.79	0.86
z22	0.282600	0.000043	0.0073	0.00102	0.282599	-5.78	1.59
z30	0.282554	0.000017	0.0070	0.00098	0.282554	-7.39	0.79

Table A3. Pb isotopic compositions of Kneeling Nun Tuff sanidine.

Sample	Grain	Core/rim	Average	$^{206}Pb/^{204}Pb$	2σ	$^{207}Pb/^{204}Pb$	2σ	$^{208}Pb/^{204}Pb$	2σ
DS1402 f1.1	1-7			18.006	0.022	15.541	0.028	38.255	0.092
DS1402 f1.2	1-7			17.999	0.026	15.542	0.031	38.281	0.098
DS1402 f1.3	1-12		*	17.940	0.030	15.510	0.033	38.172	0.103
DS1402 f1.4	1-12			17.992	0.032	15.574	0.035	38.387	0.105
DS1402 f1.5	1-12		*	17.955	0.030	15.501	0.033	38.116	0.102
DS1402 f1.6	1-12			17.970	0.022	15.528	0.029	38.203	0.093
DS1402 f1.7	1-3	rim		17.946	0.022	15.536	0.028	38.215	0.092
DS1402 f1.8	1-3	rim		17.903	0.024	15.465	0.030	37.952	0.094
DS1402 f1.9	1-3	core	*	17.950	0.037	15.485	0.038	38.093	0.111
DS1402 f1.10	1-3	core	*	17.944	0.023	15.489	0.029	38.070	0.093
DS1402 f2.1	2-50	rim	*	17.931	0.022	15.506	0.028	38.105	0.092
DS1402 f2.2	2-50	rim		17.972	0.022	15.556	0.028	38.264	0.093
DS1402 f2.3	2-50	core		18.036	0.022	15.553	0.029	38.283	0.093
DS1402 f2.4	2-16	rim		17.960	0.024	15.561	0.029	38.260	0.094
DS1402 f2.8	2-44	whole grain		18.029	0.022	15.608	0.028	38.464	0.093
preferred initial Pb composition				**17.944**	**0.017**	**15.498**	**0.019**	**38.111**	**0.069**

2σ uncertainty includes the uncertainty on the instrumental mass fractionation correction $\alpha_{Pb} = 0.094 \pm 0.06\%$/a.m.u. (2σ).

Appendix B

Maturation and rejuvenation of a silicic magma reservoir: high-resolution chronology of the Kneeling Nun Tuff

D. Szymanowski, B. S. Ellis, J. F. Wotzlaw, O. Bachmann

SUPPLEMENTARY MATERIAL

Analytical Methods

Sample preparation and initial characterisation

Samples of Kneeling Nun Tuff (KNT) ignimbrite and KNT-hosted magmatic inclusions were initially split into aliquots used to prepare polished thin sections, XRF powders and for rock crushing and separation of minerals. All samples were studied in thin section and all have at least one corresponding bulk-rock composition (Table B3). A summary of analyses performed on each sample and sampling locations are available as Table B1.

Zircon crystals were separated from the crushed and sieved material by standard heavy liquid (methylene iodide) and magnetic separation procedures, with the final concentrates hand-picked under a binocular microscope. Selected zircon crystals were then placed in quartz crucibles and annealed for 48 h at 900 °C in a muffle furnace. The annealed grains were mounted in epoxy, polished and imaged with backscattered electrons and cathodoluminescence (CL) using a JEOL JSM-6390 LA scanning electron microscope at ETH Zürich.

Bulk compositions

For bulk analyses, subsets of sample material were crushed and powdered, then ca. 1.5 g powder was heated to 950 °C for 2 h and reweighed to determine the loss on ignition (LOI). The desiccated powders were mixed with lithium tetraborate–metaborate flux and fused into glass beads. The bulk major and trace element compositions were determined at ETH Zürich by X-ray fluorescence (XRF) analysis using a 2.4 kW PANalytical Axios wavelength-dispersive X-ray spectrometer. For additional trace element concentrations, the same glass beads were subsequently analysed by LA–ICPMS using a 193-nm ArF excimer laser coupled to either a PerkinElmer ELAN 6100 or a PerkinElmer NexION 2000 quadrupole ICPMS.

Major elements in feldspar, amphibole and glass

Major element compositions of feldspar and amphibole were determined in a selection of samples from different stratigraphic levels of the KNT ignimbrite sheet as well as juvenile and lithic inclusions. Matrix glass was analysed in a single glassy sample of intracaldera KNT megabreccia (DS 1501) where melt had been quenched at contact with a metre-size lithic clast. The analyses were conducted on polished thin sections except for a large set of epoxy-mounted sanidine from sample DS 1402 previously characterised for Pb-isotope microsampling by Szymanowski et al. (2017 [*Chapter 2*]). All analyses were performed with a JEOL JXA 8200 electron probe microanalyser (EPMA) at ETH Zürich using five wavelength-dispersive spectrometers. For feldspar and amphibole we used an acceleration voltage of 15 kV and a beam current of 20 nA, for glass a reduced current of 10 nA. A fully focussed beam was used for amphibole, while increased beam diameters of 10 µm for feldspars and 20 µm for glass were chosen in order to avoid beam-induced

alkali migration. Analytical reproducibility was monitored by repeat analyses of in-house standards of the appropriate mineral phases throughout the analytical sessions.

Trace elements in feldspar and zircon

Trace element concentrations in the mineral phases were determined *in situ* using LA-ICPMS with a Thermo Element XR sector-field ICPMS coupled to an ASI Resolution 155 ArF excimer laser, with a spot diameter of 30 µm (zircon) or 43 µm (feldspar). A typical routine included 30 s of background measurement followed by 30 s of sample ablation, with a repetition rate of 5 Hz and an energy density of 2.5 J/cm². NIST SRM 610/612 glass was used as primary reference material and Si as internal standard. The concentration of Si in zircon was assumed to be stoichiometric (15.2% Si) while the values of Si in feldspar were based on average results from EPMA analyses within the respective sample. The data reduction was performed using SILLS (Guillong et al., 2008) for feldspar and Iolite (Paton et al., 2011) for zircon. To ensure the accuracy of analyses of Ti in zircon, the newly characterised high-Ti zircon GZ7 (Szymanowski et al., 2018 [*Chapter 4*]) was employed as primary reference material for this element. For zircon in sample DS 1402, trace element data were reproduced from Szymanowski et al. (2017 [*Chapter 2*]) with the sole exception of Ti, which was re-evaluated to match the isotope dilution value for zircon 91500 (Szymanowski et al., 2018 [*Chapter 4*]).

U–Pb zircon geochronology by ID-TIMS

Individual zircon crystals selected based on their optical and electron microscope appearance (additionally screened for inherited cores with U–Pb LA–ICPMS analyses) were extracted from the epoxy mounts, rinsed repeatedly with 4 N HNO_3 and loaded into 300 µl Savillex microcapsules for partial dissolution ('chemical abrasion') in ~70 µl 29 N HF + trace HNO_3 at 180 °C for 12 h (Mattinson, 2005). Crystals were then transferred into 3 ml Savillex beakers, fluxed in 6 N HCl on a hotplate and cleaned twice in 4 N HNO_3 in ultrasonic bath before loading back into their pre-cleaned microcapsules with a microdrop of 7 N HNO_3 and ~70 µl 29 N HF. The zircon samples were spiked with 5–12 mg of the EARTHTIME ^{202}Pb–^{205}Pb–^{233}U–^{235}U tracer solution (Condon et al., 2015; McLean et al., 2015) and dissolved in pressure vessels for ~60 h at 210 °C. After dissolution, samples were dried down and redissolved in 50 µl 6 N HCl at 180 °C for ~ 12 h to convert to chlorides, then dried down in preparation for ion exchange chemistry. Pb and U were separated using an HCl-based single-column anion exchange chemistry procedure modified from Krogh (1973). The resulting fractions were dried down with a drop of 0.02 M H_3PO_4, then loaded on single outgassed Re filaments with a silica gel emitter modified from Gerstenberger and Haase (1997). All measurements were performed with a Thermo TRITON Plus thermal ionisation mass spectrometer (TIMS) at ETH Zürich. Pb isotopes were measured in dynamic mode using a MasCom secondary electron multiplier. Instrumental Pb isotopic fractionation during zircon measurements was corrected online using the double spike (Condon et al., 2015). U was measured as oxides with $^{265}(UO_2)$, $^{267}(UO_2)$, $^{270}(UO_2)$ and $^{272}(UO_2)$ collected in Faraday cups connect-

ed to amplifiers with $10^{13}\,\Omega$ resistors (von Quadt et al., 2016). For samples with $^{270}(UO_2)$ intensities > 20 mV (relative to $10^{11}\,\Omega$ amplifier) the oxygen isotopic composition of UO_2 was measured using the method described by Wotzlaw et al. (2017) and interferences from minor UO_2 isotopologues were corrected online using the measured $^{18}O/^{16}O$. Measured $^{18}O/^{16}O$ ratios were indistinguishable from the average $^{18}O/^{16}O$ measured by Wotzlaw et al. (2017), so zircon analyses with lower U intensities were corrected using their preferred $^{18}O/^{16}O$ of 0.002064 ± 0.000011 (2σ). Instrumental U mass fractionation was corrected using the double spike (Condon et al., 2015) and a sample $^{238}U/^{235}U$ of 137.818 ± 0.045 (Hiess et al., 2012). Data reduction was performed using the Tripoli and U–Pb Redux software packages (Bowring et al., 2011) employing data reduction and uncertainty propagation algorithms of McLean et al. (2011). U–Pb ratios and dates were calculated relative to a tracer $^{235}U/^{205}Pb$ ratio of 100.23 ± 0.046 % (2σ) and using the decay constants of Jaffey et al. (1971). All common Pb in zircon analyses was attributed to laboratory blank and corrected with the average composition of total procedural blank measurements ($^{206}Pb/^{204}Pb = 18.41 \pm 0.39$, $^{207}Pb/^{204}Pb = 15.19 \pm 0.39$, $^{208}Pb/^{204}Pb = 36.93 \pm 0.91$ (2σ), $n = 14$). The accuracy of TIMS U and Pb isotope ratio measurements was monitored by routine analyses of NBS 982 Pb standard as well as U–Pb synthetic solutions and standard zircons throughout the period of the study (analyses compiled in Wotzlaw et al., 2017 and von Quadt et al., 2016).

All zircon $^{206}Pb/^{238}U$ dates were corrected for initial $^{230}Th–^{238}U$ disequilibrium resulting from the depletion in ^{230}Th, a long-lived intermediate daughter product in the $^{238}U–^{206}Pb$ decay chain, during zircon crystallisation (Schärer, 1984). Based on the long-lived nature of the KNT system and variable Th/U recorded by zircons, we previously (Szymanowski et al., 2017 [*Chapter 2*]) assumed that the variable Th/U of analysed zircons results from variations in the Th/U of melt in equilibrium with the individual crystals rather than from variable partitioning of Th and U between the mineral and the melt (i.e., the mineral/melt Th/U distribution coefficient $D_{Th/U}$ was constant). We used the same value of zircon $D_{Th/U} = 0.218$ as assumed in Szymanowski et al. (2017 [*Chapter 2*]), which translates into a correction of all $^{206}Pb/^{238}U$ dates by +84.9 ka. This value was not assigned an uncertainty as the assumed shift is fully systematic and does not affect the assessment of the relative timing of events within the magmatic system.

References

Bowring, J.F., McLean, N.M., Bowring, S.A., 2011. Engineering cyber infrastructure for U-Pb geochronology: Tripoli and U-Pb_Redux. Geochem. Geophys. Geosyst. 12, Q0AA19.

Condon, D.J., Schoene, B., McLean, N.M., Bowring, S.A., Parrish, R.R., 2015. Metrology and traceability of U–Pb isotope dilution geochronology (EARTHTIME Tracer Calibration Part I). Geochim. Cosmochim. Acta 164, 464–480.

Gerstenberger, H., Haase, G., 1997. A highly effective emitter substance for mass spectrometric Pb isotope ratio determinations. Chem. Geol. 136, 309–312.

Guillong, M., Meier, D.L., Allan, M.M., Heinrich, C.A., Yardley, B.W.D., 2008. SILLS: a MATLAB-based program for the reduction of laser ablation ICP-MS data of homogeneous materials and inclusions. Mineralogical Association of Canada Short Course 40, 328–333.

Hiess, J., Condon, D.J., McLean, N., Noble, S.R., 2012. $^{238}U/^{235}U$ systematics in terrestrial uranium-bearing minerals. Science 335, 1610–1614.

Jaffey, A.H., Flynn, K.F., Glendenin, L.E., Bentley, W.C., Essling, A.M., 1971. Precision measurement of half-lives and specific activities of ^{235}U and ^{238}U. Phys. Rev. C 4, 1889–1906.

Krogh, T.E., 1973. A low-contamination method for hydrothermal decomposition of zircon and extraction of U and Pb for isotopic age determinations. Geochim. Cosmochim. Acta 37, 485–494.

Mattinson, J.M., 2005. Zircon U–Pb chemical abrasion ("CA-TIMS") method: Combined annealing and multi-step partial dissolution analysis for improved precision and accuracy of zircon ages. Chem. Geol. 220, 47–66.

McLean, N.M., Bowring, J.F., Bowring, S.A., 2011. An algorithm for U–Pb isotope dilution data reduction and uncertainty propagation. Geochem. Geophys. Geosyst. 12, Q0AA18.

McLean, N.M., Condon, D.J., Schoene, B., Bowring, S.A., 2015. Evaluating uncertainties in the calibration of isotopic reference materials and multi-element isotopic tracers (EARTHTIME Tracer Calibration Part II). Geochim. Cosmochim. Acta 164, 481–501.

Paton, C., Hellstrom, J., Paul, B., Woodhead, J., Hergt, J., 2011. Iolite: Freeware for the visualisation and processing of mass spectrometric data. J. Anal. At. Spectrom. 26, 2508–2518.

Schärer, U., 1984. The effect of initial ^{230}Th disequilibrium on young U–Pb ages: the Makalu case, Himalaya. Earth Planet. Sci. Lett. 67, 191–204.

Szymanowski, D., Fehr, M.A., Guillong, M., Coble, M.A., Wotzlaw, J.F., Nasdala, L., Ellis, B.S., Bachmann, O., Schönbächler, M., 2018. Isotope-dilution anchoring of zircon reference materials for accurate Ti-in-zircon thermometry. Chem. Geol. 481, 146–154.

Szymanowski, D., Wotzlaw, J.F., Ellis, B.S., Bachmann, O., Guillong, M., von Quadt, A., 2017. Protracted near-solidus storage and pre-eruptive rejuvenation of large magma reservoirs. Nat. Geosci. 10, 777–782.

von Quadt, A., Wotzlaw, J.F., Buret, Y., Large, S.J.E., Peytcheva, I., Trinquier, A., 2016. High-precision zircon U/Pb geochronology by ID-TIMS using new 10^{13} ohm resistors. J. Anal. At. Spectrom. 31, 658–665.

Wotzlaw, J.F., Buret, Y., Large, S.J.E., Szymanowski, D., von Quadt, A., 2017. ID-TIMS U-Pb geochronology at the 0.1‰ level using 10^{13} Ω resistors and simultaneous U and $^{18}O/^{16}O$ isotope ratio determination for accurate UO_2 interference correction. J. Anal. At. Spectrom. 32, 579–586.

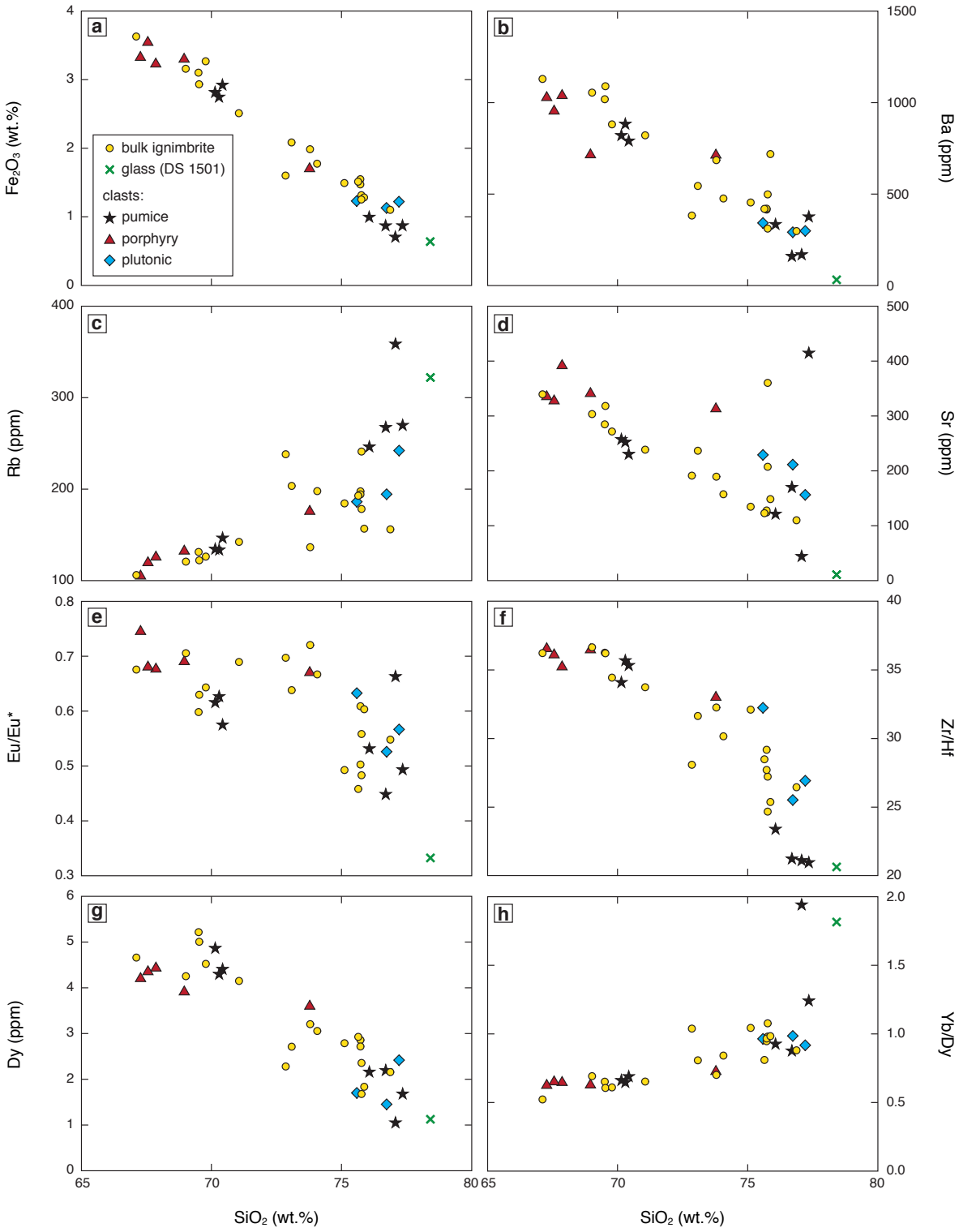

Fig. B1. Bulk compositions of Kneeling Nun Tuff ignimbrite, juvenile and lithic clasts and KNT matrix glass (sample 1501) from XRF and LA–ICPMS analyses. Ba, Sr, Eu/Eu* are controlled by feldspars, Fe by Fe–Ti oxides and ferromagnesian phases, Zr/Hf by zircon, and Dy and Yb/Dy are mostly sensitive to titanite crystallisation (see main text of Chapter 3).

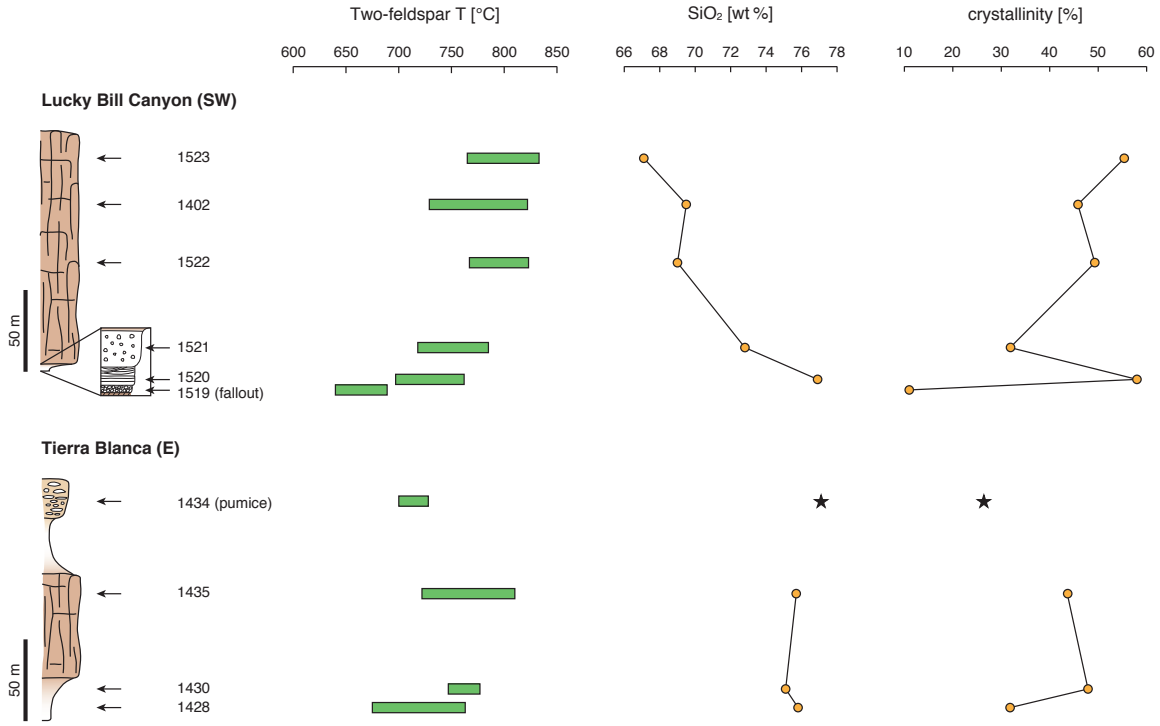

Fig. B2. Variation of selected parameters through two vertical sections of the Kneeling Nun Tuff outflow sheet. Sample numbers are indicated next to their positions (arrows). At Lucky Bill Canyon, the earliest erupted material has been deposited as a sequence of airfall, planar and cross-stratified 'surge' deposits and an unwelded massive ignimbrite. The earliest-erupted material is characterised by lower crystallinity and lower two-feldspar temperatures (Putirka, 2008) at both Lucky Bill Canyon and Tierra Blanca, as well as lower SiO_2 contents at Lucky Bill Canyon, indicating variable involvement of extracted melts.

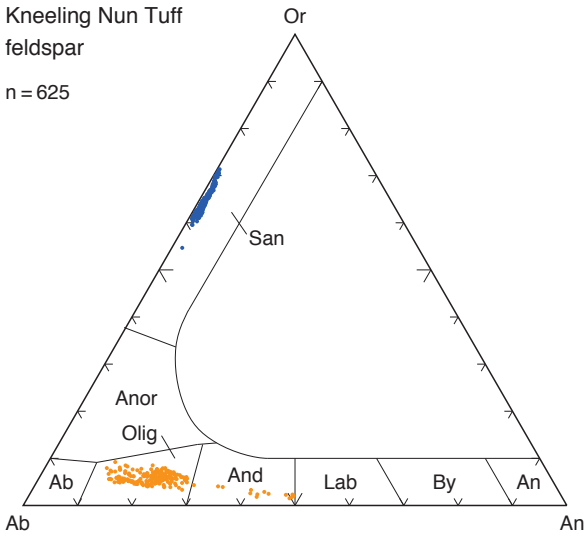

Fig. B3. Major element compositions of KNT feldspars.

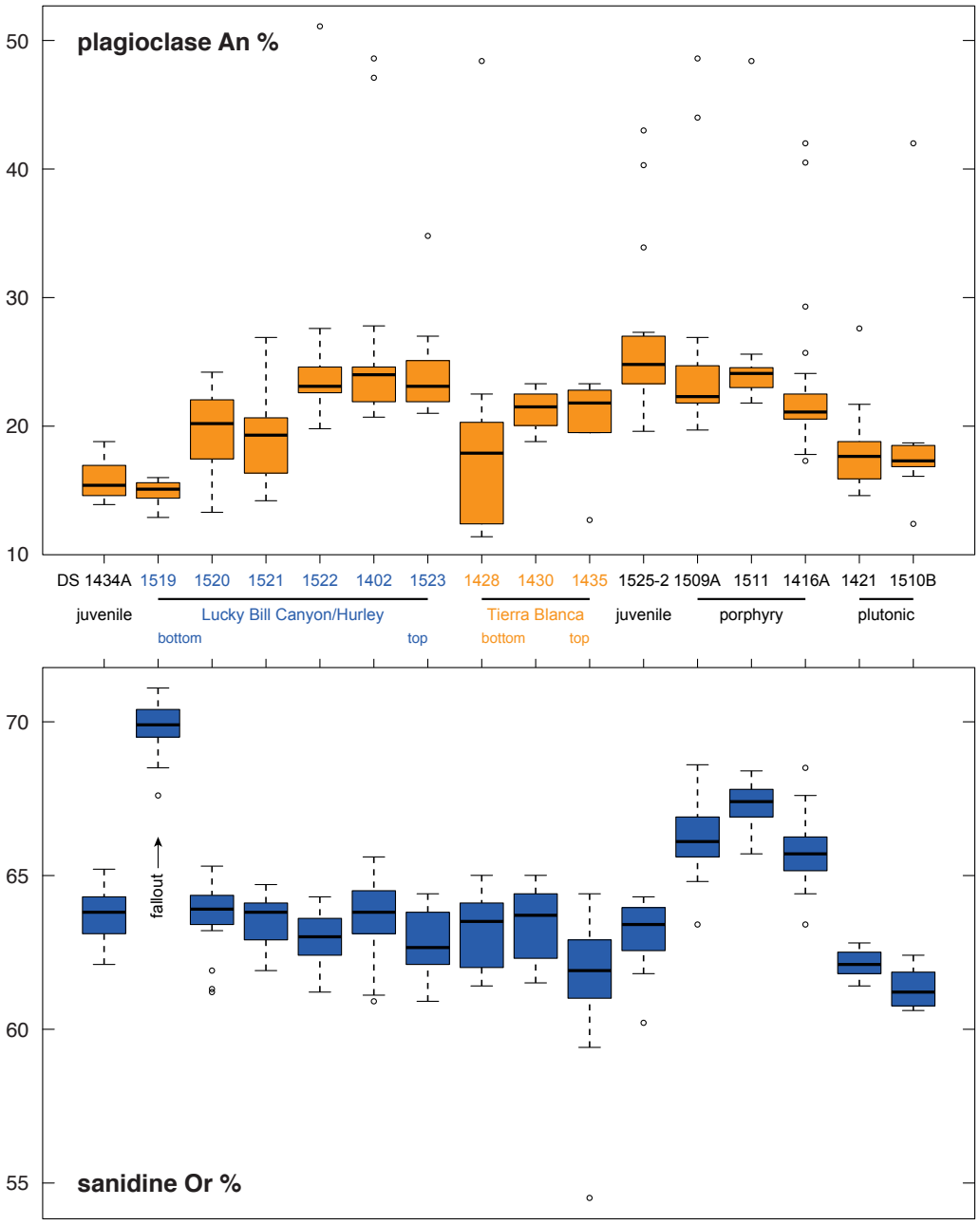

Fig. B4. Box plots of sanidine and plagioclase major element compositions. Boxes are drawn between first and third quartile values, with median marked with bold line. Whiskers extend to extreme values if those are no more than 1.5 times the interquartile range from the box, otherwise they are marked as outliers.

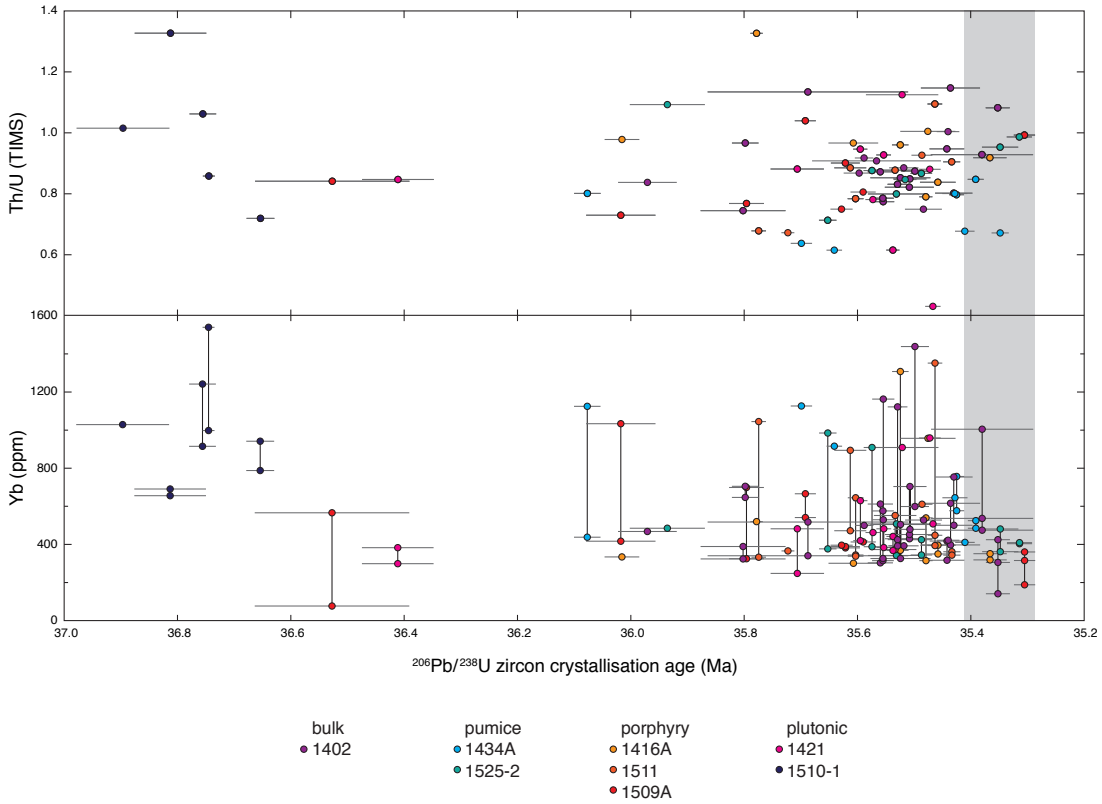

Fig. B5. Additional zircon trace element vs. time diagrams not included in Fig. 3.6.

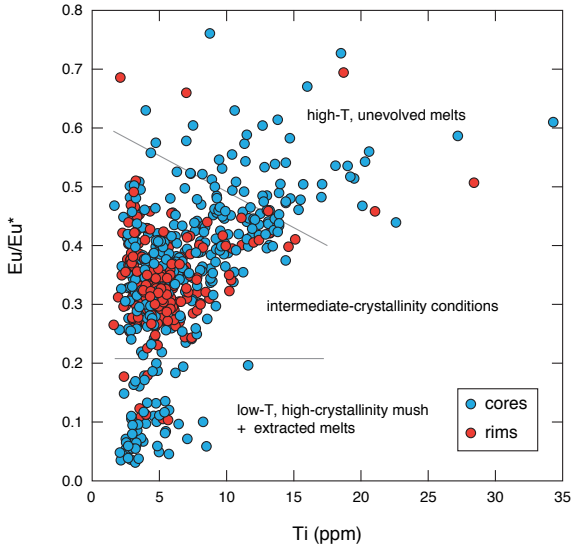

Fig. B6. Zircon trace elements illustrating the distinction between crystallisation from melts characteristic for most of reservoir volume (many cores and almost all rims), high-temperature unevolved melts that may be more proximal to recharge, and low-T, highly fractionated melts that represent either high-crystallinity conditions or extracted melt pockets (both occurring almost exclusively in innermost crystal cores).

Table B1. Summary of samples used and analyses performed in Chapter 3.

Sample	Latitude	Longitude	Location	Description	Whole-rock	Feldspars	High-Ba rims	Amphibole	Zircon
coarse-grained porphyrytic inclusions									
DS 1509	32.8583	107.8788	Emory Pass road NM152, intracaldera	many red porphyry inclusions	A, B, D	A	×	×	A
DS 1511	32.8826	107.8636	Emory Pass road NM152, megabreccia	single red porphyry inclusion	×	×	×	×	×
DS 1416	32.82995	107.79242	upper Cold Springs Canyon	KNT, big sample of intracaldera white porphyritic inclusion	A	A	—	—	A
plutonic inclusions									
DS 1510	32.8826	107.8636	Emory Pass road NM152, megabreccia	many granitic inclusions of variable texture, equi-granular to porphyrytic	1, 2	B	—		1510-1
DS 1421	32.88142	107.86349	Emory Pass road NM152, megabreccia	grey granitic lithic	×	×	—		×
pumices									
DS 1434	32.83204	107.5941	Tierra Blanca Canyon	KNT, white quartz-bearing pumices from uppermost cliff	A, B, C	A	—	—	A
DS 1413	32.82835	107.79592	upper Cold Springs Canyon	KNT, individual pumices from pumice-rich intracal-dera facies	A				
DS 1525	32.7762	108.0666	Chino mine	many pumices from mid-section KNT, fresh wall inside Chino mine	A, B, C	1525-2	×	×	1525-2
Lucky Bill Canyon									
DS 1519	32.7693	108.1047	Lucky Bill Canyon	fallout KNT	×	×	—	—	
DS 1520	32.7693	108.1047	Lucky Bill Canyon	planar stratified surge, not welded	×	×	—	—	
DS 1521	32.7693	108.1047	Lucky Bill Canyon	massive ignimbrite, not welded	×	×	—	(×)	
DS 1522	32.7701	108.1038	Lucky Bill Canyon	KNT mid-section	×	×	×	×	
DS 1523	32.7705	108.1035	Lucky Bill Canyon	KNT top of section	×	×	×	(×)	

×, present–analysed; (×), trace–not analysed; —, absent. If multiple sub-samples analysed, their IDs are indicated instead of '×'

Table B1 continued. Summary of samples used and analyses performed in Chapter 3.

Sample	Latitude	Longitude	Location	Description	Whole-rock	Feldspars	High-Ba rims	Amphibole	Zircon
Hurley									
DS 1402	32.72775	108.11784	Hurley	KNT, lowermost part of the cliff	C, F	×	×	×	×
DS 1524	32.7269	108.1181	Hurley	KNT, bottom of the cliff	×				
City of Rocks									
DS 1518	32.5901	107.9757	City of Rocks S.P.	KNT outflow, white	×				
Tierra Blanca									
DS 1428	32.82705	107.59758	Tierra Blanca Canyon S	bottom of S section: pink, non-welded, pumice-rich	×	×	—	—	
DS 1429	32.82732	107.59687	Tierra Blanca Canyon S	going up, white lithic-rich part forming first cliff	×				
DS 1430	32.82732	107.59687	Tierra Blanca Canyon S	top cliff in this part of section (S), big xtls to 0.5 cm	×	×	×	—	
DS 1435	32.83206	107.59572	Tierra Blanca Canyon at road	KNT, about 1/3 of 2nd cliff, quite pumice-poor	×	×	×	(×)	
DS 1505	32.81541	107.59611	Tierra Blanca far S, past windmill	KNT, base 20 cm above contact to conglomerate	×				
DS 1513	32.81496	107.59487	Tierra Blanca far S, past windmill	KNT, top of cliff	×				
DS 1514	32.83204	107.5941	Tierra Blanca Canyon at road	matrix of DS 1434	×				
intracaldera									
DS 1508	32.8518	107.8843	Emory Pass road NM152, intracaldera	KNT, intracaldera with pumice, red, xtl-rich	×				
DS 1501	32.8878	107.8566	Emory Pass road NM152, megabreccia	Glassy KNT sampled from contact to a m-sized (Rubio Peak) mafic clast within the megabreccia	×				
DS 1422	32.89273	107.83609	Gallinas Canyon	huge walls of grey intracaldera rocks mapped as KNT with one dominant, black type of lithic	×				

×, present–analysed; (×), trace–not analysed; —, absent. If multiple sub-samples analysed, their IDs are indicated instead of '×'

Table B2. ID-TIMS zircon U–Pb data.

Fraction	Composition				Isotopic ratios								Dates [Ma]					
	Th/U [a]	Pb* [pg] [b]	Pbc [pg] [c]	Pb*/Pbc [d]	$^{206}Pb/^{204}Pb$ [e]	$^{206}Pb/^{238}U$ [f]	±2σ [%]	$^{207}Pb/^{235}U$ [f]	±2σ [%]	$^{207}Pb/^{206}Pb$ [f]	±2σ [%]	Corr.	$^{206}Pb/^{238}U$ [g]	±2σ	$^{206}Pb/^{238}U$ [h]	±2σ	$^{207}Pb/^{235}U$ [g]	±2σ
DS1434A																		
b3	0.67	9.02	0.08	108	6151	0.0054852	0.043	0.035392	0.27	0.04682	0.23	0.776	35.263	0.015	35.348	0.015	35.315	0.092
s1	0.64	2.88	0.06	46	2647	0.0055399	0.053	0.03572	0.55	0.04678	0.51	0.693	35.614	0.019	35.699	0.019	35.63	0.19
3	0.68	4.31	0.08	57	3261	0.0054949	0.049	0.03544	0.42	0.04680	0.39	0.606	35.325	0.017	35.410	0.017	35.36	0.15
s17	0.80	8.54	0.09	94	5206	0.0054972	0.038	0.035516	0.24	0.04688	0.22	0.514	35.340	0.013	35.425	0.013	35.437	0.084
s18	0.85	12.68	0.06	214	11698	0.0054919	0.040	0.035494	0.21	0.046894	0.17	0.929	35.306	0.014	35.391	0.014	35.415	0.072
s24	0.62	8.73	0.14	62	3598	0.0055308	0.039	0.03594	0.33	0.04715	0.31	0.494	35.556	0.014	35.641	0.014	35.85	0.12
s26	0.80	4.96	0.14	36	2008	0.0055988	0.065	0.03638	0.59	0.04715	0.54	0.658	35.992	0.023	36.077	0.023	36.28	0.21
s28	0.80	15.85	0.18	86	4758	0.0054977	0.063	0.035435	0.27	0.04677	0.24	0.521	35.343	0.022	35.428	0.022	35.358	0.092
DS1525-2																		
z5	1.09	0.74	0.12	6	333	0.0055768	0.19	0.0352	3.4	0.0458	3.2	0.692	35.850	0.066	35.935	0.066	35.1	1.2
z11	0.95	3.73	0.09	41	1924	0.0054852	0.091	0.03576	1.5	0.04731	1.4	0.838	35.263	0.032	35.348	0.032	35.68	0.52
z13	0.71	7.38	0.10	72	4065	0.0055326	0.044	0.03580	0.33	0.04696	0.30	0.752	35.567	0.015	35.652	0.015	35.72	0.12
z16	0.85	6.77	0.17	40	2221	0.0055113	0.057	0.03570	0.51	0.04699	0.46	0.793	35.431	0.020	35.516	0.020	35.61	0.18
z24	0.87	4.20	0.08	52	2830	0.0055069	0.054	0.03550	0.43	0.04677	0.39	0.796	35.402	0.019	35.487	0.019	35.42	0.15
z27	0.99	4.51	0.07	64	2948	0.0054799	0.063	0.03561	0.98	0.04716	0.93	0.824	35.229	0.022	35.314	0.022	35.53	0.34
z30	0.88	6.90	0.16	43	2338	0.0055205	0.042	0.03565	0.43	0.04685	0.41	0.586	35.489	0.015	35.574	0.015	35.56	0.15
z32	0.80	1.41	0.06	24	1178	0.0055137	0.14	0.03500	2.6	0.0461	2.5	0.915	35.446	0.050	35.531	0.050	34.93	0.89

[a] Th contents calculated from radiogenic ^{208}Pb and ^{230}Th-corrected $^{206}Pb/^{238}U$ date of the sample, assuming concordance between U-Pb and Th-Pb systems.
[b] Total mass of radiogenic Pb.
[c] Total mass of common Pb.
[d] Ratio of radiogenic Pb (including ^{208}Pb) to common Pb.
[e] Measured ratio corrected for fractionation and spike contribution only.
[f] Measured ratios corrected for fractionation, tracer and blank.
[g] Isotopic dates calculated using $\lambda_{238} = 1.55125 \times 10^{-10}$ yr^{-1} and $\lambda_{235} = 9.8485 \times 10^{-10}$ yr^{-1} (Jaffey et al., 1971).
[h] Corrected for initial Th/U disequilibrium using radiogenic ^{208}Pb and $D_{Th/U}$ zircon–melt = 0.218.

Table B2 continued. ID-TIMS zircon U–Pb data.

Fraction	Composition				Isotopic ratios								Dates [Ma]					
	Th/U [a]	Pb* [pg] [b]	Pbc [pg] [c]	Pb*/Pbc [d]	$^{206}Pb/^{204}Pb$ [e]	$^{206}Pb/^{238}U$ [f]	±2σ [%]	$^{207}Pb/^{235}U$ [f]	±2σ [%]	$^{207}Pb/^{206}Pb$ [f]	±2σ [%]	Corr.	$^{206}Pb/^{238}U$ [g]	±2σ	$^{206}Pb/^{238}U$ [h]	±2σ	$^{207}Pb/^{235}U$ [g]	±2σ
DS1416A																		
z2-1	1.01	21.10	0.58	37	1941	0.0055051	0.14	0.03540	0.69	0.04666	0.59	0.759	35.391	0.049	35.475	0.049	35.33	0.24
z2-2	0.97	3.46	0.49	7	393	0.0055256	0.12	0.03639	2.3	0.0478	2.2	0.559	35.522	0.044	35.607	0.044	36.29	0.81
z5	0.79	13.50	0.09	144	7993	0.0055056	0.033	0.035562	0.19	0.046867	0.17	0.582	35.394	0.012	35.479	0.012	35.482	0.065
z9	1.33	12.96	0.14	93	4570	0.0055522	0.031	0.035943	0.25	0.04697	0.23	0.547	35.693	0.011	35.778	0.011	35.855	0.087
z14	0.92	6.85	0.08	82	3844	0.0054880	0.084	0.03555	0.80	0.04701	0.75	0.645	35.281	0.029	35.366	0.029	35.47	0.28
z18	0.98	3.91	0.11	36	1928	0.0055893	0.086	0.03640	0.81	0.04726	0.75	0.720	35.931	0.031	36.015	0.031	36.31	0.29
z20	0.84	35.66	0.18	202	11033	0.0055023	0.089	0.035564	0.15	0.046899	0.11	0.654	35.373	0.031	35.458	0.031	35.484	0.053
z21	0.89	9.54	0.15	66	3562	0.0056289	0.047	0.03708	0.33	0.04780	0.29	0.839	36.184	0.017	36.269	0.017	36.97	0.12
z23	0.96	10.83	0.12	93	4948	0.0055127	0.041	0.03568	0.29	0.04696	0.26	0.831	35.439	0.015	35.524	0.015	35.60	0.10
DS1511																		
z18	0.78	26.98	0.17	161	8900	0.0055250	0.039	0.035666	0.18	0.046839	0.16	0.648	35.518	0.014	35.603	0.014	35.583	0.064
z19	0.91	7.04	0.08	91	4908	0.0054985	0.043	0.03546	0.30	0.04679	0.28	0.619	35.349	0.015	35.433	0.015	35.38	0.11
z24	0.68	27.10	0.12	220	12507	0.0055517	0.036	0.03603	0.13	0.047085	0.11	0.601	35.689	0.013	35.774	0.013	35.936	0.046
z25	0.88	4.76	0.19	25	1364	0.0055141	0.11	0.03576	0.92	0.04705	0.83	0.918	35.449	0.038	35.533	0.037	35.67	0.32
z28	1.09	13.97	0.11	128	6592	0.0055031	0.036	0.035621	0.22	0.046967	0.19	0.724	35.378	0.013	35.463	0.013	35.540	0.077
z30-1	0.67	5.61	0.09	59	3381	0.0055436	0.032	0.03580	0.34	0.04686	0.32	0.629	35.638	0.011	35.723	0.011	35.72	0.12
z31	0.93	3.45	0.08	41	2226	0.0055067	0.053	0.03569	0.52	0.04703	0.49	0.593	35.401	0.019	35.486	0.019	35.61	0.18
z39	0.89	2.72	0.09	30	1646	0.0055264	0.080	0.03558	0.70	0.04672	0.66	0.533	35.528	0.028	35.612	0.028	35.50	0.24

[a] Th contents calculated from radiogenic ^{208}Pb and ^{230}Th-corrected $^{206}Pb/^{238}U$ date of the sample, assuming concordance between U-Pb and Th-Pb systems.
[b] Total mass of radiogenic Pb.
[c] Total mass of common Pb.
[d] Ratio of radiogenic Pb (including ^{208}Pb) to common Pb.
[e] Measured ratio corrected for fractionation and spike contribution only.
[f] Measured ratios corrected for fractionation, tracer and blank.
[g] Isotopic dates calculated using $\lambda_{238} = 1.55125 \times 10^{-10}$ yr^{-1} and $\lambda_{235} = 9.8485 \times 10^{-10}$ yr^{-1} (Jaffey et al., 1971).
[h] Corrected for initial Th/U disequilibrium using radiogenic ^{208}Pb and $D_{Th/U}$ zircon–melt = 0.218.

Table B2 continued. ID-TIMS zircon U–Pb data.

Fraction	Composition				Isotopic ratios								Dates [Ma]					
	Th/U [a]	Pb* [pg] [b]	Pbc [pg] [c]	Pb*/Pbc [d]	$^{206}Pb/^{204}Pb$ [e]	$^{206}Pb/^{238}U$ [f]	±2σ [%]	$^{207}Pb/^{235}U$ [f]	±2σ [%]	$^{207}Pb/^{206}Pb$ [f]	±2σ [%]	Corr.	$^{206}Pb/^{238}U$ [g]	±2σ	$^{206}Pb/^{238}U$ [h]	±2σ	$^{207}Pb/^{235}U$ [g]	±2σ
DS1509A																		
z9	0.84	1.18	0.14	8	402	0.005669	0.38	0.0381	7.1	0.0488	6.7	0.957	36.44	0.14	36.53	0.14	38.0	2.6
z19	0.90	3.35	0.09	39	2125	0.0055278	0.072	0.03566	0.65	0.04681	0.62	0.395	35.536	0.026	35.621	0.026	35.58	0.23
z20	0.75	4.85	0.08	59	3284	0.0055288	0.055	0.03553	0.41	0.04663	0.38	0.580	35.543	0.020	35.628	0.020	35.45	0.14
z23	0.81	2.52	0.08	32	1758	0.0055229	0.063	0.03556	0.68	0.04672	0.64	0.706	35.505	0.022	35.590	0.022	35.48	0.24
z27	1.04	4.43	0.12	36	1892	0.0055388	0.053	0.03593	0.56	0.04706	0.53	0.534	35.607	0.019	35.692	0.019	35.84	0.20
z31	0.77	25.45	0.27	95	5272	0.0055550	0.086	0.035994	0.22	0.047015	0.19	0.509	35.711	0.031	35.796	0.031	35.905	0.077
z35	0.73	6.35	0.31	20	1150	0.0055896	0.17	0.03584	1.5	0.04653	1.3	0.822	35.933	0.061	36.017	0.061	35.76	0.51
z44	0.99	11.55	0.19	61	3236	0.0054785	0.053	0.03540	0.39	0.04688	0.34	0.917	35.220	0.019	35.305	0.019	35.32	0.13
DS1421																		
z5	0.62	21.14	0.12	176	10192	0.0055147	0.033	0.035777	0.17	0.047073	0.14	0.857	35.452	0.012	35.537	0.012	35.692	0.059
z6	0.43	6.70	0.11	60	3675	0.0055037	0.039	0.03557	0.33	0.04690	0.30	0.645	35.382	0.014	35.467	0.014	35.49	0.11
z7	0.88	2.64	0.08	35	1647	0.0055410	0.13	0.03584	1.9	0.04693	1.8	0.829	35.621	0.047	35.706	0.047	35.75	0.68
z12	0.85	1.93	0.10	19	897	0.0056510	0.18	0.0373	3.2	0.0479	3.0	0.912	36.326	0.063	36.411	0.063	37.2	1.2
z13	0.95	7.70	0.12	66	3538	0.0055237	0.035	0.03584	0.30	0.04709	0.28	0.496	35.510	0.012	35.595	0.012	35.76	0.11
z15	0.78	10.00	0.10	104	5777	0.0055202	0.038	0.035667	0.24	0.04688	0.22	0.517	35.488	0.013	35.572	0.013	35.585	0.084
z20	0.88	5.30	0.12	45	2446	0.0055046	0.055	0.03561	0.47	0.04693	0.44	0.701	35.387	0.019	35.472	0.019	35.53	0.17
z21	0.93	6.29	0.13	47	2515	0.0055172	0.037	0.03563	0.41	0.04686	0.39	0.571	35.469	0.013	35.553	0.013	35.55	0.14
z28	1.13	0.69	0.12	6	312	0.005512	0.18	0.0354	3.4	0.0466	3.2	0.669	35.436	0.064	35.521	0.064	35.3	1.2

[a] Th contents calculated from radiogenic ^{208}Pb and ^{230}Th-corrected $^{206}Pb/^{238}U$ date of the sample, assuming concordance between U-Pb and Th-Pb systems.
[b] Total mass of radiogenic Pb.
[c] Total mass of common Pb.
[d] Ratio of radiogenic Pb (including ^{208}Pb) to common Pb.
[e] Measured ratio corrected for fractionation and spike contribution only.
[f] Measured ratios corrected for fractionation, tracer and blank.
[g] Isotopic dates calculated using $\lambda_{238} = 1.55125 \times 10^{-10}$ yr^{-1} and $\lambda_{235} = 9.8485 \times 10^{-10}$ yr^{-1} (Jaffey et al., 1971).
[h] Corrected for initial Th/U disequilibrium using radiogenic ^{208}Pb and $D_{Th/U}$ zircon–melt = 0.218.

Table B2 continued. ID-TIMS zircon U–Pb data.

Fraction	Composition				Isotopic ratios								Dates [Ma]					
	Th/U [a]	Pb* [pg] [b]	Pbc [pg] [c]	Pb*/Pbc [d]	$^{206}Pb/^{204}Pb$ [e]	$^{206}Pb/^{238}U$ [f]	±2σ [%]	$^{207}Pb/^{235}U$ [f]	±2σ [%]	$^{207}Pb/^{206}Pb$ [f]	±2σ [%]	Corr.	$^{206}Pb/^{238}U$ [g]	±2σ	$^{206}Pb/^{238}U$ [h]	±2σ	$^{207}Pb/^{235}U$ [g]	±2σ
DS1510-1																		
z6	0.72	5.45	0.10	56	3195	0.0056888	0.068	0.03685	0.49	0.04700	0.44	0.718	36.569	0.025	36.653	0.025	36.75	0.18
z13	1.33	0.90	0.06	14	681	0.0057136	0.17	0.0370	3.3	0.0470	3.1	0.725	36.727	0.063	36.812	0.063	36.9	1.2
z14	0.86	15.87	0.10	158	8598	0.0057030	0.029	0.036949	0.16	0.047010	0.14	0.619	36.660	0.011	36.745	0.011	36.841	0.059
z21	1.06	4.15	0.14	29	1542	0.0057047	0.065	0.03674	0.75	0.04673	0.71	0.652	36.670	0.024	36.755	0.024	36.64	0.27
z22	1.02	1.85	0.24	8	413	0.005727	0.22	0.0373	5.0	0.0473	4.9	0.717	36.811	0.082	36.896	0.082	37.2	1.8

[a] Th contents calculated from radiogenic ^{208}Pb and ^{230}Th-corrected $^{206}Pb/^{238}U$ date of the sample, assuming concordance between U-Pb and Th-Pb systems.
[b] Total mass of radiogenic Pb.
[c] Total mass of common Pb.
[d] Ratio of radiogenic Pb (including ^{208}Pb) to common Pb.
[e] Measured ratio corrected for fractionation and spike contribution only.
[f] Measured ratios corrected for fractionation, tracer and blank.
[g] Isotopic dates calculated using $\lambda_{238} = 1.55125 \times 10^{-10}\ yr^{-1}$ and $\lambda_{235} = 9.8485 \times 10^{-10}\ yr^{-1}$ (Jaffey et al., 1971).
[h] Corrected for initial Th/U disequilibrium using radiogenic ^{208}Pb and $D_{Th/U}$ zircon–melt = 0.218.

Appendix C

Isotope-dilution anchoring of zircon reference materials for accurate Ti-in-zircon thermometry

D. Szymanowski, M. A. Fehr, M. Guillong, M. A. Coble, J. F. Wotzlaw, L. Nasdala, B. S. Ellis, O. Bachmann, M. Schönbächler

SUPPLEMENTARY MATERIAL

Rock reference samples

The Ti content of three magmatic geochemical reference samples (BHVO-2, BCR-2, AGV-2) was measured to check the accuracy of the applied isotope dilution procedure. Sample powders of 140–220 mg were digested in concentrated HF–HNO in Parr® bombs (Schönbächler et al., 2004; Williams, 2014). Titanium stable isotope analyses were performed using a Neptune multi-collector ICP-MS (MC-ICP-MS) at the Open University (UK) after chemical isolation of Ti from spiked sample aliquots by anion-exchange chromatography (Schönbächler et al., 2004; Williams, 2014; Williams et al., 2014). Full procedural blanks for MC-ICP-MS analyses were on average 3 ng Ti and ranged from 0.6 to 16 ng Ti, which is negligible given that sample aliquots of 50 µg Ti were processed. To minimise blank contribution for the determination of Ti contents in zircons (where smaller amounts of Ti are available for analyses) Ti isotope analyses were performed on spiked unprocessed zircon sample solutions on a Thermo Element XR ICP-MS as detailed in the main text.

Table C1. Titanium contents of geochemical reference samples determined by isotope dilution using the ^{47}Ti–^{49}Ti spike

Sample	Description	TiO_2 [wt%] [a]	
		this study	reference [a]
BHVO-2 (aliq. 1)	basalt, Hawaii	2.748	2.731 ± 0.018
BHVO-2 (aliq. 2)	basalt, Hawaii	2.736	2.731 ± 0.018
BCR-2 (aliq. 1)	basalt, Columbia River	2.270	2.265 ± 0.024
BCR-2 (aliq. 2)	basalt, Columbia River	2.246	2.265 ± 0.024
AGV-2	andesite, Oregon	1.037	1.051 ± 0.023

[a] reference values from Jochum et al. (2016)

References

Jochum, K.P., Weis, U., Schwager, B., Stoll, B., Wilson, S.A., Haug, G.H., Andreae, M.O., Enzweiler, J., 2016. Reference values following ISO guidelines for frequently requested rock reference materials. Geostand. Geoanal. Res. 40, 333–350.

Schönbächler, M., Rehkämper, M., Lee, D.C., Halliday, A.N., 2004. Ion exchange chromatography and high precision isotopic measurements of zirconium by MC–ICP–MS. Analyst 129, 32–37.

Williams, N.H., 2014. Titanium isotope cosmochemistry. PhD thesis, University of Manchester.

Williams, N.H., Schönbächler, M., Fehr, M.A., Akram, W.M., Parkinson, I.J., 2014. Different heterogeneously distributed titanium isotope components in solar system materials and mass-dependent titanium isotope variations. Lunar Planet. Sci. Conf. 45, 2183.